# DEPTH IMAGING OF CRUSTAL SCALE SEISMIC REFLECTION SURVEYS IN SOUTHERN CALIFORNIA

---

A Dissertation

Presented to

the Faculty of the Department of Geosciences

University of Houston

---

In Partial Fulfillment

of the Requirements for the Degree

Doctor of Philosophy

---

By

Michael Thornton

May 2006

# DEPTH IMAGING OF CRUSTAL SCALE SEISMIC REFLECTION SURVEYS IN SOUTHERN CALIFORNIA

---

Michael Thornton

APPROVED:

---

Dr. Hua-wei Zhou, Chairman

---

Dr. Samuel Gray

---

Dr. Stuart Hall

---

Dr. Fred Hilterman

---

Dean, College of Natural Sciences and Mathematics

# Acknowledgments

I would like to thank Dr. Hua-wei Zhou for his support and guidance over the course of this project. I would also like to thank the members of the committee: Dr Sam Gray, Dr. Stuart Hall, and Dr. Fred Hilterman for their help and suggestions. Thanks to Drs. Yu Zhang and James Sun for their advice and guidance on the migration code. Thanks to the Incorporated Research Institutions for Seismology and the Southern California Earthquake Center for providing the data used here. Thanks to my parents for their encouragement. A special thanks to Cory Hoelting for the beer fueled discussions about geophysics and life. Last, but not least, a very special thanks to my wife, Rebecca, for her patience and support.

# DEPTH IMAGING OF CRUSTAL SCALE SEISMIC REFLECTION SURVEYS IN SOUTHERN CALIFORNIA

An Abstract of a Dissertation

Presented to

the Faculty of the Department of Geosciences

University of Houston

---

In Partial Fulfillment

of the Requirements for the Degree

Doctor of Philosophy

---

By

Michael Thornton

May 2006

# Abstract

Advanced seismic reflection imaging techniques can be used to substantially improve the images obtained from deep crustal reflection surveys. This dissertation demonstrates this thesis via application of prestack wave equation migration to two crustal scale reflection surveys collected by the Los Angeles Regional Seismic Experiment (LARSE) in southern California.

Wave equation prestack depth imaging is an effective tool for imaging weak reflection energy in the presence of noise, primarily due to wavefield correlation used by this process. A secondary advantage is the ability to image each frequency component independently and form the image bandwidth after migration, allowing the optimal bandwidth to be more effectively determined.

Using tomographically generated crustal velocity models, the images of the LARSE lines produced here show substantial improvements over the previous imaging efforts. Coherent images of features as deep as the Moho are seen from both lines. Reflections from structures associated with major fault zones allow the subsurface locations of the San Andreas and San Gabriel fault zones to be inferred.

The depth images correlate well with teleseismic measurements of crustal thickness and gross crustal structure. The images also correlate well with the spatial distribution of local seismic activity. A strong correlation between reflectivity and local seismic activity

suggests that faults or fault prone areas form a substantial portion of the observed reflectivity.

The new depth images show several previously unknown crustal features: thickening and discontinuities of the Moho associated with the San Andreas Fault, discontinuities in the Moho associated with the San Gabriel and Northridge fault systems, and a mid-crustal shear zone beneath the San Gabriel Mountains.

# Contents

# List of Figures

# Introduction

Prestack depth migration is the tool of choice for modern exploration scale seismic reflection imaging. This technology often allows images to be constructed in areas where the conventional common midpoint (CMP) stack technique fails. Surprisingly, this technology has been largely ignored by the crustal imaging community. My thesis is that with appropriate adaptations, prestack depth imaging can be an effective and important tool for deep crustal seismic reflection imaging studies. I assert that one type of prestack depth migration, shot profile wave equation migration, has several key characteristics that make it particularly well suited for deep crustal imaging. In this dissertation, I will demonstrate that this technique can produce substantial improvements over previous imaging efforts.

Crustal scale seismic reflection surveying was pioneered by the Consortium for Continental Reflection Profiling (COCORP) in 1975, the first series of large scale seismic reflection surveys in the United States. The success of this program has inspired many other similar programs around the world including BIRPS (Britain), DEKORP (Germany), INDEPTH (Tibet) and LITHOPROBE (Canada). The objective of these programs is to better understand the structures and tectonics of the continental lithosphere. Often these surveys are carried out for purely scientific purposes, but the knowledge gleaned from these efforts can often be applied to more practical purposes.

One such program is the Los Angeles Regional Seismic Experiment (LARSE) consortium. This program was formed in 1993 to acquire crustal scale seismic data to better understand the continental crust in southern California. A major driver behind this program was the need to better understand the fault structure and regional tectonics of the area for earthquake hazard assessment. Although the data acquired by the LARSE consortium has provided insight on the crustal structure of southern California, the reflection images have largely failed to meet the objectives of delineating faults and major crustal structures.

A fundamental problem with nearly all deep crustal reflection surveys is low signal to noise ratios. Primary reflections from crustal structures are likely to be very weak, they must travel very long distances (100 km or more) from source to reflector to receiver. The areas of interest are likely to be geologically complex, which leads to scattering and complex reflection paths. Furthermore, the large scale of these surveys (often 100 km of more), access restrictions, and limited budgets dictate coarse shot and receiver spacing in the acquisition geometry. Often a receiver station is occupied by a single sensor, leaving the entire receiver spread vulnerable to contamination by surface waves. Furthermore, the coarse acquisition geometry aliases the surface waves, making it very difficult to remove this noise.

The typical approach used to deal with the signal to noise problem has been common midpoint stacking of trace envelopes. This technique was adopted in an attempt to

produce a zero-offset time section without accurate moveout velocities. By stacking trace envelopes rather than the traces themselves, the cancellation effect of the stacking process is removed, offering a degree of leeway in the alignment of the primary reflections. Although designed to cope with low signal and high noise levels, envelope stacking actually does very little to enhance signal and suppress noise. By removing the cancellation effect of stacking, any strong event will dominate the stack.

Deep crustal imaging has been largely limited to poststack migration. Early attempts at migration imaging were problematic; primarily due to discontinuous and segmented diffractions in the time stacks. Warner (1987) attributes this problem to unaccounted for overburden effects; Louie and Vidale (1991) point to complexity in the reflectors themselves. However, low signal to noise ratios, and the relatively low fold common in these surveys undoubtedly played a significant part in the poor stack images. Currently, the most common imaging practice for crustal surveys is line migration of reflector segments interpreted from time or envelope stacks.

Recently, crustal researchers have begun to use prestack Kirchhoff depth migration as an imaging tool. Henning *et al*. (2004) used Kirchhoff prestack depth migration to image crustal structures to a depth of 12 km from marine streamer data acquired off the west coast of Spain. Dessa *et al*. (2004) used the same technique to image 20 km of the upper crust from ocean bottom seismometer data acquired offshore of Japan. However, the

time domain CMP stack seems to remain the predominant imaging tool in the field (Kopp *et al*., 2002; Hopper *et al*. 2003, Ali and Watts, 2003).

Why this remains so is unclear; perhaps it is a lack of experience with the technology, or a perception that prestack depth migration is a tool for very specialized problems. I suspect that the main hurdle is the poor signal to noise ratios common in crustal surveys; there may be the assumption that these techniques can only work in good data areas. This is conjecture; but the only two examples I could find of prestack Kirchhoff depth migration applied to crustal surveys (sited above) were applied to relatively clean marine data sets. I claim that not only is this assumption wrong, but just the opposite is true. Data sets with poor signal levels require more sophisticated techniques to deal with the noise, not less sophisticated.

I believe the failure to achieve the imaging objectives of the LARSE program is born largely of the overly simplistic imaging technique, rather than data quality. More sophisticated imaging techniques offer the potential for improved crustal imaging by positioning the reflected energy in space before stacking, and using the structure of the recorded wavefield to discriminate between signal and noise.

Prestack wave equation depth migration has become the tool of choice for exploration seismic imaging in areas of complex velocity variation (Gray *et al*. 2001). This technique more faithfully models the complex wavefields than the Kirchhoff technique in these

situations. For crustal scale reflection imaging, prestack wave equation migration offers two other significant advantages over Kirchhoff imaging.

First, wave equation imaging is accomplished by downward extrapolation of the recorded wavefield and a modeled source wavefield. Imaging is accomplished by correlation of the two wavefields at every potential image point. Wavefield correlation is a critical tool for deep crustal imaging, not just for positioning the reflected energy in space, but for detecting weak signal in the presence of noise. Secondly, wave equation algorithms can be easily adapted to image each frequency of the input data independently. By doing so, the imaged components can be recombined after migration, allowing the imaging response as a function of input bandwidth to be determined.

The imaging strategy used here was designed to deal with several issues inherent in the LARSE surveys in particular and crustal surveys in general. First, accurate velocity information is difficult to determine from the reflection data. To provide velocity models for the depth imaging, regional crustal models derived from earthquake tomography were used. Since these models are regional, and do not contain significant detail, first arrival tomography was used to update these models so that they are consistent with the recorded data. Second, migration was carried out in the shot domain. Since shot spacing is coarser than the receiver spacing, the shot domain offered the most complete recorded wavefield for imaging. Third, the imaging effort was concentrated in the low end of the frequency

spectrum. Low frequency components of the wavefield offered the best chance for deep target imaging and are less affected by imaging errors.

My thesis is that prestack wave equation migration can be adapted for use in crustal scale reflection surveys and that it is an effective tool to substantially improve the imaging of these data sets. I will demonstrate this by application of this process to two crustal scale reflection surveys from the LARSE program. To the best of my knowledge, this is the first application of this technique to a crustal reflection survey and the first depth images produced from the LARSE surveys. I will show improvement in the images over those previously reported, and verify my results by comparison to two other data sources: local earthquake activity, and teleseismic imaging studies.

The following chapters will demonstrate my thesis as follows: Chapter 1 introduces the LARSE program, the two data sets used in this study, and reviews the imaging previously attempted with them. Chapter 2 discusses the imaging velocity models and the details of their construction. Chapter 3 discusses the wave equation imaging algorithm and presents synthetic model results to verify of its application to deep crustal imaging. Chapter 4 presents the depth images and demonstrates the validity of my results through comparisons to independent data sets and demonstrates improvement over previous work in the area. The dissertation concludes with recommendations for further work on this topic.

# Chapter 1 - Los Angeles Regional Seismic Experiment

The Los Angeles Regional Seismic Experiment (LARSE) was a joint study of the crustal structure of southern California conducted by the United States Geologic Survey (USGS), and the Southern California Earthquake Center (SCEC). From 1993 to 1999, a series of passive and active seismic surveys were carried out with the objective of better understanding the crustal structure and tectonics in the Los Angeles region in the hopes that it would lead to better earthquake hazard assessment.

This study uses two of the data sets collected by the LARSE program, both active source land lines. The first was collected in 1994 along Line 1, a line running 165 km from Seal Beach northeast through the Los Angeles Basin, the San Gabriel Mountains and the Mojave Desert (see Figure 1 ). The second was collected in 1999 along Line 2, a line running 150 km northward from Santa Monica Bay into the western Mojave Desert.

The locations of both lines were selected: 1) to cross the Transverse Ranges as close to perpendicular to geologic strike as possible, 2) to pass near recent moderate earthquakes, 3) to pass through open areas in the densely populated Los Angeles Metropolitan area to reduce background noise, and 4) to follow routes that afford access through the Transverse Ranges.

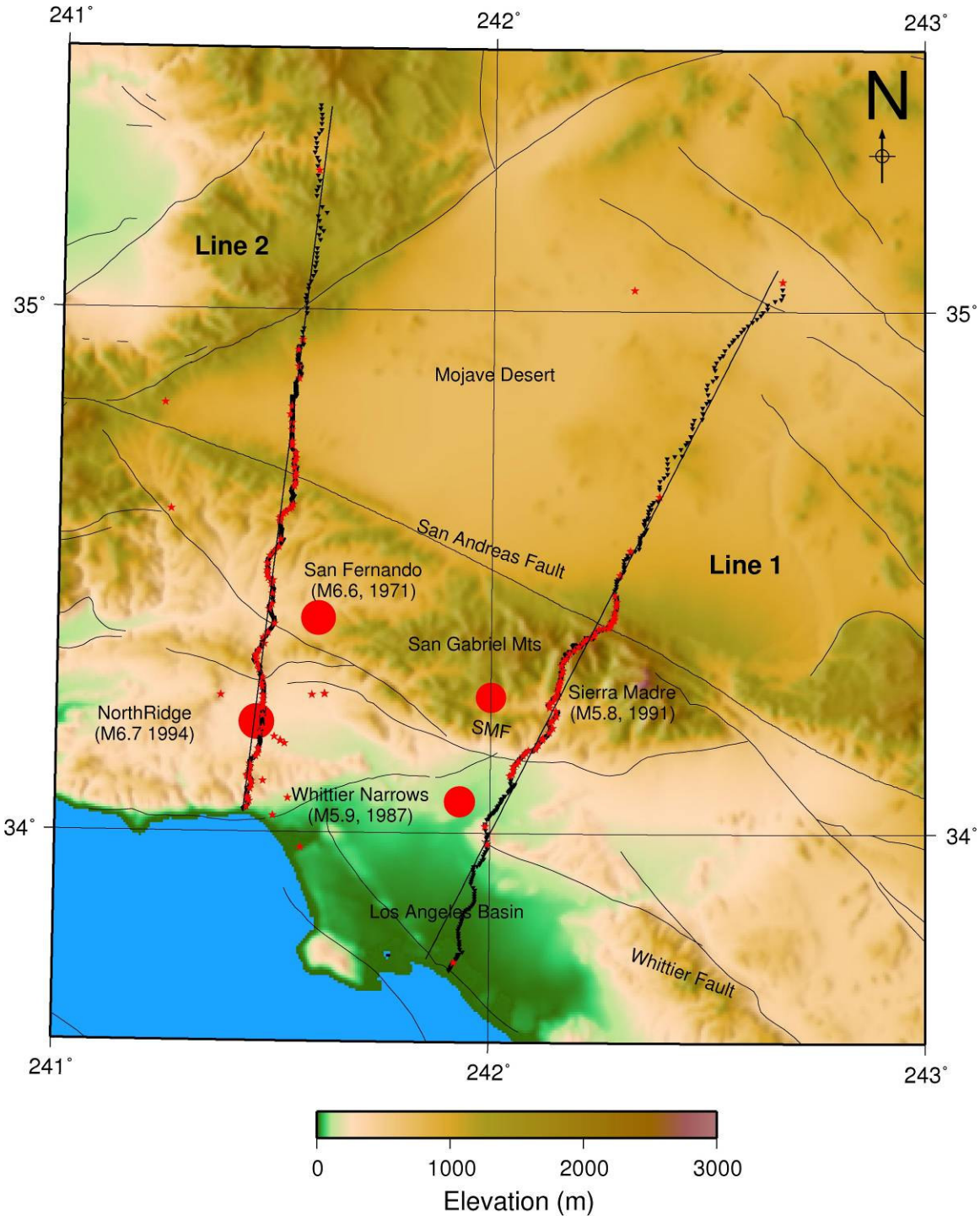


**Figure 1 – Map of southern California showing locations of LARSE Lines 1 and 2. Shot locations shown in red, receiver locations in black. Major faults and geographic areas annotated along with four recent earthquakes.**

Additional phases of the LARSE program included passive surveys along Line 1 in 1993 and again in 1997, a passive survey along Line 2 in 1998-1999 (Kohler *et al*., 1996 and Fuis *et al*. 2001), and a pair of marine reflection surveys along the offshore extensions of Lines 1 and 2 (Brocher *et al*., 1995).

Both land surveys were designed with dual goals, to produce shallow high resolution data for fault delineation, and lower resolution data for imaging crustal scale structures. To achieve these goals the surveys were laid out as combination reflection and refraction surveys. That is, each survey contains a section of relatively high density shot and receiver locations and sections of less dense receiver and shot locations. In both surveys the high density portion of the line is occupied by receiver stations at approximately 100 m intervals with a shot spacing of about 1 km.
Table 1 summarizes the acquisition parameters for these two surveys.

Both surveys were shot using a stationary array. Apart from occasional equipment failures, all stations were active for all shots. All stations employed single sensors, no arrays were used. Approximately one third of the stations on each line were occupied by three component recorders. Only the vertical components from these stations were used in this work.

A wide variety of instrumentation was used in the acquisition of both data sets. Low frequency units (PRS1 and PRS4 recorders coupled with 2 Hz geophones) were laid out

along the entire line. Higher frequency units (Reftek recorders with 4.5 Hz geophones and SGR recorders with 8 Hz geophones) were concentrated in the denser reflection portions of each line. The assignment of instrument type to a station along the line was designed to create as even a distribution as possible.

The 1994 survey along Line 1 also included four additional receiver stations located on Santa Catalina and San Clemente Islands. As these stations were significantly off the main survey line, the data recorded at these stations were not used here. Likewise, three of the recorded shots were quarry blasts located 30 km offline, and were not used here.

The 1999 survey along Line 2 included five auxiliary lines laid out in the San Fernando Valley. These were short (10-25 km) receiver lines running nearly perpendicular to Line 2, along with 12 shot points scattered among these lines. The traces recorded along the auxiliary lines and the shot records from the offline shot points were not used here.

| Survey | 1994 Line 1 | 1999 Line 2 |
|---|---|---|
| Line length | 165 km | 150 km |
| Dense portion | 40-90 km | 0-90 km |
| Number of stations | 622 | 961 |
| Station spacing<br>Dense portion<br>Sparse portion | <br>~100 m<br>200-1000 m | <br>~100 m<br>300-1500 m |
| Number of shots | 65 | 93 |
| Source | ammonium-nitrate | ammonium-nitrate |
| Source size | 5-2722 kg | 5-1818 kg |
| Source spacing<br>Dense portion<br>Sparse portion | <br>~1 km<br>variable | <br>~1 km<br>variable |
| Record length | 60 s | 60 s |

**Table 1- Summary of acquisition parameters for LARSE Lines 1 and 2.**

## *Data quality*

The quality of the raw records from both surveys is typical of deep crustal surveys, that is to say - poor. Very few potential reflection events can be seen. The records are dominated by surface waves and direct arrivals since the survey was acquired without sensor arrays.

Figure 2 shows the field record from shot-point 8260 from Line 1. This shot was acquired in the San Gabriel Mountains; it is typical of the quality of the data in central portion of this survey which is generally the best data in the survey. The record has had a 0.5 Hz to 8 Hz band-pass filter and a median AGC with a 3 second gate length.

The P-wave first arrival breaks (P) are well defined in the dense central portion of the record and can be traced in to the sparser receiver areas. A low frequency Rayleigh event (R) can be seen in the -20 to 0 km offset range. Back-scattered Rayleigh (RR) can be seen in the -15 to -5 km offset range. Between 7.5 and 12.5 seconds (in Figure 2) a series of higher frequency hyperbolic events ($PP_1$-$PP_3$) are apparent. Previous investigators (Ryberg and Fuis, 1998) have interpreted these events as mid-crustal reflections. However, frequency and moveout analysis suggest these are in fact reflected direct arrivals, not primary reflections.

Figure 3 shows a field record from the Line 2 survey with the same filter and gain control as the previous figure. This shot record was acquired near the San Andreas Fault on the southern margin of the Mojave Desert. Events similar to those in Figure 2 can be

identified in this record. In general, the data quality in the 1999 survey was marginally better that the 1994 survey.

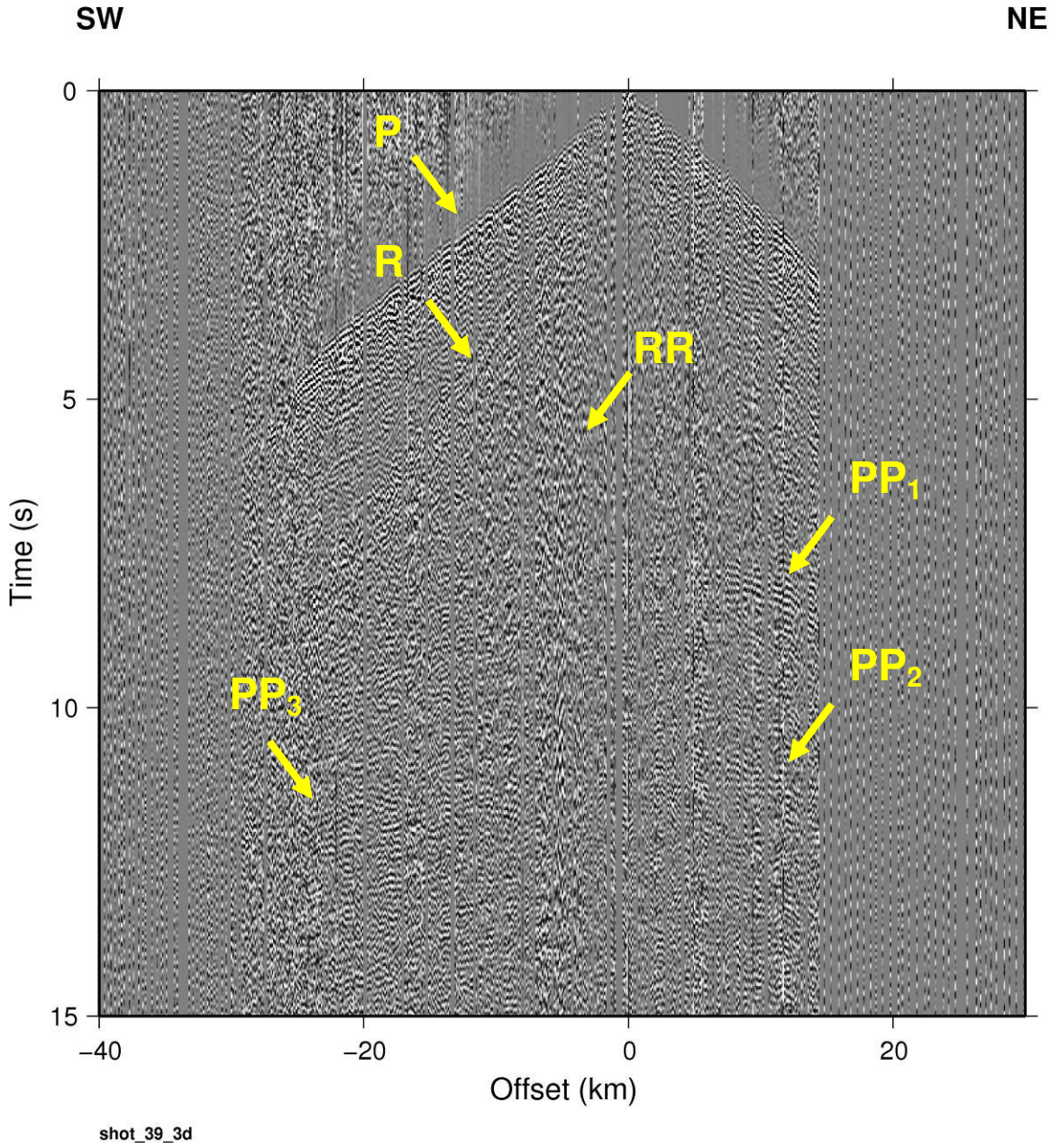


**Figure 2 - Field record from Line 1 shot-point 8260 with AGC and band-pass filter applied. Prominent events: P – P arrival, R – Rayleigh arrival, RR- back-scattered Rayleigh wave, PP – P reflections.**

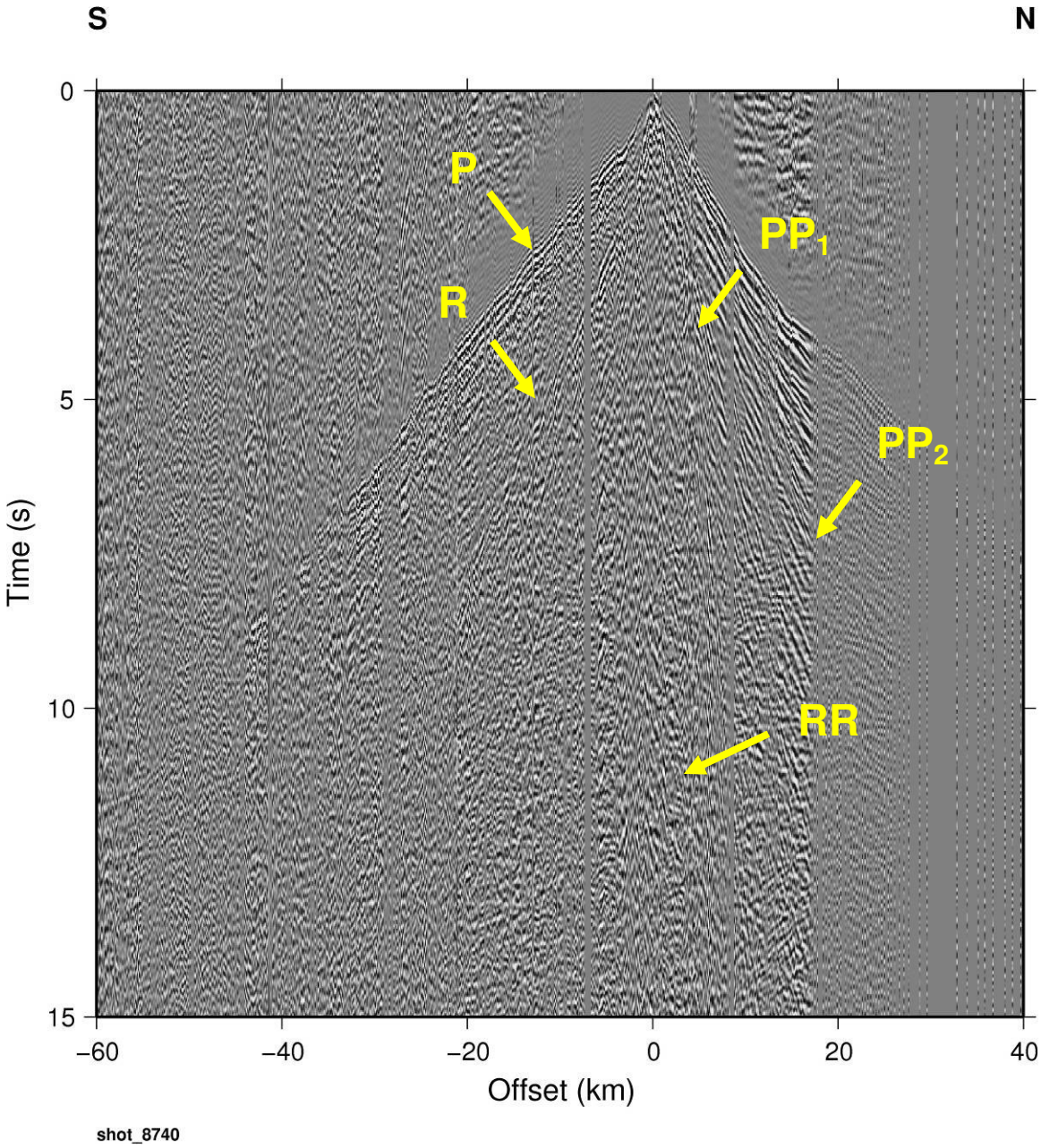


**Figure 3 - Field record from Line 2 shot-point 8740 with AGC and band-pass filter applied. Prominent events: P – P arrival, R – Rayleigh arrival, RR- back-scattered Rayleigh wave, PP – P reflections.**

## *Previous work in the LARSE area*

The first published reflection images from Line 1 were reported by Fuis *et al*. in 1996, revised versions were published in Ryberg and Fuis (1998). In these two studies, the imaging technique consisted of static replacement through the first 5 km of the near surface, NMO and CMP stack of trace envelopes, followed by line interpretation of the reflection events and constant velocity migration of the interpretation. The imaged sections obtained from this process are shown in Figure 4 and Figure 5. These two papers also introduced and developed the concept of the so-called "San Gabriel Bright Spot", a zone of high amplitude events interpreted as a mid-crustal detachment zone. Fuis *et al*. (1999, 2001b) continued to use the same technique to produce new images and interpretations for the Line 1 data; however, there was no significant improvement in the imaging. Fuis *et al*. (2003) applied the same methodology to produce reflection images for the data collected along Line 2. Two of their figures are shown as Figure 6 and Figure 7.

Other work using these data sets focused on techniques using refraction events. Lutter *et al*. (1999) used tomographic inversion of first arrivals recorded along Line 1 to produce near surface (< 10 km depth) velocity models. They interpreted small scale features in their velocity model and claimed to have imaged the Sierra Madre fault zone and Vincent Thrust fault, two major faults in the central San Gabriel Mountains.

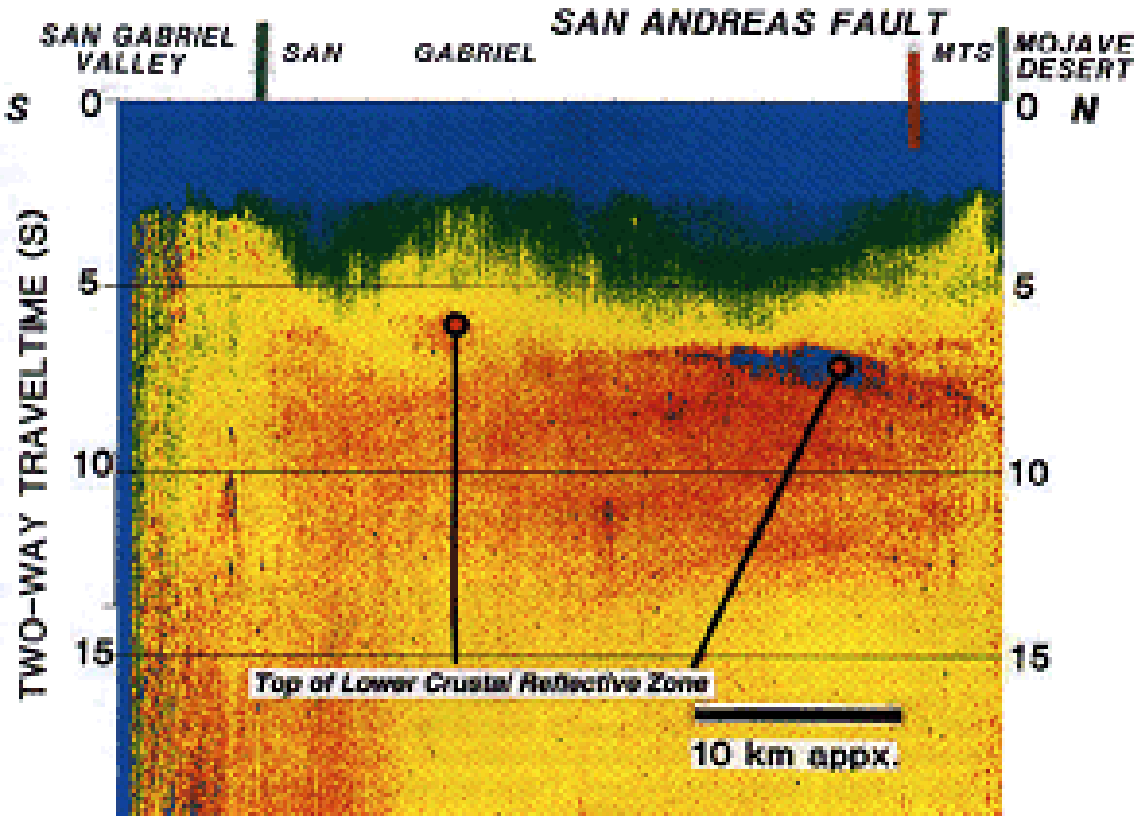


**Figure 4 - Trace envelope stack of Line 1 (Figure 3 from Fuis *et al*., 1996). High amplitude events were interpreted as the "San Gabriel Bright Spot", a mid crustal detachment zone.**

Fuis *et al*. (2001a) used reflected refractions from the Line 1 data to attempt to locate the Vincent Thrust by forward and inverse modeling of travel times. They claim to have located a reflector in roughly the right position and attitude to be the Vincent Thrust; however, the reflector appeared to be too deep to agree with the known surface geology.

Two separate investigations using different parts of the LARSE data reported very different results for the crustal thickness along Line 1. Godfrey *et al*. (2003) combined the refraction data collected along Line 1 with the marine extension of this line to produce a velocity model down to a depth of 40 km via tomographic inversion. Their

model showed a gradual landward thickening of the continental crust (from 20 km thick offshore to 30 km thick in the San Gabriel Mountains), and a pronounced sag in the base of the crust at the San Andreas Fault. Zhu (2000 and 2002) used the passive data collected along Lines 1 and 2 to invert the teleseismic waveforms for P to S reflectivity. The PS reflectivity sections for Line 1 show the continental crust thinning towards the plate boundary with a distinct discontinuity at the San Andreas Fault.

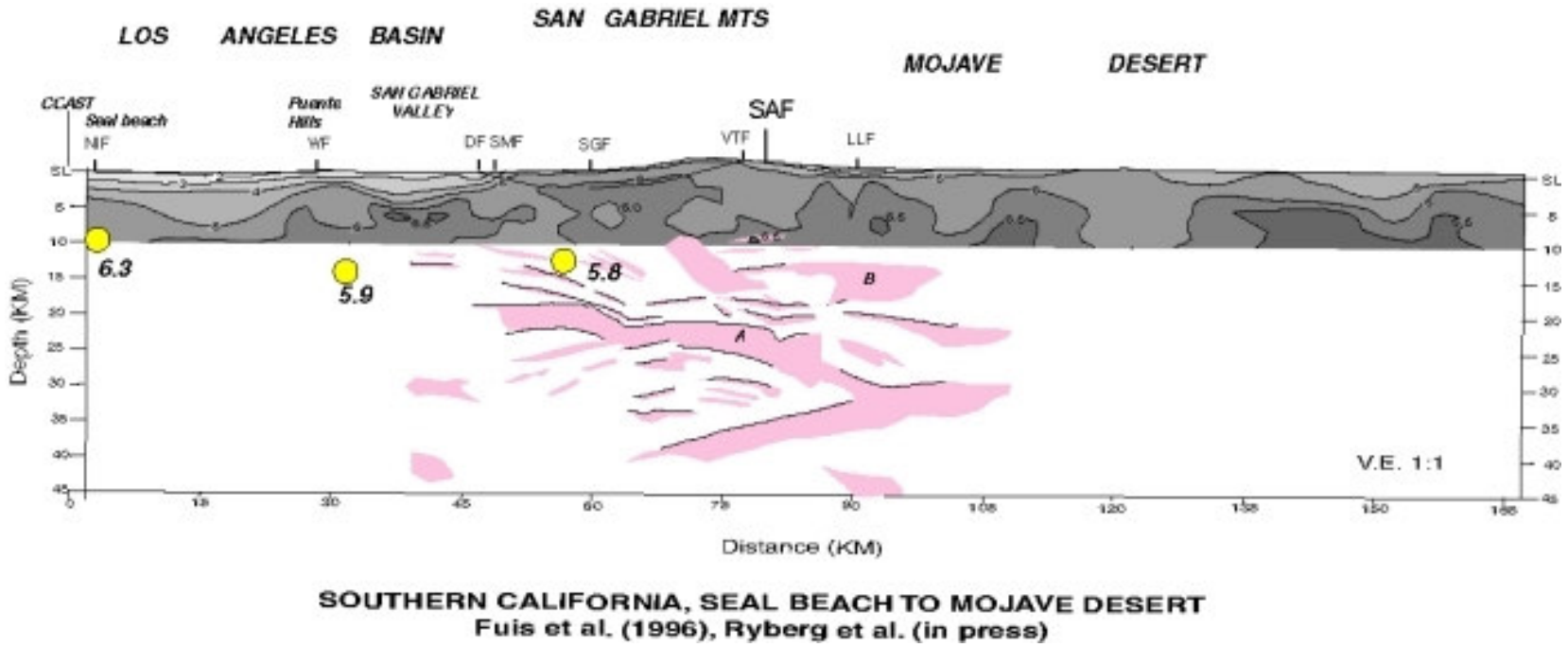


**Figure 5 - Time interpretation of LARSE Line 1 (Figure 2 from Fuis *et al*., 2001b). Upper 10 km of section (in gray) show interval velocity derived from first arrival tomography. Interpreted zones of reflection events shown in pink, projected hypocenters of nearby significant earthquakes shown in yellow.**

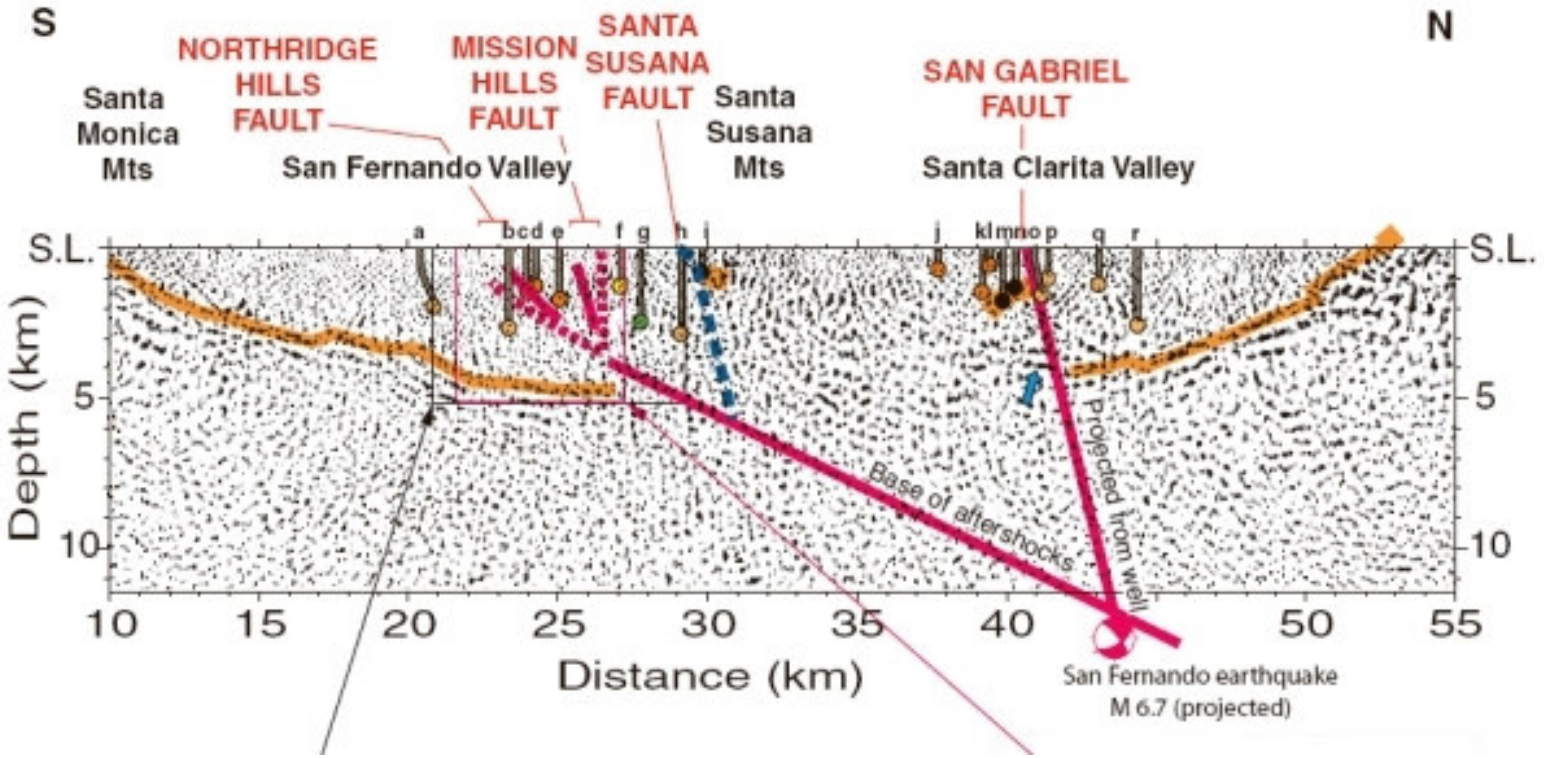


**Figure 6 - Poststack depth migration of southern half of Line 2 data (Figure 2 from Fuis *et al*., 2003). Well penetrations shown as locations a-r, interpreted base of sedimentary basin shown in orange. Projected position of San Fernando and San Gabriel fault zones shown in red.**

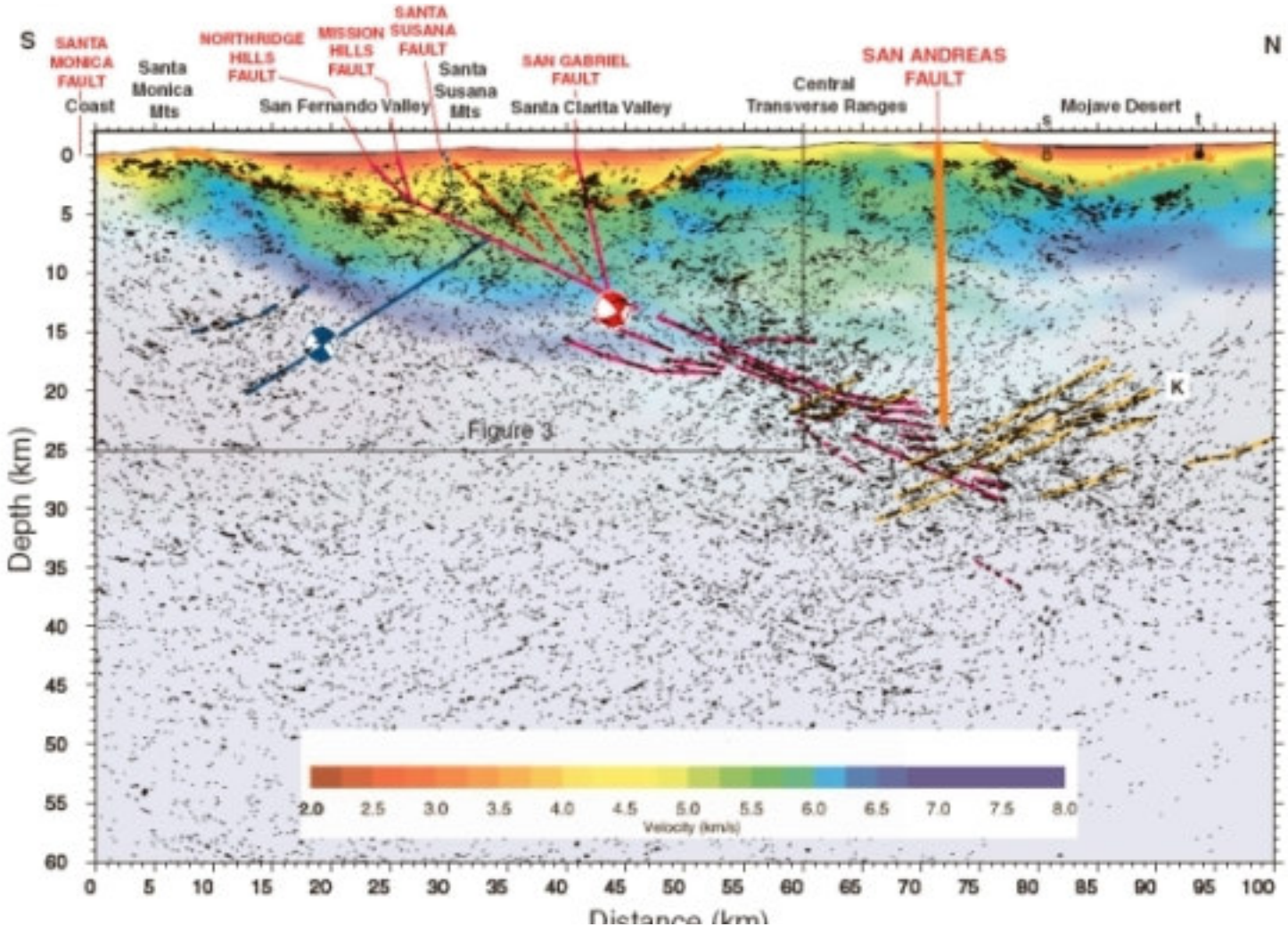


**Figure 7 – Depth migrated line interpretation from Line 2. (Figure 4 from Fuis *et al*., 2003). Tomographic velocity model shown in color in the upper portion of the section. Inferred position of Northridge Fault zone in blue, San Fernando Fault zone in red.**

# Chapter 2 - Velocity modeling

The imaging velocities for both LARSE lines were constructed from first arrival tomography updates of regional crustal velocity models derived for earthquake seismology. The difficulty in reliably identifying reflection arrivals prevented velocity estimation directly from the reflection data. However, refraction arrivals in both lines were readily identifiable and were used to improve the accuracy of the shallow velocity models. Four velocity models were constructed for Line1 to test the effects of the various regional models. Since there proved to be little difference in the images computed from these models, a single updated model was created for Line 2.

## *Tomography methodology*

### Slowness parameterization

The slowness (reciprocal velocity) parameterization used here follows the multi-scale framework of Zhou (2003). The multi-scale framework consists of multiple sets of slowness parameters. Each set spans the entire model and represents an incremental slowness field at different spatial scales or wavelengths. Thus the modeled slowness at a given point in the model is the sum of the slowness increments from all the sets in the framework.

In this implementation, the incremental slowness parameters within each multi-scale set represent values at nodes on a regular grid, and the scale of the set is defined by the

spacing of the nodes. The incremental slowness for a given point in the model is interpolated from the nearest nodes within the set. The node representation has two purposes. First, it assures a minimum level of smoothness to the slowness models. Second, it reduces the possibility of introducing linear relations between the columns of the tomography kernel and prevents further deterioration of the conditioning of the linear problem.

## Ray tracing

Ray tracing was done with the Moser (1991) network based shortest path algorithm. It is well suited to tomography applications since both travel time and ray paths are computed simultaneously. It is also well suited to situations where rays are traced from one source location to many receivers since there is very little additional cost in extracting rays once a source has been traced to all points. Furthermore, the algorithm assures that rays are computed to each point in the model (no shadow zones).

The main disadvantage to this method is that the rays are limited to the paths between points on a regular grid. This can limit the overall accuracy of a given ray. Accuracy can be improved by reducing the grid spacing and increasing the number of allowable paths to neighboring grid points, but at the cost of additional memory and run time.

In this implementation, travel time from a point to its neighbors in the network is computed from the length of the connecting segment and the interpolated slowness at the

midpoint of the segment. For a sufficiently smooth slowness field, this will provide an accurate approximation of the integral of the slowness along the connection. Since the slowness model is kept smooth by interpolation between slowness nodes, travel time computation will remain accurate as long as the connection distance is kept smaller than the smallest distance between slowness nodes.

For this implementation, two other issues must be addressed. The first is topography. To prevent the algorithm from finding rays which might exit the earth and travel through the air, points in the grid above topography are flagged as dead; no connections to these nodes are allowed, they are essentially removed from the grid. The second issue to be addressed is the locations of the starting and ending points of the ray. Since the surveyed locations of the source and receiver points will not in general fall on the regular grid, off-grid nodes are introduced for these locations. To start the algorithm, the source node is created and located in its off-grid position. Straight ray travel times and connections to the nearest neighbor grid points are computed to seed the algorithm. Likewise, once the grid has been populated, a receiver point is located in its off-grid position. Travel times from its nearest neighbors are examined, the minimum travel time is selected and a connection is made to the neighbor which supplied the minimum travel time.

## Linear Solution

Once the rays have been traced through the current slowness model, the next step is to construct and solve the local linear problem for the slowness update. The basic linear problem is shown in Equation 1:

(1) $$\Delta t = A\ \Delta s\ ,$$

where $\Delta t$ is the vector of differences between measured and raytraced traveltimes, $\Delta s$ is a vector of slowness perturbations, and $A$ is the tomography kernel, a matrix which relates the change in slowness to the travetime errors.

In order to reduce the effects of bad travel time picks, the travel time errors, $\Delta t$, are examined in each iteration to identify and remove outliers. The standard deviation for all travel time errors is computed and any travel time errors which exceed a specified multiple of the standard deviation, are flagged and not used in the current iteration. In this fashion, picks which might be deemed outliers in early iterations can be redeemed and used in later iterations.

The tomography kernel matrix ( $A$ ) is formed from the traced ray paths and the slowness parameterization. Each ray extracted from the Moser algorithm consists of a series of linear segments connecting receiver and source locations. For each segment, the midpoint of the segment is used to compute a row vector of bilinear interpolation coefficients from

the surrounding nodes in all slowness multi-scale sets. The row vector of all coefficients is multiplied by the segment length and added to the appropriate row of the kernel matrix.

To improve the conditioning of the linear inversion, and to impose some constraints on the solution, two types of regularization are used. A Laplacian operator ( $L$ ) acting on the slowness perturbation ( $\Delta s$ ) was added to the system of equations to minimize the roughness of the solution. The Laplacian operator consists of two, three-point, second difference operators centered at each slowness node; one oriented horizontally, the other vertically. The second regularization is a minimum norm constraint ( $I$ ) on the slowness perturbation. This is intended to smooth the solution and limit the total amount of variation. The augmented linear problem is shown in Equation 2:

$$\Delta t^{+} = \begin{bmatrix} \Delta t \\ 0 \\ 0 \end{bmatrix} = \begin{bmatrix} A \\ \frac{\lambda_L \|A\|_F}{\|L\|_F} L \\ \frac{\lambda_I \|A\|_F}{\|I\|_F} I \end{bmatrix} \Delta s = A^{+} \Delta s , \tag{2}$$

where $\Delta t^{+}$ is the augmented travel time error vector and $A^{+}$ is the augmented tomography kernel.

Both the operators $L$ and $I$ are given weights ( $\lambda_L$ and $\lambda_I$ ) at run time. The regularization operators are scaled relative to the tomography kernel using the Frobenius norm and the weighting factors. As the tomography iterations proceed, the weighting factors can be reduced according to a schedule driven by the trust-region algorithm. The intent here is to

relax the constraints as the trust-region algorithm determines that the iterations are nearing a solution.

Prior to solving the augmented system (2), a preconditioning matrix $C$ is introduced. This serves two purposes: to reduce the size of the linear system by removing any zero columns in the tomography kernel, and to further improve the conditioning of the system by normalizing the power of each non-zero column. Zero columns arise in portions of the slowness model not sampled by the ray field. The slowness parameters in these areas are unconstrained and should be removed from the system to prevent incidental update. The fully preconditioned augmented linear system (3) is then solved using LSQR (Paige and Saunders, 1982).

(3)
$$\Delta t^{+} = A^{+} C \Delta s'$$
$$\Delta s = C \Delta s'$$

## Trust-region globalization

The final step in each tomographic iteration is to evaluate the new perturbation within a trust-region framework. The trust-region algorithm is a standard method of monitoring the performance of a local linear approximation to a non-linear problem and improving the convergence characteristics of the algorithm (Fletcher, 1980). In terms of the seismic tomography problem, the basic idea is to limit the overall size of slowness perturbation in each iteration. The maximum allowable perturbation in a given iteration is dependent on

the recent performance of the linear approximation. The trust-region framework is well suited to tomography since it is fairly easy to implement and the information needed to assess the linear approximation can be used directly for the next iteration. In this implementation, the algorithm proceeds as follows:

The norm of the slowness update ( $\Delta s$ ) is compared to the norm of the current slowness ( $s_i$ ), if this ratio exceeds the trust-radius ( $\rho_{tr}$ ), the length of the slowness update is limited by the trust-radius (4). A tentative solution ( $s_{i+1}$ ) is formed and a new set of rays are traced using this solution.

$$(4) \qquad if \begin{cases} \frac{\|\Delta s\|}{\|s_i\|} \le \rho_{tr}, & s_{i+1} = s_i + \Delta s \\ \frac{\|\Delta s\|}{\|s_i\|} > \rho_{tr}, & s_{i+1} = s_i + \Delta s \frac{\rho_{tr}\|s_i\|}{\|\Delta s\|} \end{cases}$$

The local linear approximation is evaluated by comparing the reduction in travel time error predicted by the linear system to the reduction computed from the new set of rays (5).

$$(5) \qquad \gamma = \frac{\|\Delta t(s_i)\| - \|\Delta t(s_{i+1})\|}{\|\Delta t(s_i)\| - \|\Delta t(s_i) - A\Delta s\|}$$

If this ratio ( $\gamma$ ) is small (<.01), then the linear approximation has predicted a larger decrease in the objective function than was actually found. In this case the trust-radius is

too large, so the trust-radius is halved, a new tentative solution is formed and ray traced, and the ratio is re-evaluated until an acceptable value (>.01) is found. If the ratio is large ($>.9$), the objective function was reduced more than the linear approximation predicted. In this case, the linear approximation is deemed a good one, and the trust-radius is doubled to allow a larger update in the next iteration. Once an acceptable ratio is found, the tentative solution is accepted as the solution for this iteration, and the next iteration can begin using the rays just traced in the ratio evaluation.

In general, I have found that for seismic tomography the trust region is an active constraint only in the first few iterations. In these early iterations, the misfit between the picked travel times and the modeled travel times is large and tends to produce large slowness perturbations. Limiting the size of the allowable perturbation prevents early iterations from violating the small perturbation assumption in the linearization of the tomography problem and diverging too far from the initial model. After these early iterations, an initial trust radius of 1% expands to 4% and remains stable throughout the remaining iterations.

In addition to monitoring and adjusting the trust-region size, this algorithm is called on to regulate the regularization constraints. In this implementation, each time an acceptable solution is found, the weighting factors on the regularization operators are reduced by a fixed percentage.

## Residual Delays

The final step in the tomographic algorithm is to compute surface consistent delays for each shot and receiver location from the final set of residual travel times. These represent slowness features observable in the picked travel times but not contained in the model. Generally these would correspond to near surface features too small to be resolved in the model. These delays can then be used to correct the trace data as static shifts to account for the un-modeled features. A positive delay computed here corresponds to an increase in slowness not included in the model, and the correction would be applied as an advance to the trace data.

## Tomography Parameters

Ray trace parameters were selected by comparing travel times through a constant velocity medium from the Moser algorithm to analytic travel times. A 165 km long by 53 km thick model with a constant velocity of 6 km/s was constructed and ray paths traced from a single source at the origin of the model. Travel times were extracted on a 1 km x 1 km grid and the average percentage error over the entire model was computed for various raytrace node spacing and levels of connectivity. The level of connectivity is expressed as the number of neighboring nodes connected to any node. In a 2D grid, the first level of connectivity would be the 8 nodes immediately adjacent (vertically, horizontally and diagonally) to the node. The next level would add the 16 nodes surrounding the inner 8 for a total of 24. Likewise, the third level consists of 48 nodes, and fourth contains 80.

Figure 8 shows the effect of the level of connectivity on the average travel time error for three different node increments. Each increase in the connectivity reduces the average error by approximately half, regardless of node spacing. The relationship between run time and average travel time error is shown in Figure 9. The optimal choice for performance and accuracy would be the point closest to the origin in Figure 9, which is the combination of a node spacing of 2 km and 80 point connectivity. A node network using this parameter combination would have connection paths to the outer nodes of 8-11 km, significantly longer than the smallest slowness scale (5 km x 5 km). A better choice that keeps the outer connection lengths reasonably small is a grid spacing of 1 km and a connectivity of 48. Here the outer connection lengths are 3-4.2 km long, smaller than the smallest slowness grid and more likely to accurately represent travel times through any areas of rapid slowness change. A 1 km x 1 km grid with a connectivity of 48 was used for all tomographic updates.

The initial trust-region size was set to 1%. Both the Laplacian and diagonal damping weights were set to 2; these weights were relaxed by 1% after each successful iteration.

The slowness grid spacing was chosen to allow velocity updates to the shallow section, while preserving the original regional model in the deeper section. The maximum vertical grid spacing was chosen to be 10 km, approximately the maximum depth of penetration for the first arrival rays. Limiting the maximum vertical grid size isolates the deep, unconstrained portion of the model from changes in the shallow section.

The largest scale for the models was chosen to be 165 km long and 10 km thick. This divided each 2D profile into six horizontal slabs, intended to model a background model of mainly vertical variation with a slowly laterally varying component. To allow for medium period lateral variation and retain continuity in the model, another scale of 40 km x 10 km was added. The finest scale introduced into the model is a 5 km x 5 km model, resulting in a total model size of 464 slowness parameters.

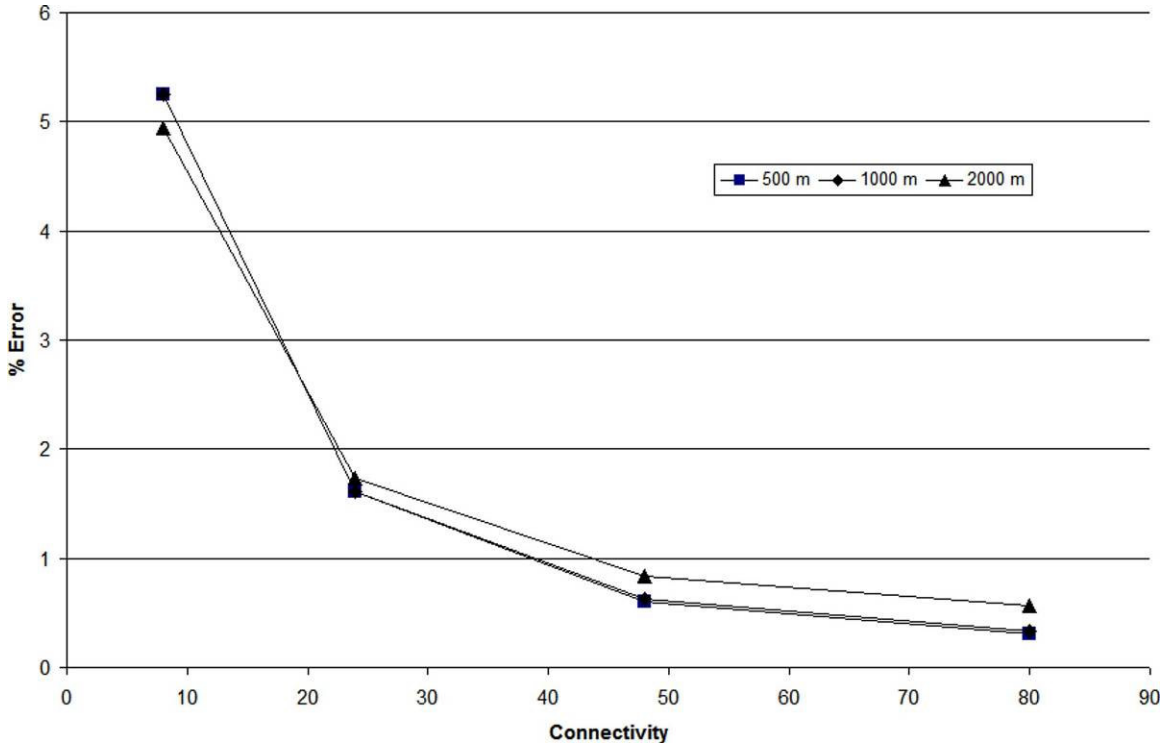


**Figure 8 – Average travel time error as a function of node connectivity and node spacing for Moser algorithm. Error computed from raytraced and analytic travel times through constant velocity. Connectivity is the total number of connections from a node to surrounding nodes in the network. Distances between nodes were varied from 500 m to 2000 m.**

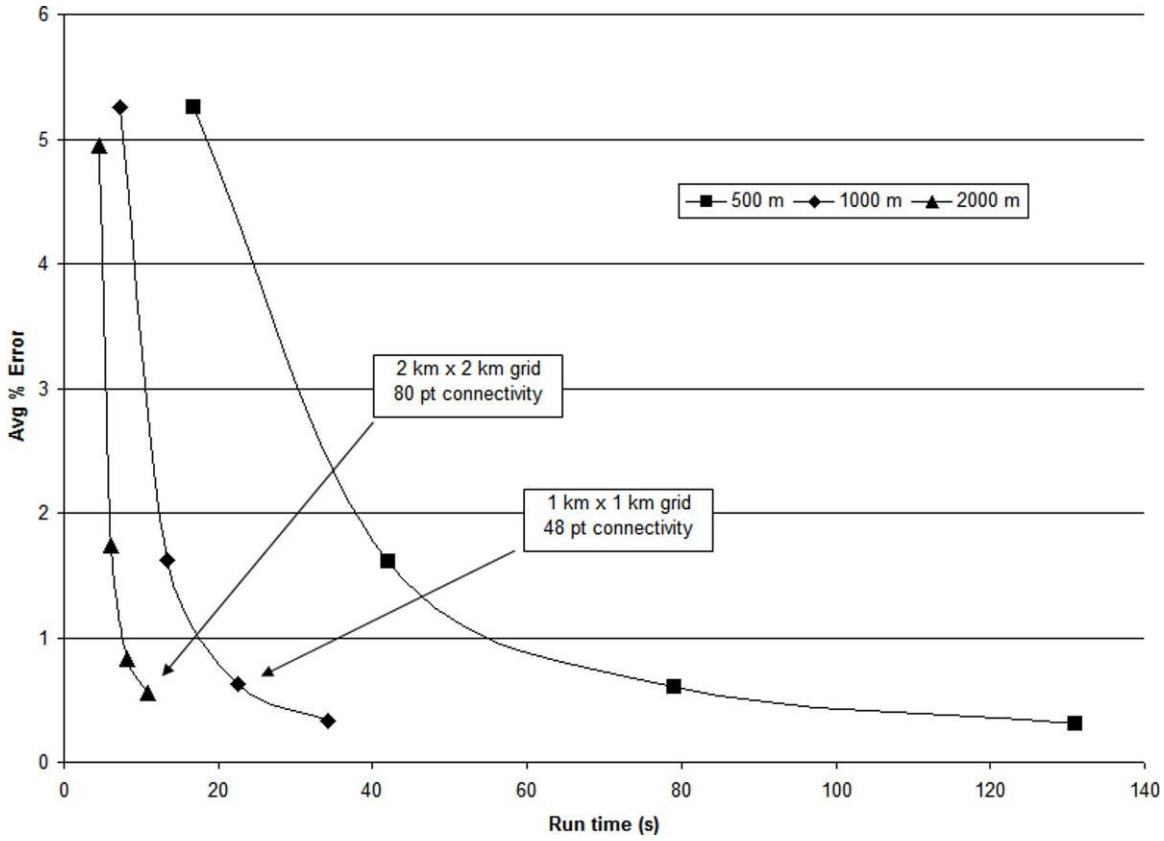


**Figure 9 - Average travel time error and run time as a function of node connectivity and node spacing for Moser algorithm. Same levels of connectivity (8,24,48,80) and node spacing (500 m, 1000 m, 2000 m) used as in previous figure. Two possible choices for optimal (minimal error and minimal run time) parameters noted.**

## Initial Models

Three of the four models created for Line 1 were based on published 3D models of the regional southern California crustal velocity structure: the Hauksson model (Hauksson and Hasse, 1997), the SCEC model (Kohler *et al*., 2003) and the MC3 model (Zhou 2004). All three were derived were derived primarily from tomography of local and teleseismic earthquakes, and consist of 10 km x 10 km x 3 km cells of constant velocity (the smaller dimension is depth). The straight-line 2D profile for Line 1 was used to

extract an interpolated 1 km x 0.2 km 2D profile from each model (again the smaller dimension is depth). The fourth model was a laterally invariant profile constructed from a single depth variant function picked to follow the average trend of the three extracted profiles. The four preliminary models are shown in Figure 10.

To construct an equivalent multi-scale representation of the extracted 2D profiles, the least-squares problem (6) was solved.

(6) $$S_{2D} = (A + \lambda L) s_{ms}$$

$S_{2D}$ is a vector of 1 km x 1 km slowness samples taken from the 2D profile, $A$ is a matrix with each row holding the bilinear interpolation coefficients for the location of a sample in $S_{2D}$, $\lambda L$ is a Laplacian smoothing constraint similar to the one used in the tomography, and $s_{ms}$ is the equivalent multi-scale parameterization. The Laplacian regularization term was added to produce smoother models, since initial attempts at conversion to the interpolated parameterization retained many sharp velocity contrasts that created instabilities in the ray tracing. The weighting parameter ($\lambda$) was set to 2, and normalized in the same fashion as described in the tomography methodology.

The velocity profiles for the four smoothed models from the multi-scale parameterization are shown in Figure 11. The smoothed models retain many of the gross structural features of the 2D extracted models, but do not include the sharp edges created by the constant

cell parameterization. The four models are generally similar; shallow crustal velocities span the range of 5-6.5 km/s, with a transition to mantle velocity (7.5–8 km/s) at about 30 km depth. The MC3 and SCEC and to a lesser degree the Hauksson models show a mid-crustal velocity inversion at a depth of 15-20 km below the San Gabriel Mountains. The near surface velocities in the Los Angeles Basin drop to 3–5 km/s, which is consistent with a sedimentary basin.

Figure 12 shows the initial slowness model constructed from the Hauksson model along with its constituent incremental slownesses. In this figure one can see how the largest scale parameterization (165 km x 10 km) produces a primarily depth dependent background slowness model. The medium scale grid (40 km x 10 km) contains more of the lateral variation in the initial field, while the smallest grid size (5 km x 5 km) is dominated by the high slowness values of the Los Angeles Basin.

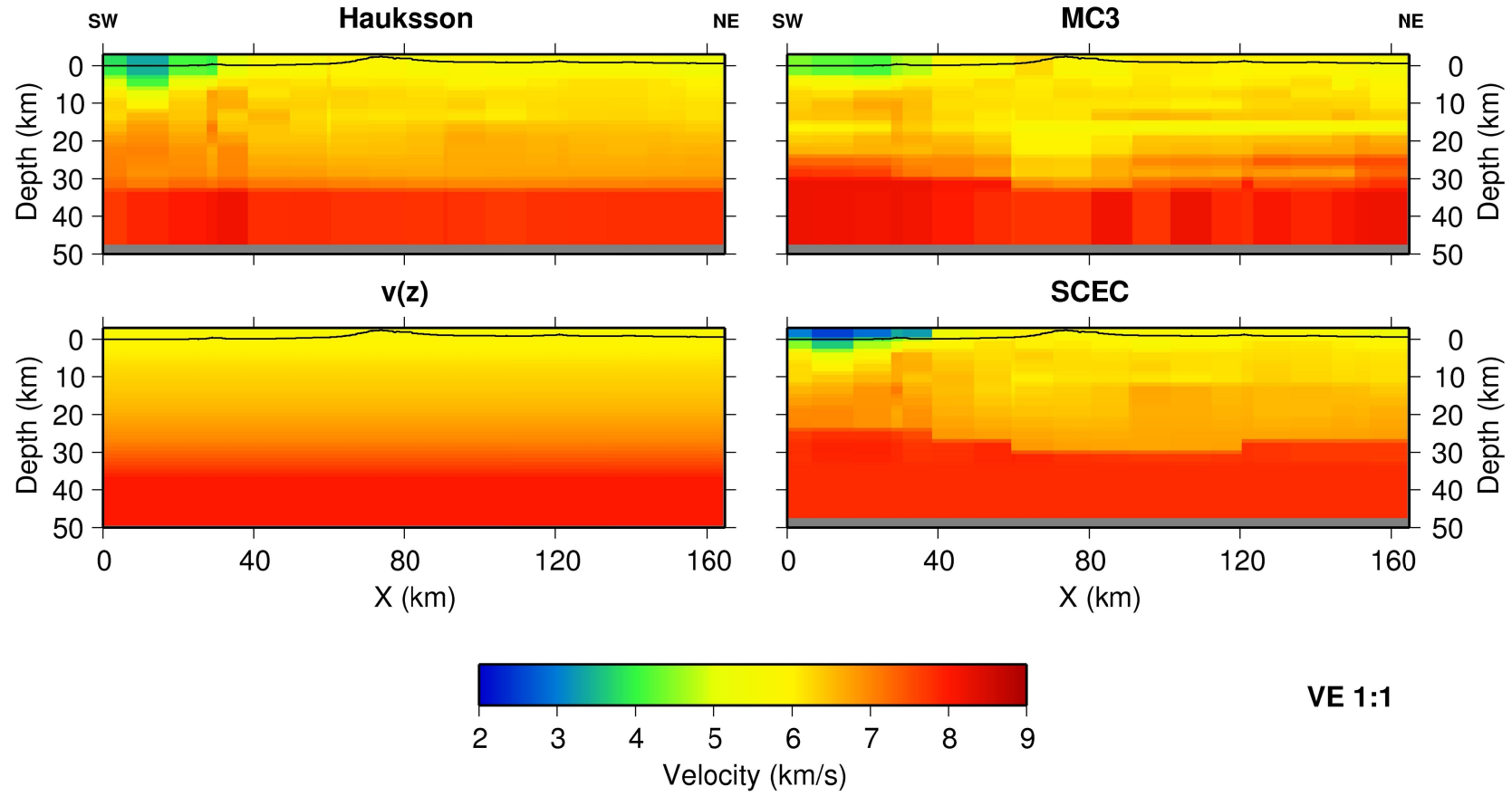


**Figure 10 - Velocity profiles for Line 1extracted from Hauksson, MC3 and SCEC 3D models and laterally invariant control model v(z).**

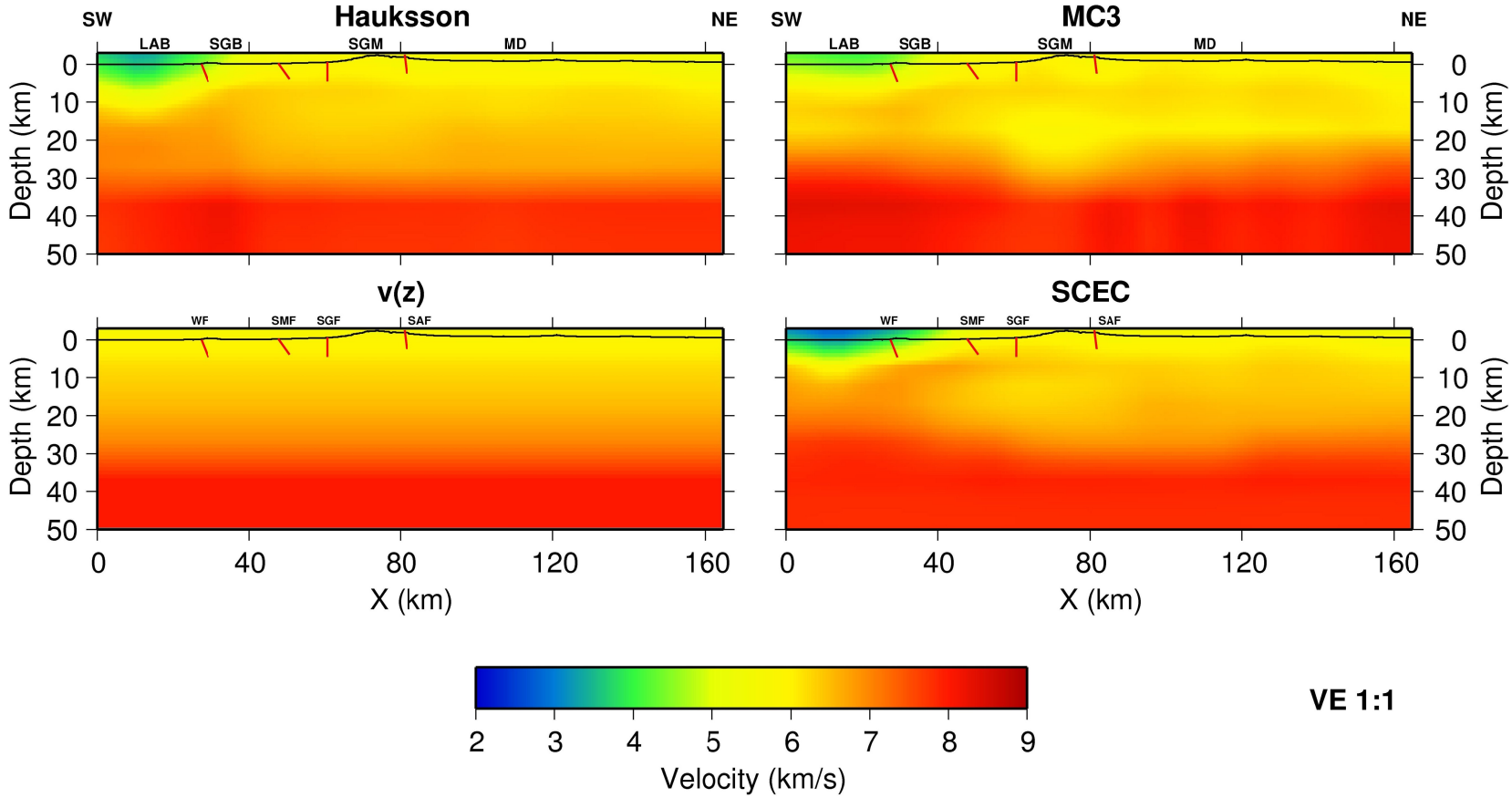


**Figure 11 - Initial smoothed velocity models for Line 1. Black line shows topography along 2D line. Major faults are shown as red lines and labeled in lower two sections (WF- Whittier Fault, SMF – Sierra Madre Fault, SGF – San Gabriel Fault, SAF – San Andreas Fault). Major geographic areas are labeled in upper two sections (LAB – Los Angeles Basin, SGB – San Gabriel Basin, SGM – San Gabriel Mountains, MD – Mojave Desert).**

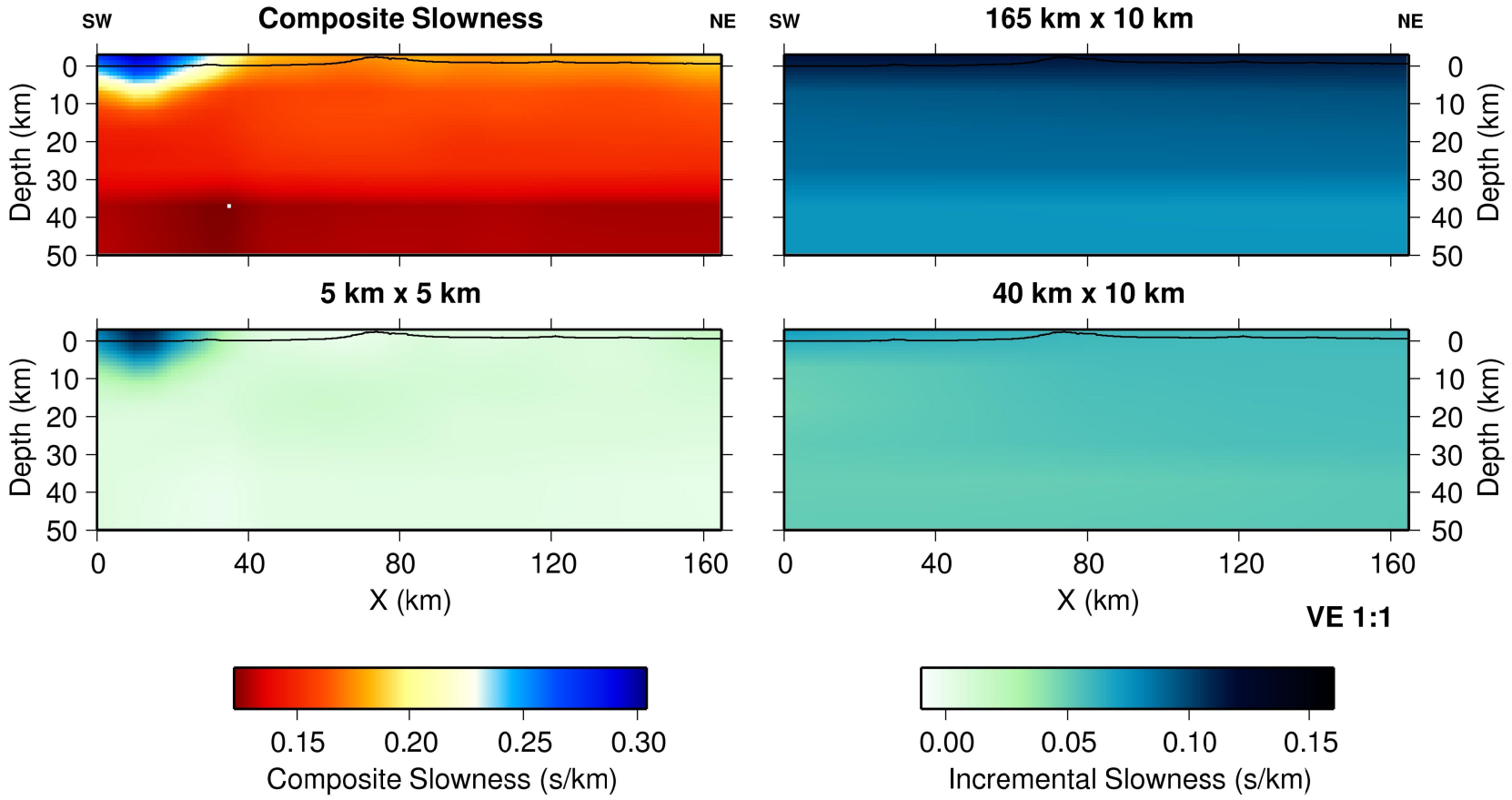


**Figure 12 - Multi-scale slowness representation of initial Hauksson model for Line 1. Composite slowness is the sum of the incremental slowness fields. Dimensions above each incremental slowness field indicate the spacing of slowness nodes within the grid.**

## First Arrivals

First arrival times were manually picked from the trace data wherever the data quality would allow. 20804 first arrival times were picked on Line 1, approximately 55% of the traces. 35387 picks were made on Line 2 or 48% of the total traces. Approximately 95% of the picks survived the editing process, consistent with a normal error distribution and a two standard deviation threshold. Since the editing process rejects picks based on magnitude of difference between picked travel time and modeled travel time, valid picks can be erroneously discarded in early iterations when the slowness model is not well developed. Figure 13 shows the percentage of picks used in the inversion as a function of iteration for each of the four tomography updates on Line 1. In each case, the percentage of picks reaches a minimum in the first or second iteration then steadily increases with each iteration. The total number of picks recovered in this process is small (about 1%), but the increase in the percentage of picks with continued iteration suggests that these picks are associated with areas of change in the slowness model.

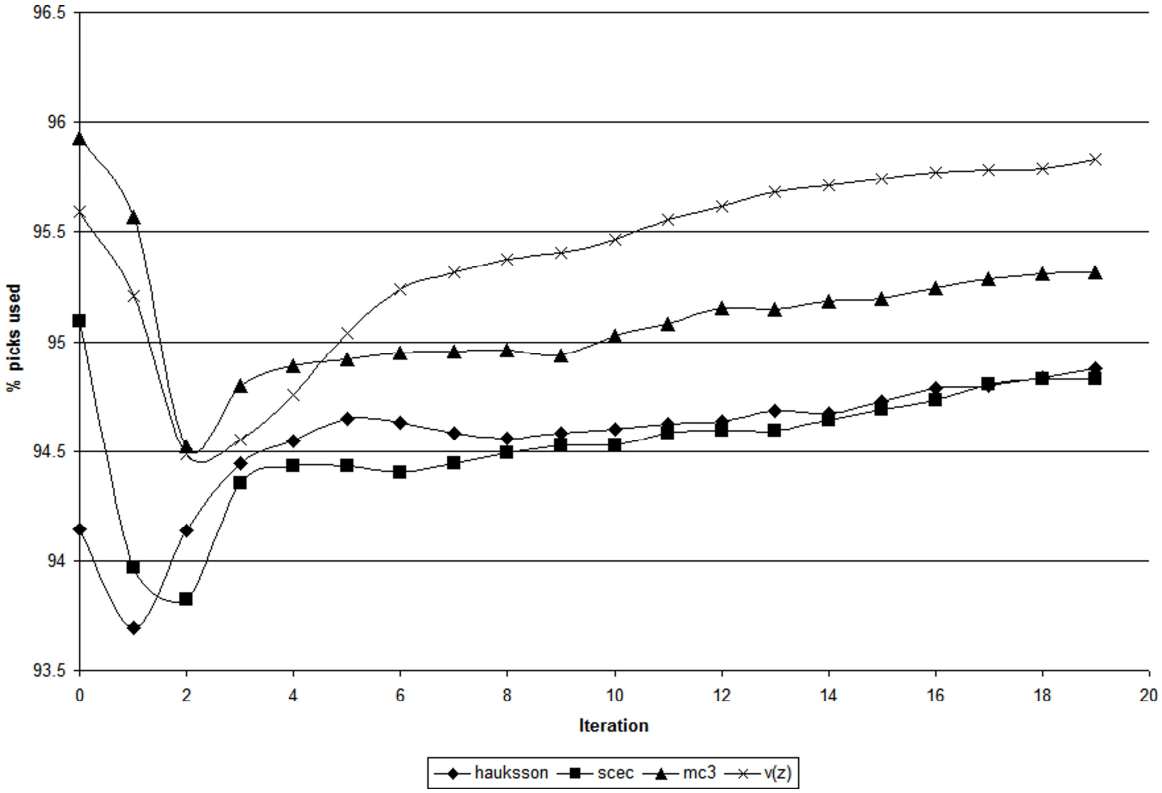


**Figure 13 - Percentage of total picks used after editing versus iteration for the four tomography runs for Line1. After initial decline in first 2-3 iterations, approximately 1% of picks are recovered as model fit improves.**

## *Tomography results*

### Line 1

Each of the four initial models was updated with the same set of first break picks and tomography parameters. The four updated models are shown in Figure 14 along with the residual delays for each in Figure 15. For each model, the tomographic update has converged to a similar model in the uppermost 15 km. A high velocity block (~ 6.5 km/s) is developed below the southwestern flank of the San Gabriel Mountains. The southwestern edge of this block correlates with San Gabriel Fault. Low velocity zones (~

4.5 km/s) are introduced by the tomography in the vicinity of both the Sierra Madre and San Andreas faults. In the uppermost 10 km of the Mojave Desert, the crustal velocity is reduced to 5.0-5.5 km/s in all models. Velocities in the Los Angeles Basin are decreased in all models, but this area remains the area with the greatest differences among models. Below 15 km the initial models remain essentially unchanged. The near surface features in these models are consistent with those found by Lutter *et al*. (1999) and Fuis *et al*. (2001b).

The residual delays provide an indication of the accuracy of the updated models. For all four models, the delays northeast of the Sierra Madre Fault are small and well behaved. The delays in this region are centered on zero and variation is less than 200 ms, indicating the tomographic model largely explains the measured travel times. Southwest of the Sierra Madre fault through the San Gabriel and Los Angeles basins, the residual delays increase rapidly but consistently, reaching a maximum of 500-1300 ms. A large positive static indicates that the velocity in these basins are actually slower than represented in the model. The Hauksson and SCEC initial models have significantly slower velocities in the Los Angeles Basin, and corresponding smaller residual delays. A similar but smaller peak in the residual delay is associated with the San Andreas Fault zone.

The large positive residual delays found in the Los Angeles and San Gabriel basins indicate the tomographic model is faster than the actual velocity in these basins. Lutter *et*

*al*. (1999) show velocity profiles from four wells, one from the northwestern edge of the Los Angeles Basin and three from the San Gabriel Basin. These profiles show shallow interval velocities in the first 4 km increasing nearly linearly with depth from 2 km/s at the surface to approximately 4 km/s at 3 km depth. The modeled basin velocities in the first 3 km are in the range of 3.5-5.5 km/s, significantly faster than the well profiles. The tomography grid was designed to model features 5 km or larger. The rapid near surface increase in sedimentary velocities is likely too small a feature to be adequately represented in the model, and could reasonably explain the range of measured residual delays.

Figure 16 shows the reduction of residual travel time error as a function of iteration for the four tomographic runs. All models achieve the largest reduction in the residual error in the first five iterations then begin a long series of small decreases in residual error. The average change in the slowness model for the later iterations was 0.5%. The algorithm never converged in the sense that the residual error stopped falling, or that the perturbation step approached zero. However, the algorithm was halted after 20 iterations after examining the models produced after each of the later iterations. Subsequent iterations produced localized changes which lead to more instability in the ray tracing.

## Line 2

The 2D extraction, initial model, final model and residual delays from the tomographic update of the Line 2 data are shown in Figure 17. The 2D model was extracted from the Hauksson model and updated with parameters identical to those used in Line 1.

In the final model, two low velocity zones are apparent, one associated with the San Fernando and Santa Clarita Valleys, the other associated with the southern margin of the Mojave Desert. The Central Transverse Range shows a block of fast velocity (6 km/s) overlaying slightly slower velocities (5.5-5.7 km/s) just below. These results correlate well with the velocity model reported by Fuis *et al*. (2003).

The residual delays show a similar pattern to those seen in Line 1. Large positive delays are associated with the San Fernando Valley, most likely due to slow velocities in the near surface below the resolution of the model. The divergence of the shot and receiver delays in the Mojave Desert portion of this line indicate potential unresolved velocity structure in the model.

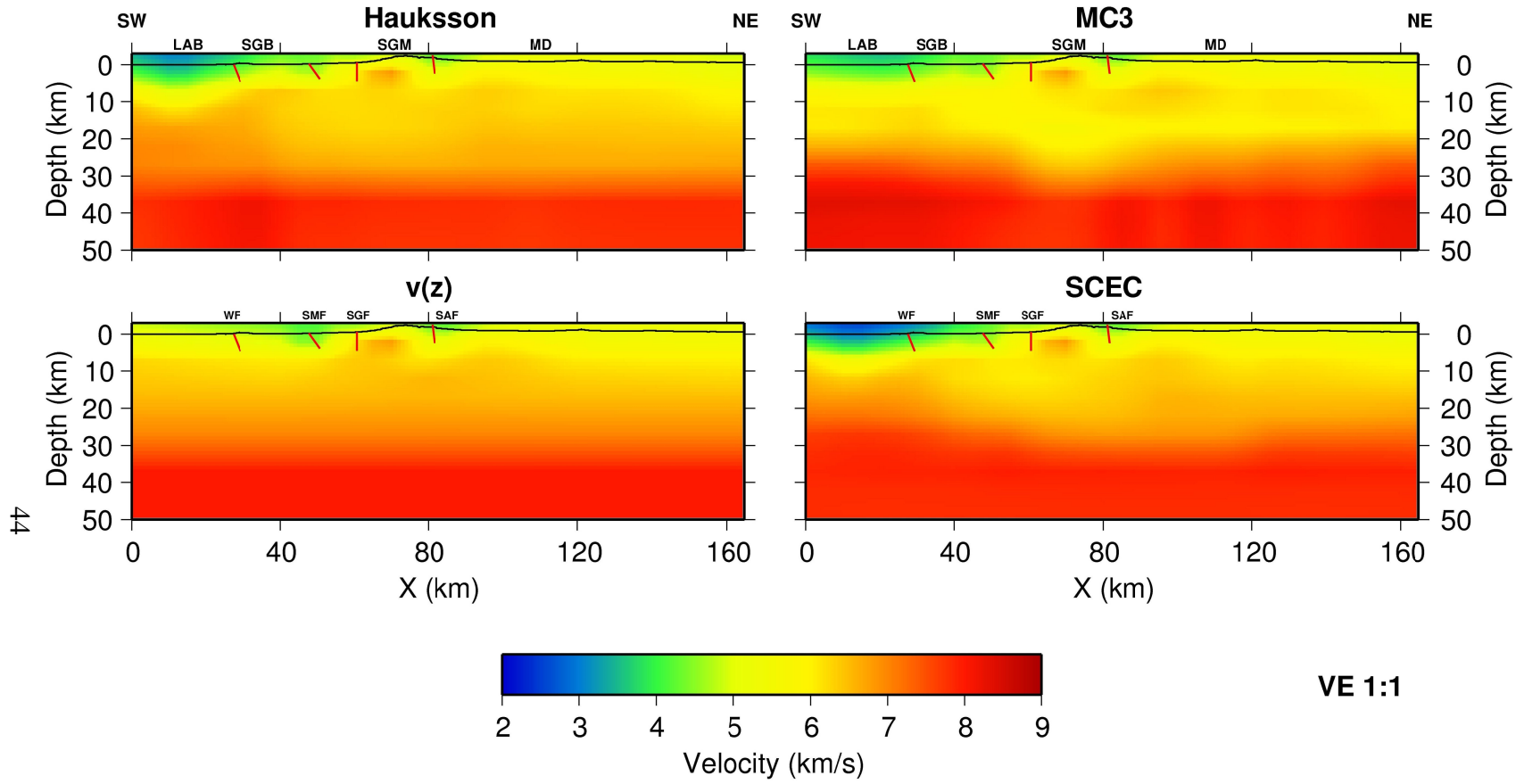


**Figure 14 - Velocity models for Line 1 after tomographic update. Black line shows topography along 2D line. Major faults are shown as red lines and labeled in lower two sections (WF- Whittier Fault, SMF – Sierra Madre Fault, SGF – San Gabriel Fault, SAF – San Andreas Fault). Major geographic areas are labeled in upper two sections (LAB – Los Angeles Basin, SGB – San Gabriel Basin, SGM – San Gabriel Mountains, MD – Mojave Desert).**

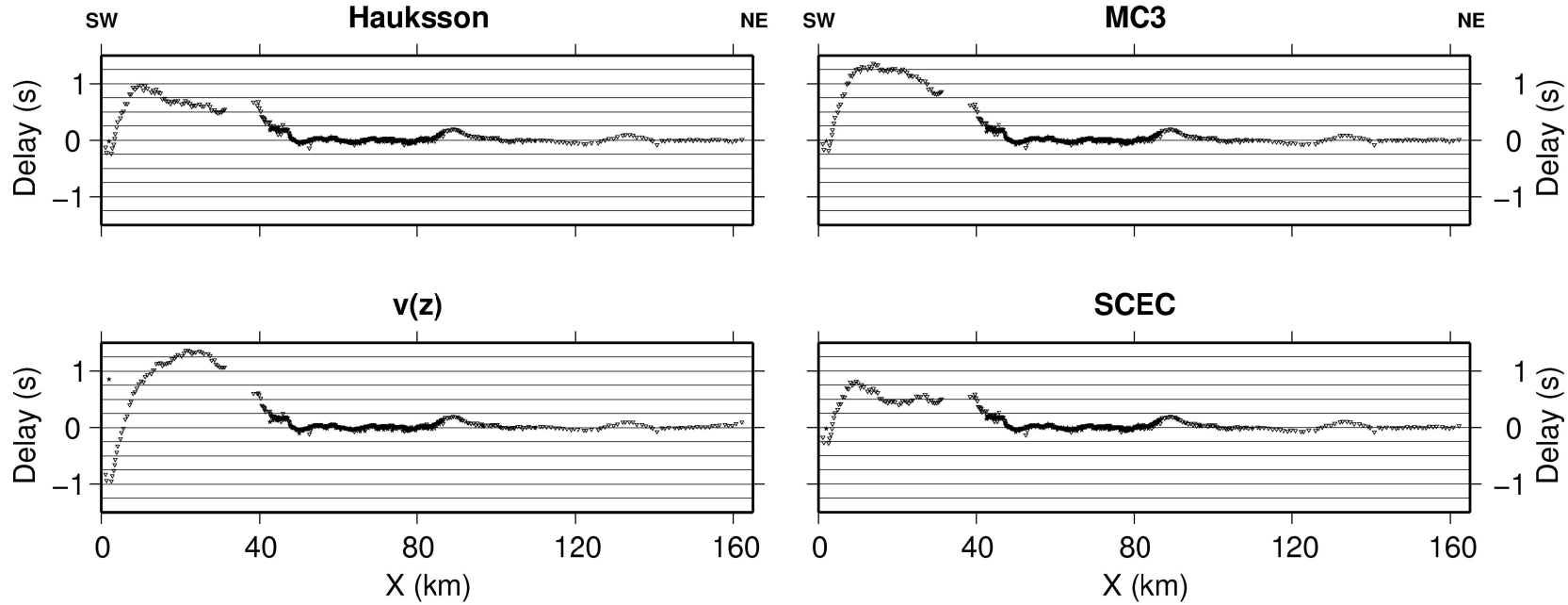


**Figure 15 - Residual shot (star) and receiver (triangle) delays computed for 4 models from Line 1. Positive delays between 0 and 40 km indicate true velocity slower than modeled velocity in Los Angeles Basin.**

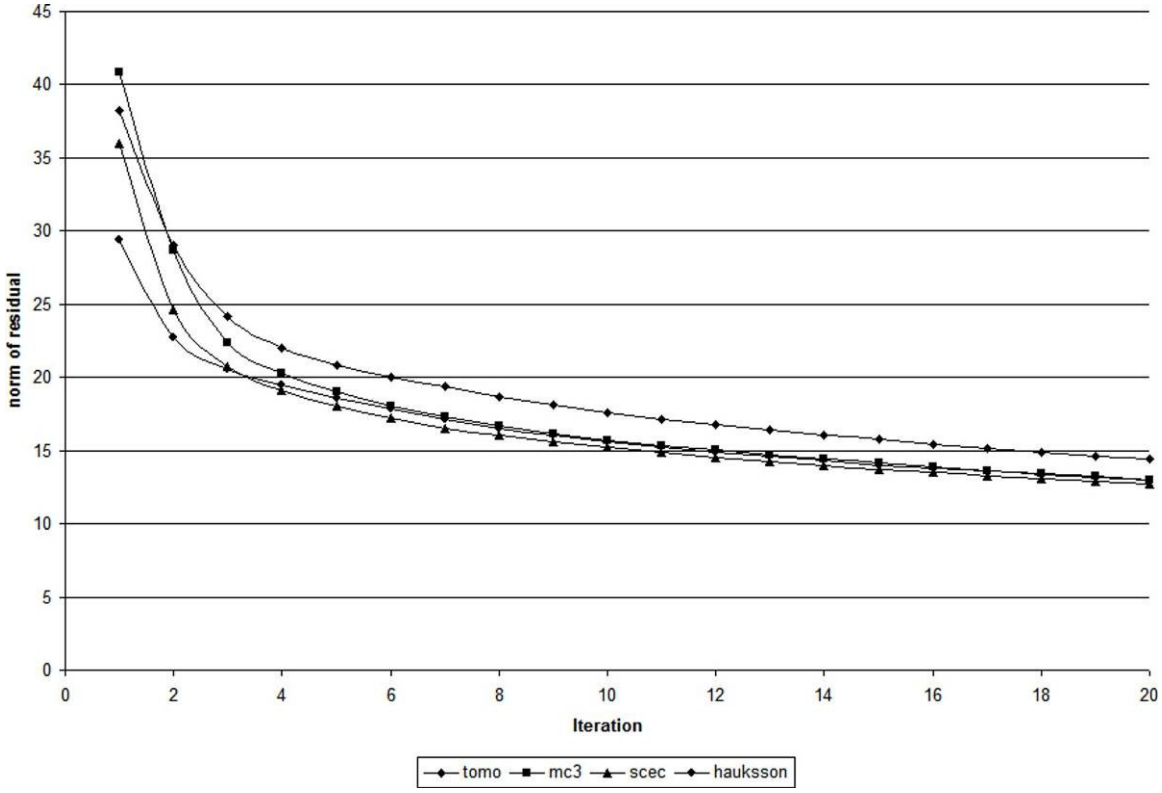


**Figure 16 – Norm of residual travel time error as a function of iteration for four Line 1 tomography runs.**

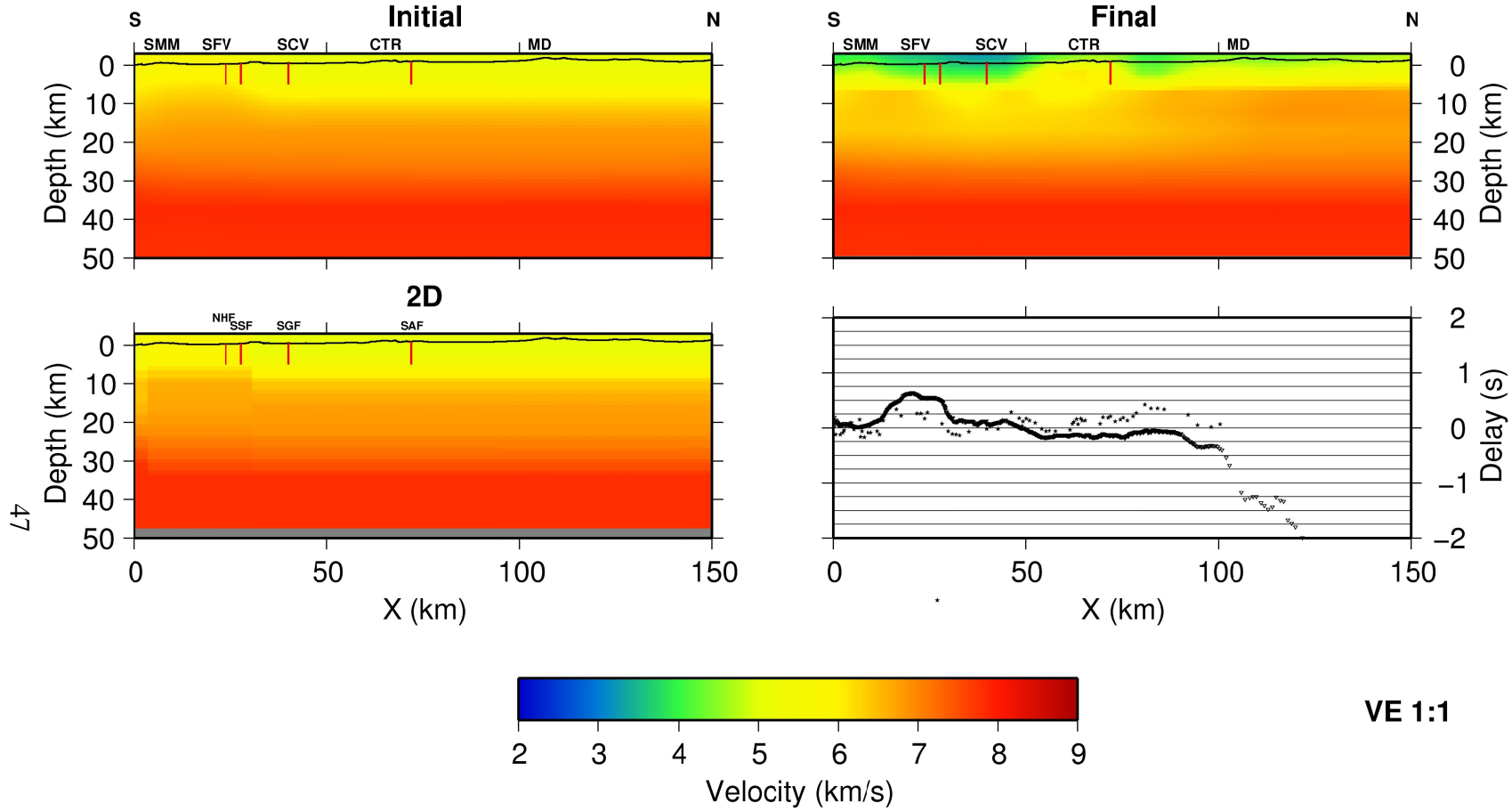


**Figure 17 - Velocity model for Line 2. Black line shows topography along 2D line. Major faults are shown as red lines and labeled in lower two sections (NHF- Nothridge Hills Fault, SSF – Santa Susana Fault, SGF – San Gabriel Fault, SAF – San Andreas Fault). Major geographic areas are labeled in upper two sections (SMM – Santa Monica Mountains, SFV – San Fernando Valley, SCV – Santa Clarita Valley, CTR – Central Transverse Range, MD – Mojave Desert). Shot delays shown as stars, receiver delays shown as triangles**

# Chapter 3 - Seismic imaging

For this study, depth images of the reflection data from the two LARSE lines were produced using prestack wave equation migration. Two properties of the wave equation technique are critical to the success of this approach.

Wave equation migration involves independent downward continuation of the recorded wavefield and an assumed source wavefield. Reflection point imaging is achieved by cross correlation of the two wavefields at each image point. As the wavefields are downward continued, primary reflection energy remains coherent and in phase with the source wavefield. Noise, such as surface waves, tend to become incoherent and do not, in general, correlate with the source wavefield. This phase discrimination turns out to be a very effective tool for detecting weak signal in the presence of strong noise.

Wave equation migrations are usually implemented using a parabolic, or one-way, approximation to the wave equation. This allows the algorithm to be carried out in the frequency domain, where each frequency component is imaged independently. By capturing these imaged components, they can be recombined after migration to form images corresponding to various input bandwidths. The ability to interrogate the imaged volume as a function of frequency after imaging and wavefield correlation is another key tool for detecting signals.

## *Data preprocessing*

Prior to releasing the data, preliminary preprocessing was applied by the LARSE group. This consisted of assigning geometry information to the trace headers, correcting timing and polarity errors, and resampling the data to 4 ms.

Initial work in developing a preprocessing stream focused on signal enhancement. A wide variety of techniques were tested in an attempt to boost the signal-to-noise ratio; these included array forming, spectral equalization, coherence filtering, and velocity filtering. However, none of these was able to improve on the images produced by the wave equation migration. The final preprocessing sequence was limited to the steps necessary to prepare the data for wave equation migration. The preprocessing steps applied to both data sets consist of:

1. 2D geometry assignment,
2. Bandpass filtering,
3. Resample to 24 ms,
4. Limit trace length to 24 s,
5. Median AGC,
6. Trace amplitude clipping,
7. Spiking deconvolution,
8. Static shift.

A 2D geometry was constructed for each line by fitting a straight line through the shot-receiver midpoints, and projecting the shot and receiver coordinates onto the line. The original surveyed elevations for shots and stations were retained. The maximum distance of projection from actual location to 2D location was about 2.5 km for each line. The impact of the projection from true locations to 2D locations will be discussed later in this section.

A band-pass filter (0.2-10 Hz) was applied to remove some very low frequency noise (<0.1 Hz) present on many traces, and to anti-alias filter the data for resampling. The traces were then resampled to 24 ms and limited to 24 seconds in length, to reduce the data volume for migration.

The raw data had significant numbers of spikes, as well as huge variations in the amplitudes from receiver station to receiver station. The combination of median gate AGC and trace amplitude clipping proved to be the most effect method to handle both problems. Both operations were applied on a trace by trace basis. Each trace sample was normalized by the median absolute value of samples within a one second time window; trace amplitude values were then clipped at the $95^{th}$ percentile.

Single trace spiking deconvolution was applied to whiten the spectra of each trace. Since the bandwidth of the image can be manipulated after migration, whitening of the input

spectrum was not as critical as improving the consistency of each frequency component across each shot record.

Prior to each migration, the surface consistent delays corresponding to the migration velocity model were removed from the trace data.

## *Shot-profile wave equation imaging algorithm*

The wave equation imaging code used here is based on the Seismix Un*x (SU) module *migprefd*, a 2D frequency domain finite difference prestack downward continuation migration (Cohen and Stockwell, 2005). The code is based on the parabolic wave equation and uses an implicit solution for the diffraction term. Three major modifications were made to the SU code for use in this study.

The first was to rearrange the order of computations so that the loop over frequency was the outermost loop. This allows individual frequency components to be depth imaged and output separately. By doing this, subsets of the frequency image planes can be weighted and stacked after migration to produce images of different bandwidths. The advantage of this approach is that it allows one to readily explore the imaged section as a function of bandwidth to determine where signal exists. In very low signal data sets such as this, determining bandwidth after imaging is critical, since signal is difficult, if not impossible, to find before imaging.

The second major modification to the SU code was to incorporate a mechanism to handle migration from topography. The mechanism involved modifying the logic handling the downward continuation so that source and receiver wavefields are not added to the extrapolated wavefield until the downward continuation has passed their elevation. This mechanism is similar to the zero-velocity layer technique of Beasley and Lynn (1992).

Prior to downward continuation, cells in the gridded migration velocity above topography are set to zero and each trace is static shifted so that each source and receiver is moved to the top of the nearest non-zero velocity. For each depth in the downward continuation loop, the velocity model is scanned horizontally to find segments of contiguous non-zero velocity. The wavefields over each of these segments are downward continued independently. As downward continuation progresses through the topography, these segments expand and merge, and additional wavefields are added. Once the lowest elevation has been passed, downward continuation proceeds as a single wavefield segment.

The third modification was to add filtering for evanescent waves. After each downward continuation step, both the source and receiver wavefields are transformed into in the lateral wave number (ω-Kx) domain. Wave numbers above the evanescent limit are zeroed, and the wavefields are transformed back to the ω-x domain.

## *Composite stacking*

For each shot, the shot profile migration produced a set of image traces at each image location. Each set contains the depth imaged frequency components for that location which can be weighted and recombined to produce images a various bandwidths.

Before stacking, each imaged frequency component was normalized then re-weighted to produce the desired image bandwidth. The normalization scaled each imaged frequency component for each shot to a constant value to account for residual shot-to-shot variations in the source spectrum.

The weighting scheme used here is based on a first derivative Gaussian function and shown in Equation 7:

$$A(f) = \frac{f}{f_C} e^{-\left(\frac{f-f_C}{f_C/2}\right)^2}, \tag{7}$$

where $f$ is frequency and $f_C$ is the center frequency of the weighting function. The choice of a weighting scheme is somewhat arbitrary; this particular weighting function was chosen to limit the effect of side lobes in the composite wavelet. The weighting function is shown for three center frequencies in Figure 18.

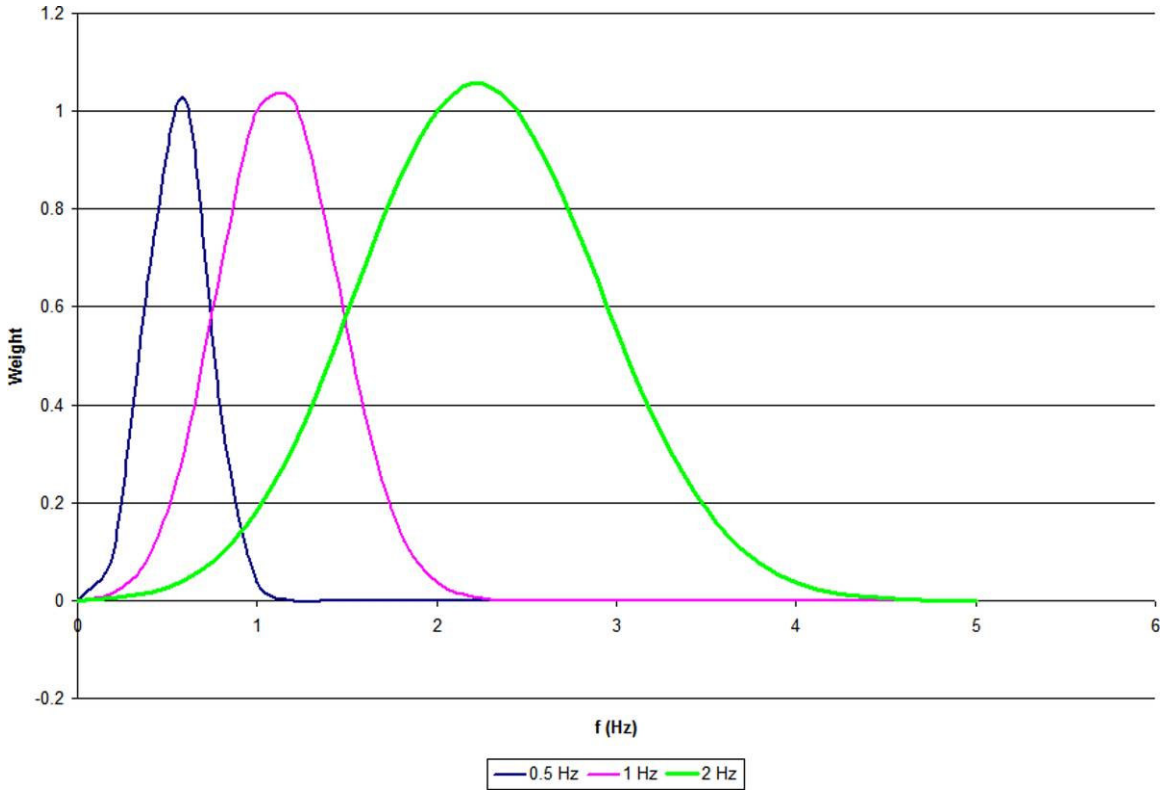


**Figure 18 – First derivative Gaussian spectral weighting functions for three center frequencies: 0.5 Hz, 1 Hz and 2 Hz.**

## *Wave equation imaging parameters*

A 100 m x 100 m grid was selected for both the input velocity grid and output imaging grids to correspond with the receiver spacing in the dense portions of each line. The slowest velocities in the migration models are roughly 4 km/s, which give an aliasing frequency for the output grid of 20 Hz; the frequencies of interest here are generally below 5 Hz.

The finite difference code offers several options for a maximum dip angle to be imaged. The deep structures of interest are expected to have shallow dip; however, near surface fault zones are likely to be more steeply dipping. The maximum migration angle was selected to be 79 degrees. Increasing or reducing the maximum angle did not show any significant changes in the image.

Figure 19 shows an impulse calculated using the parameter set selected for the migrations. The input was a single trace with spikes every 1 second, and was migrated in a 6 km/s constant background velocity. The output is a composite stack with a center frequency of 2 Hz. The impulse response is clean and free from dispersion artifacts, indicating a reasonable parameter set.

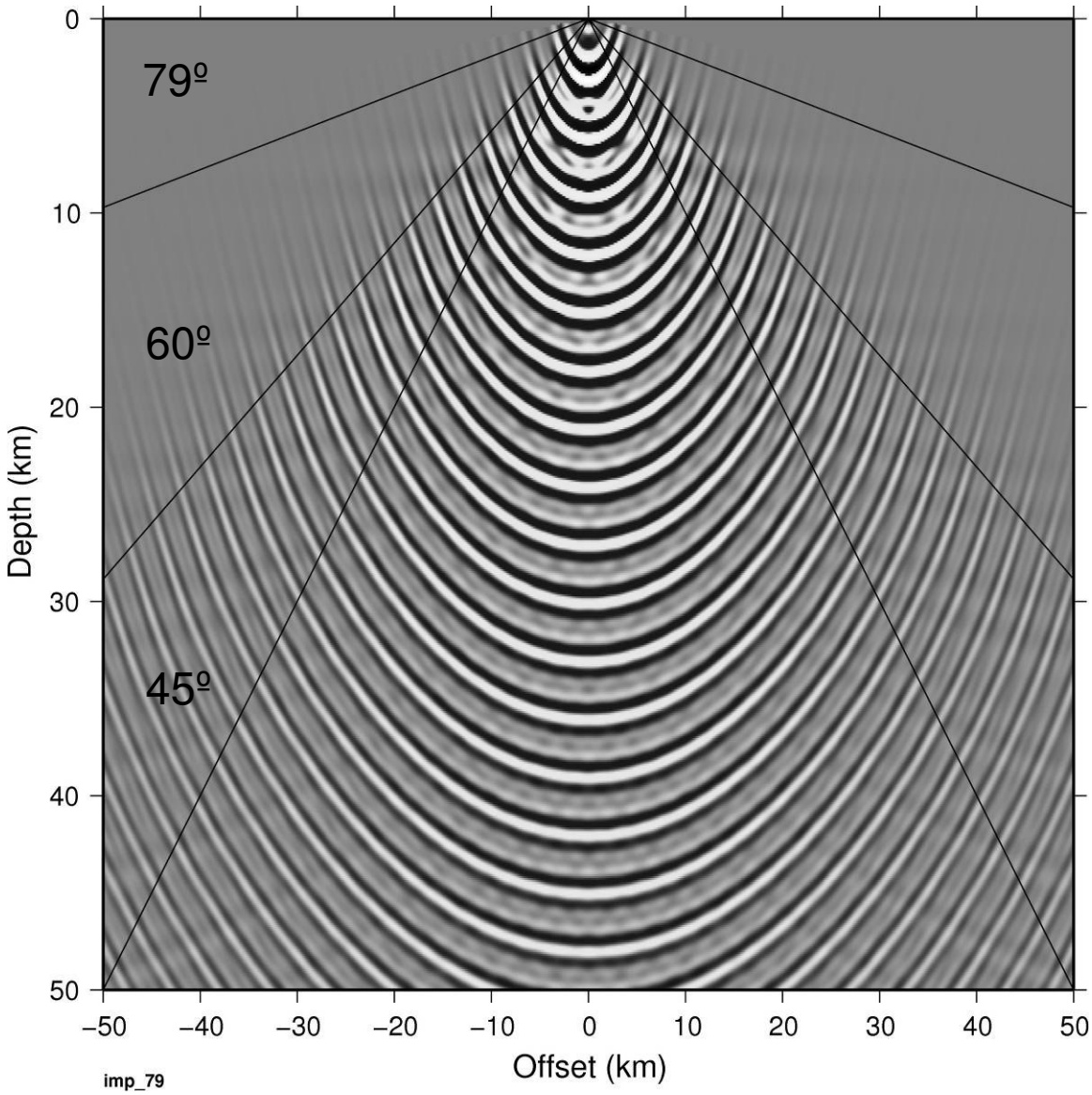


**Figure 19 – 2 Hz composite stack of impulse response from shot profile migration. Impulse response computed with spike at 1 second intervals, a 6 km/s constant back ground velocity, and a maximum dip of 79º.**

## *Synthetic results*

### Impact of acquisition geometry

To verify the code and to assess the impact of the acquisition geometry on imaging, synthetic data sets were constructed to simulate the acquisition along Line 1, and migrated with the selected parameters.

The first model data set used straight ray travel times through a constant 6 km/s background model, and the locations of the sources and receivers as projected onto the 2D line (not the true locations). Flat reflectors were located every 5 km in depth. The 2 Hz composite image of this model is shown in Figure 20. The images of the reflectors show the highest amplitudes in the center of the section and some minor distortions of the imaged depths at depths of 0 and 5km beneath the San Gabriel Mountains. However, the reflectors are largely well imaged without significant migration noise. For low frequency images, the sparse acquisition geometry does not appear to have a significant impact on quality.

The second test was conducted to test the sensitivity of the image to the 2D projection. A second model data set was constructed in the same fashion except that the true 3D locations were used to compute travel times. The synthetic gathers were then projected into their 2D positions and migrated. The 2 Hz composite image for this test is shown in Figure 21. The reflector at 0 km depth is somewhat lower amplitude and imaged at a

slightly deeper depth. Likewise, the reflector a 5km depth is imaged slightly deeper than expected. However, the magnitude of the depth errors is small, and the migrated images of the 2D and 3D models below 5 km are virtually identical.

The synthetic tests indicate that for low dip reflectors at low frequencies, imaging artifacts are more likely due to the non-uniform acquisition geometry than the effect of the 2D projection.

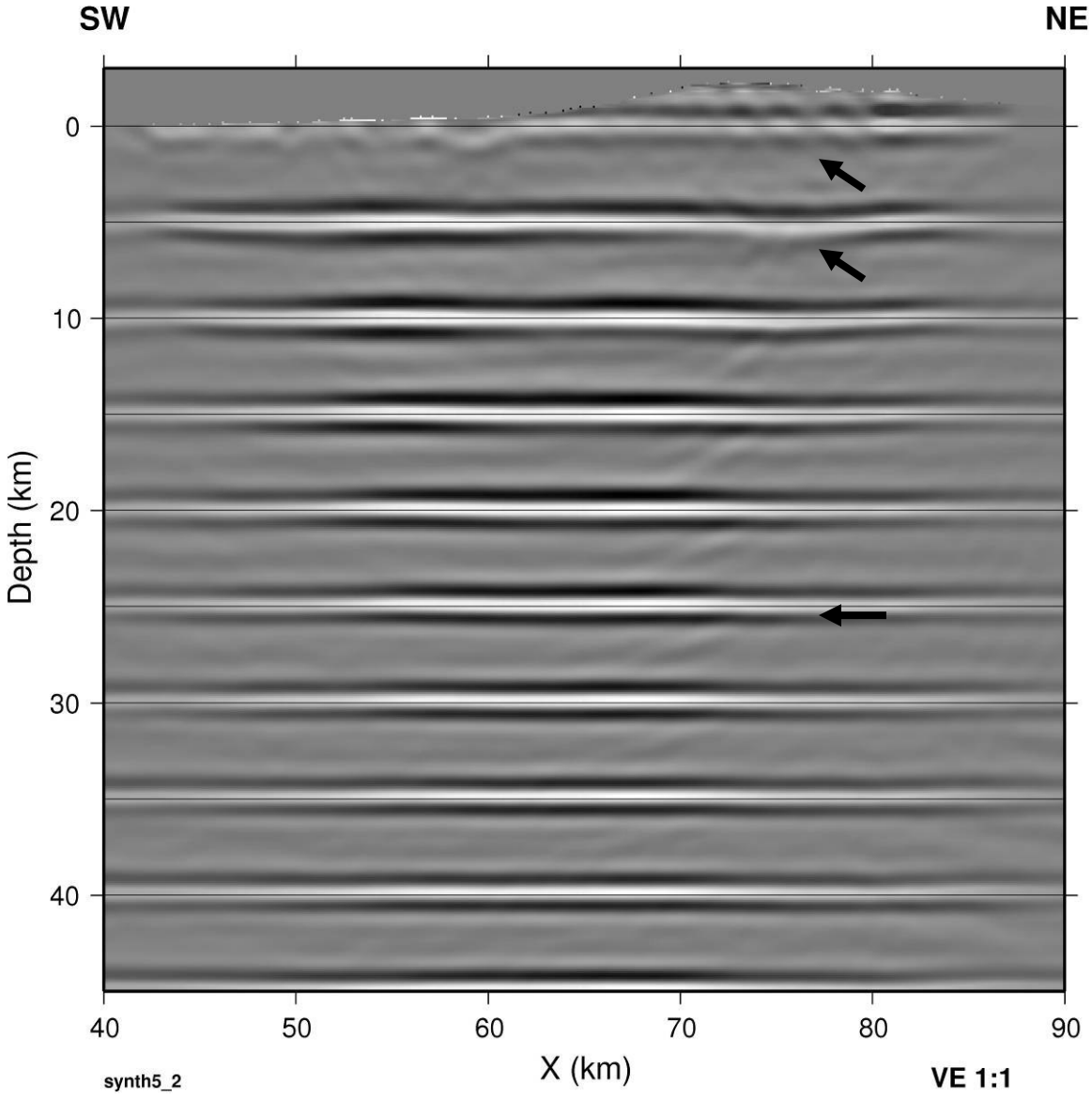


**Figure 20 – 2Hz composite migration of ray-traced 2D synthetic using Line 1 geometry as projected into 2D locations. Model assumed flat reflectors at 5km intervals and a constant 6 km/s back ground velocity. Arrows indicate areas of image distortion due to acquisition geometry.**

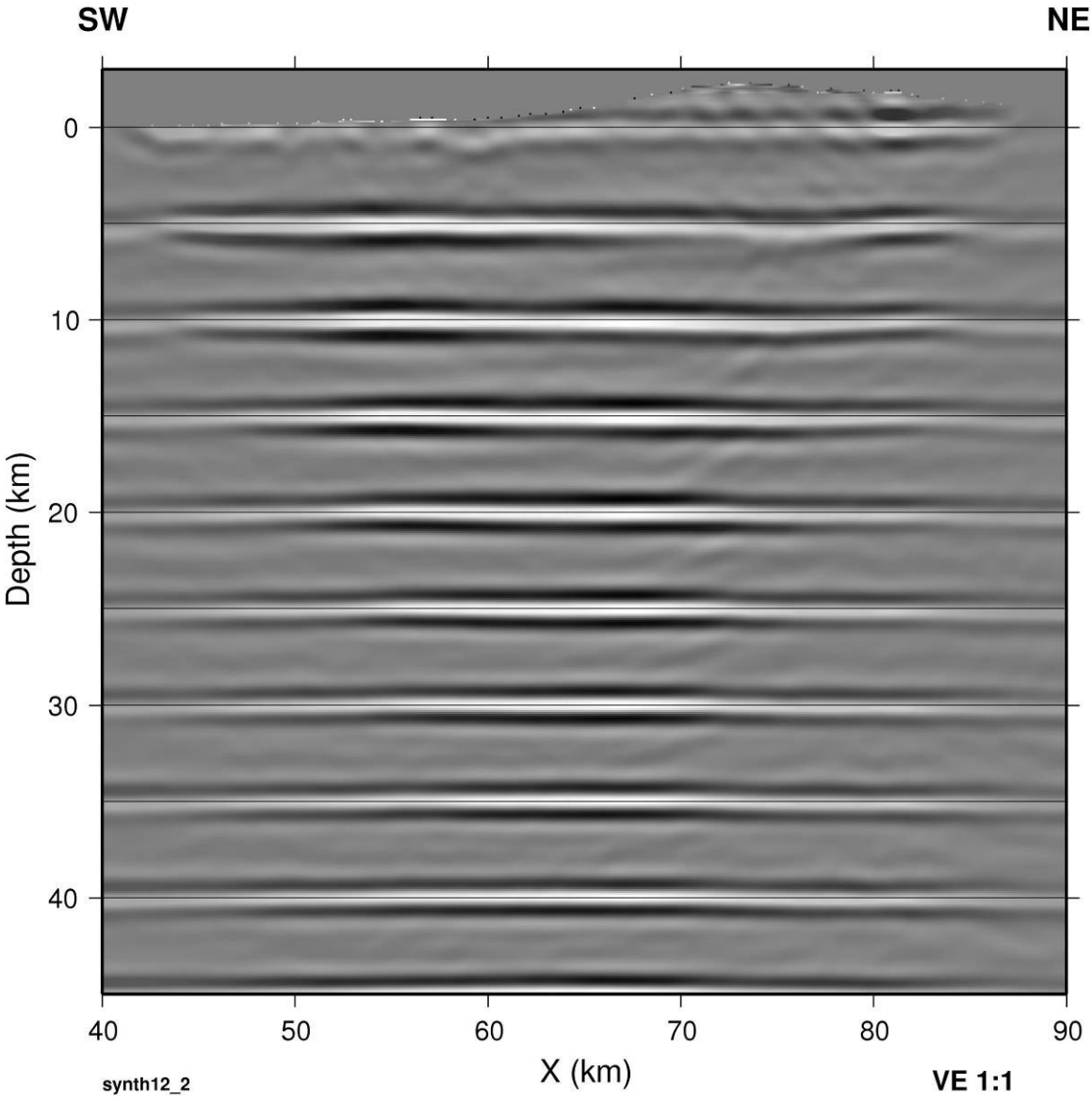


**Figure 21 - 2Hz composite migration of ray-traced 3D synthetic using Line 1 geometry from true 3D locations. 3D synthetic data was migrated from 2D locations. Model assumed flat reflectors at 5km intervals and a constant 6 km/s back ground velocity. No additional significant image distortion caused by 2D projection.**

## Impact of sensors and recording instruments

Given the mix of instruments and geophones used in recording this survey, differences in phase and amplitude response of individual stations could affect the quality of the final image. In particular, both the recording instruments and geophones introduce significant phase shifts to the low end of the spectrum. Figure 22 shows the nominal phase and amplitude responses for the types of geophones used in these surveys. At 2 Hz there is a phase difference of 70º between a 2 Hz geophone and an 8 Hz geophone. Generally, phase shifts of this magnitude are significant. The concern was that migrating wavefield components with these phase distortions uncorrected would degrade the migrated image. However, synthetic tests and tests with the field data indicate that this was not the case.

Figure 23 shows the composite migrated image of the ray-traced synthetic with geophone and estimated recording instrument phase shifts applied. In this synthetic, the distribution of geophone and recording instrument types is identical to that in the survey. This image appears nearly identical to the image in Figure 20; there are, however, subtle differences. The peaks of the reflections above 30 km are slightly deeper than the 5 km intervals in the center of the section, and a gradual sag in the reflector depths towards the edge of the section.

Figure 24 shows the difference in instantaneous phase between the sections shown in Figure 20 and Figure 23. The phase difference at the reflectors (the 5 km depth intervals)

is largely a constant -30º in the center of the section, and decreases towards -60º at the edges, with the zone of transition becoming wider with depth.

Recall that the central portion of this line (40-90 km) was occupied by a more or less uniform mix of 2 Hz, 4.5 Hz and 8Hz recorders; the rest of the line was occupied primarily by 2 Hz recorders. What appears to be happening here is that the downward continuation process and the distribution of instruments have averaged out the phase errors, leaving a nearly constant residual phase error in the center of the section. Although laterally varying phase errors are introduced, creating small differences, the magnitude of these errors is small. Concerns about the degradation of the image turned out to be unfounded; there is no real indication that the mixture of phase errors contaminates the image enough to impede interpretation.

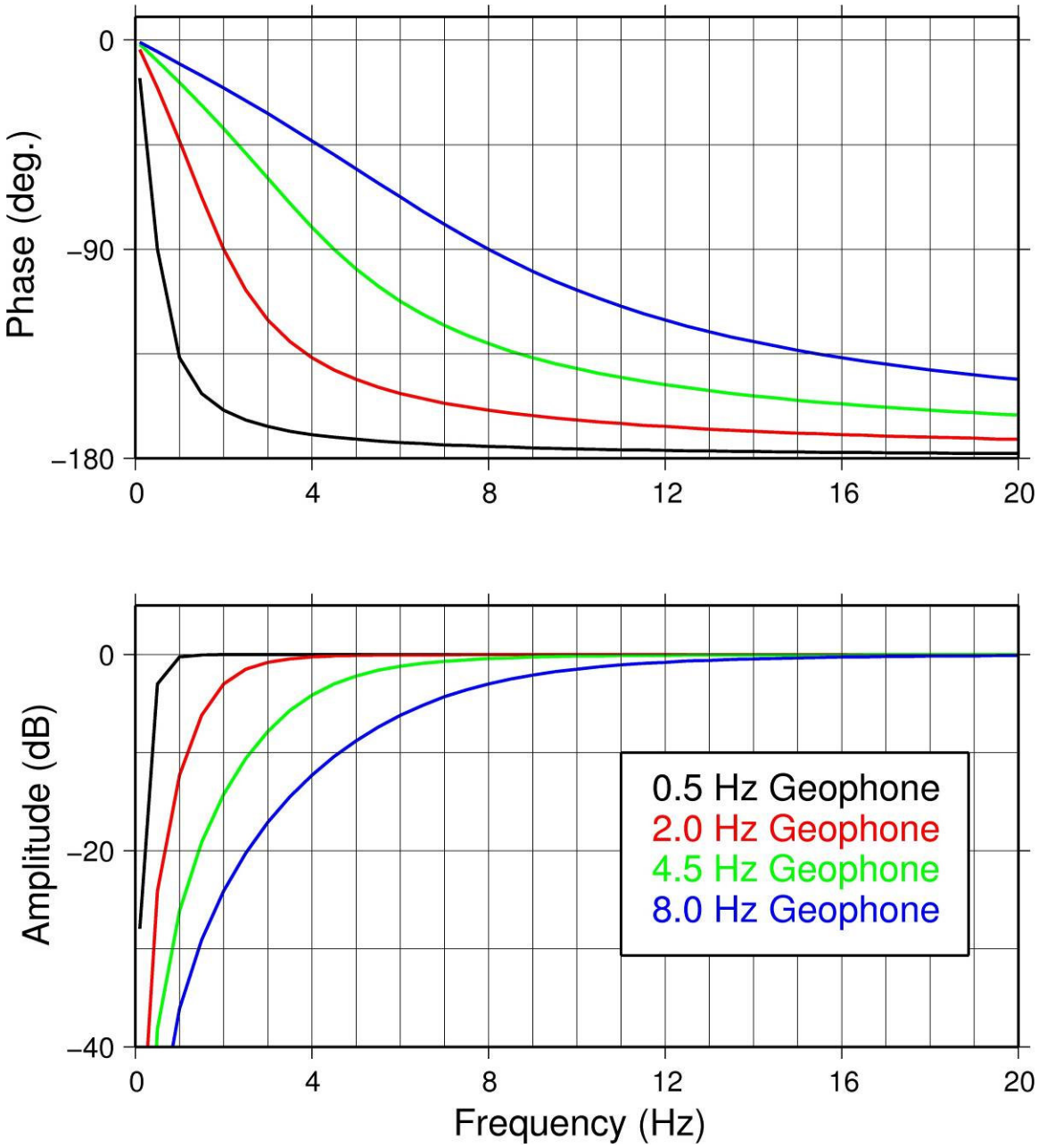


**Figure 22 - Nominal geophone phase and amplitude response for instruments used in the LARSE surveys.**

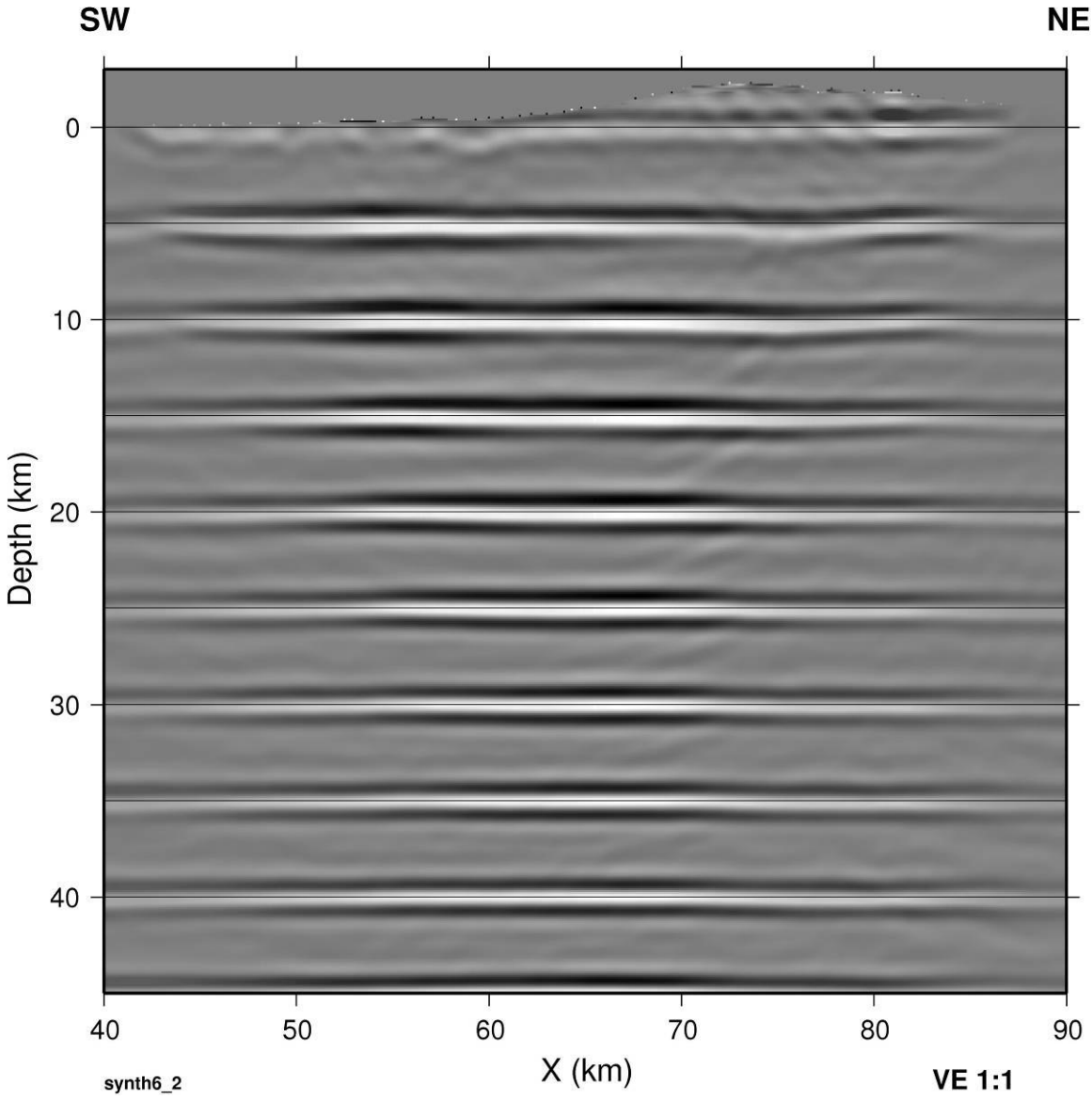


**Figure 23 - 2 Hz composite migration of 2D synthetic with geophone and recording system phase shifts applied. Small phase distortions in the image are introduced by instrument responsess, but overall image quality is preserved.**

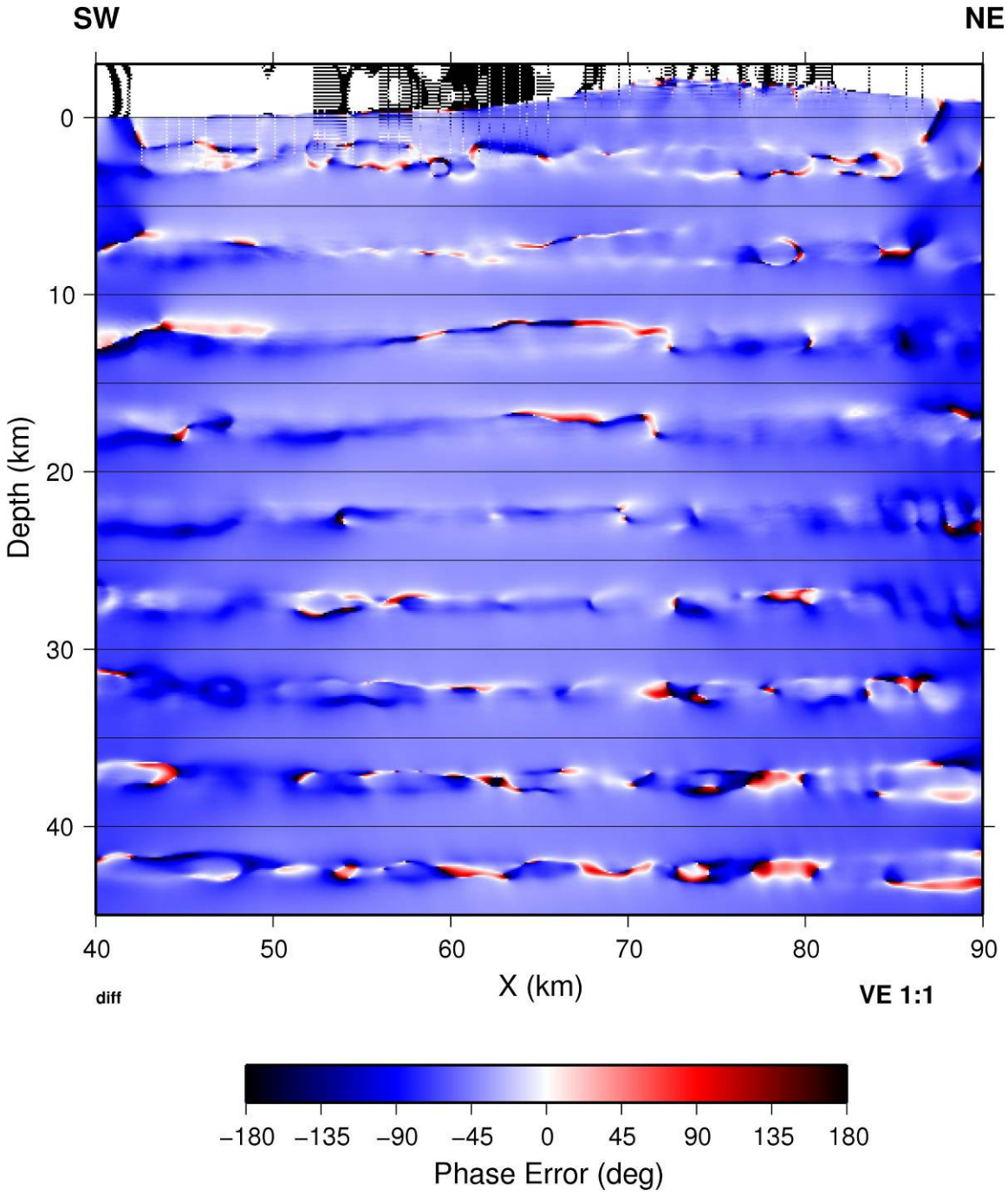


**Figure 24 - Phase error introduced by geophones and recording instruments. Difference in instantaneous phase between 2 Hz composite migrations of synthetics with and without instrument phase responses applied. Phase errors at the reflectors (5km intervals) vary from -30º in the center of the line to -60º on the edges.**

# Chapter 4 - Imaging results and discussion

Wave equation prestack depth migration as described in Chapter 3 was applied to the reflection data from LARSE Lines 1 and 2 using the velocity models discussed in Chapter 2. The final composite migration stacks are shown in Figure 25 and Figure 26. These sections were stacked with a depth varying weighting function (described below) and have a mild post-stack dip filter applied.

The imaged sections are fairly noisy; this begs the question - are the features in the section real reflections or are they simply artifacts of migration of noisy data? As will be shown, correlations with known geology and other constraints can be found, indicating that many of the imaged features are in fact primary reflections.

Reflectors are imaged in both sections to depths of more than 30 km. The imaged reflectors are generally discontinuous; however, some packages can be traced for some distance. Reflections from the Mohorovicic discontinuity (Moho) are imaged in both sections. Both sections also show discontinuities in the Moho near the San Andreas Fault. Groups of bright reflector segments can be seen in both sections; these are most prevalent near the San Andreas and San Gabriel Faults. The migration from Line 2 also shows a sequence of shallow high frequency reflections associated with the San Fernando sedimentary basin, and a similar package just north of the San Andreas Fault.

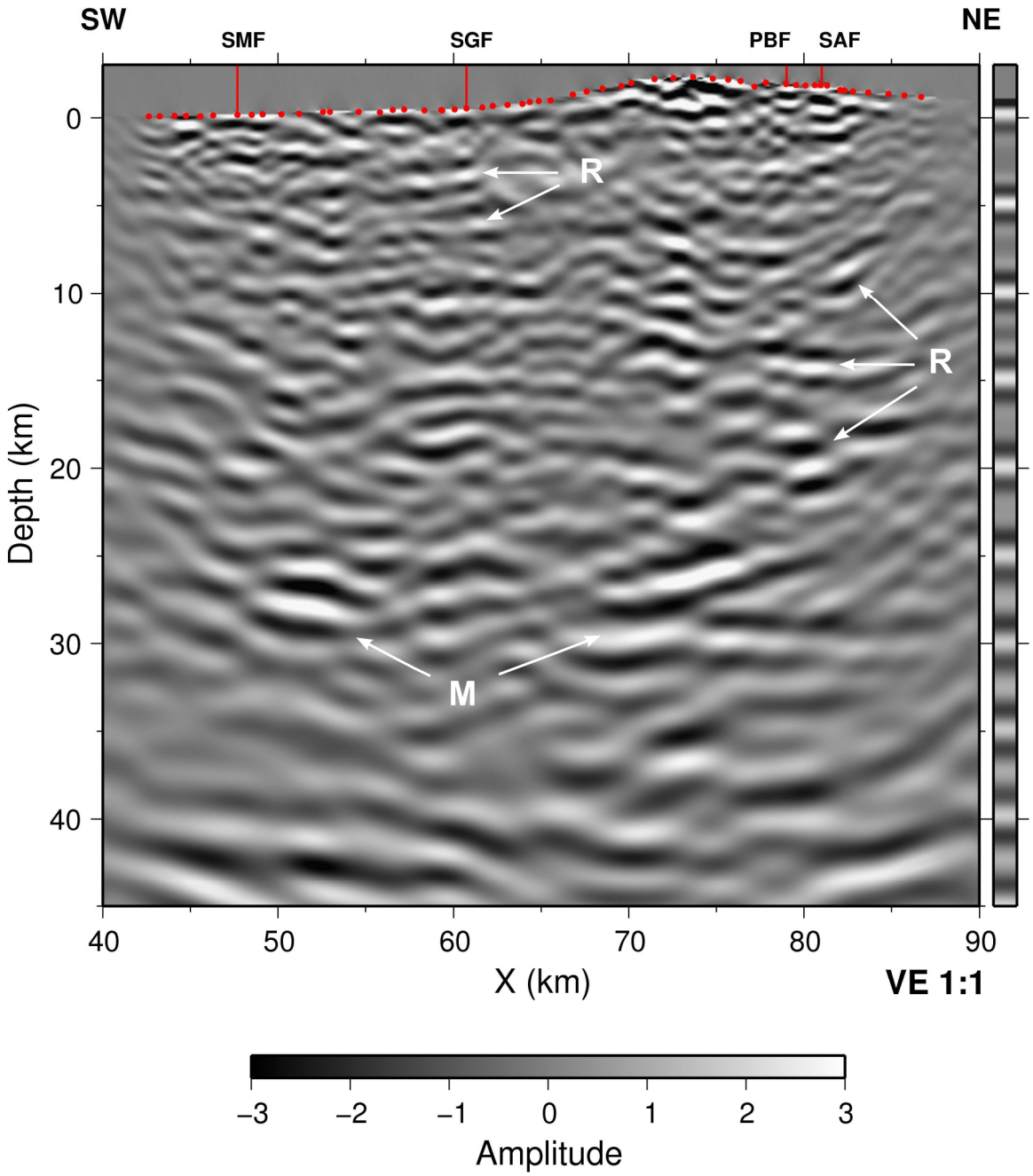


**Figure 25 - Composite PSDM stack for Line 1. Locations of reflector segments (R) and Moho reflections (M) annotated. To right of section is synthetic image composited with same depth varying weighting function. Major faults annotated on top of section: SMF – Sierra Madre Fault, SGF – San Gabriel Fault, PBF – Punchbowl Fault, SAF – San Andreas Fault. Locations of shot points shown as red circles.**

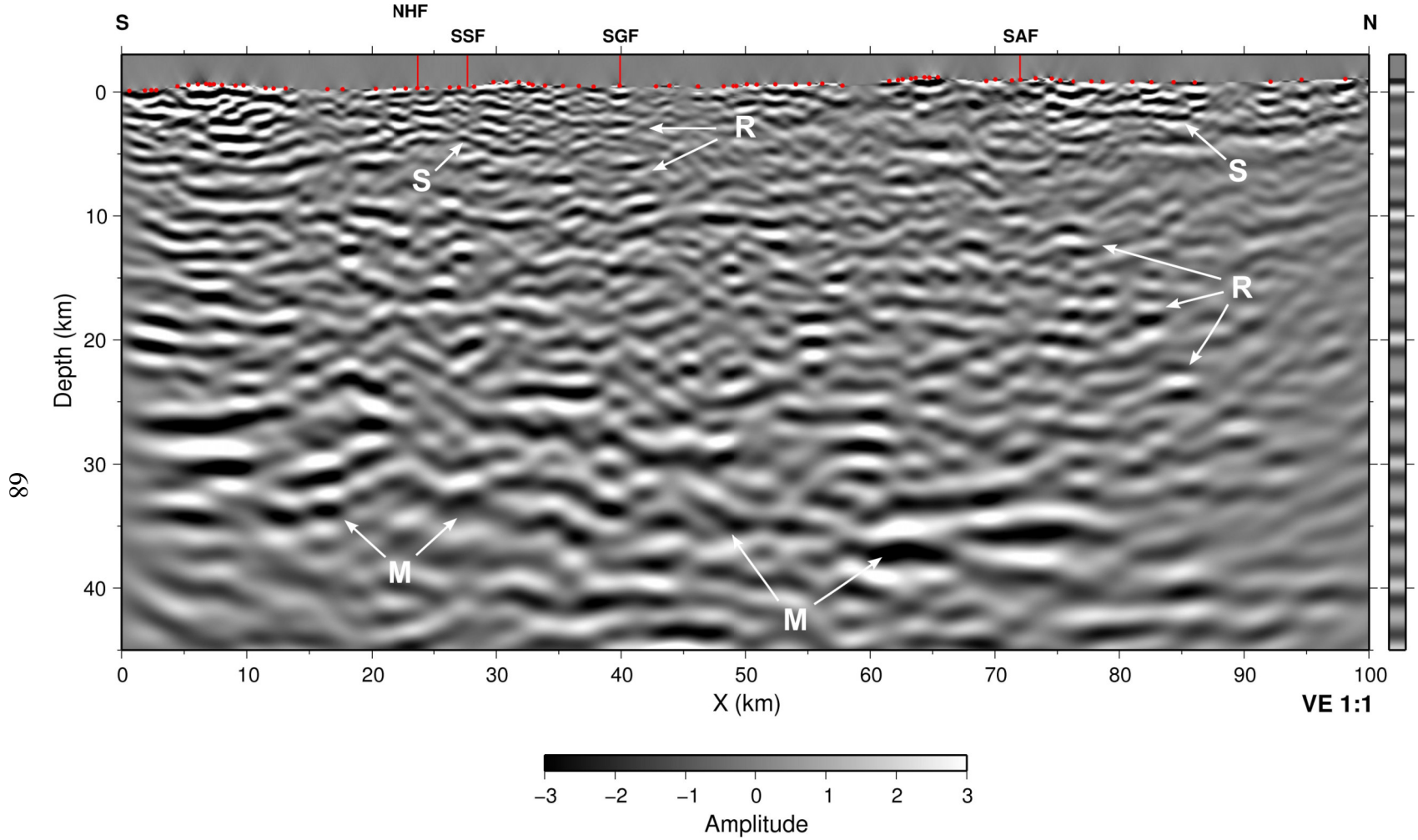


**Figure 26 - Composite PSDM stack from Line 2. Locations of sedimentary basins (S), reflector segments (R) and Moho reflections (M) annotated. To right of section is synthetic image composited with same depth varying weighting function. Major faults annotated on top of section: NHF - Northridge Hills Fault, SSF= Santa Suzana Fault, SGF – San Gabriel Fault, SAF – San Andreas Fault. Locations of shot points shown as red circles.**

### *Imaging bandwidth*

Investigations of the reflection data both before and after migration, lead to the selection of an optimal signal bandwidth in the 0.5-3.0 Hz range. This was determined primarily by assessing the depth image clarity and coherency as a function of frequency. In general, the best images of shallow features (0-15 km) were found in the 1.0-2.0 Hz range; reflectors at 30 km and deeper best imaged in the 0.7-1.0 Hz range. Composite images above 4.0 Hz became increasingly more chaotic and appeared to offer little information. A sampling of composite stacks from Line 1 for center frequencies from 0.5 to 5 Hz is shown in Figure 27.

The low end of the frequency spectrum provides the best images for several reasons. First low frequencies are less susceptible to scattering than higher frequencies; they are more likely to remain coherent throughout the long travel path. Additionally, low frequency components are less sensitive to imaging errors. Velocity errors and the assumption of a 2D geometry will result in errors in the imaged depth of reflections. If these depth errors are a significant fraction of a wavelength, the imaged reflections will not stack coherently. Lower frequency components have correspondingly longer wavelengths, and a given depth imaging error will affect lower frequency components to a lesser degree. Finally, in these particular data sets, surface waves and direct arrivals tend to dominate the 5-20 Hz portion of the spectrum.

For the final images, a depth varying set of weights were chosen to provide the best image throughout the section. The weighting function is summarized in Table 2. To assist in estimating the resolution of each composite stacks, synthetic data with reflectors every 5 km are stacked with the same depth variable bandwidth and shown to the right of each figure.

| Depth (km) | Center Frequency (Hz) |
|---|---|
| 0 | 2.0 |
| 10 | 1.6 |
| 20 | 1.3 |
| 30 | 1.15 |
| 40 | 1.05 |

**Table 2 – Parameters for depth varying weight function for final composite stacks.**

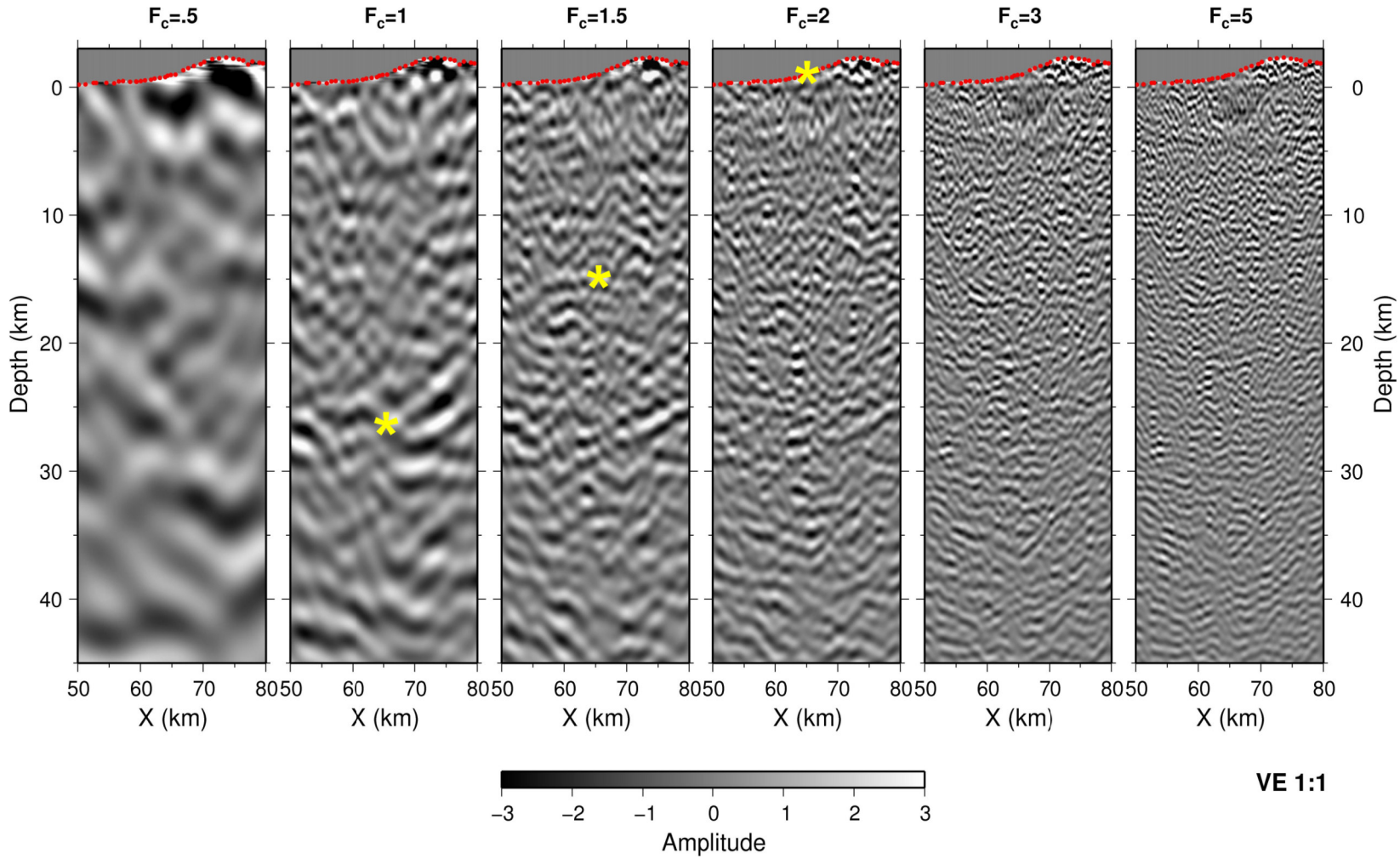


**Figure 27 - Comparison of various imaging bandwidths for Line 1. Center frequency for constant weighting function shown at top of panel. Approximate depth/center frequency pairs of weighting function shown in yellow.**

## *Comparison with Kirchhoff migration*

2D and 3D Kirchhoff migrations were run on the Line 1 data for comparison to the wave equation migration. Figure 28 shows a constant weighting function composite of the wave equation results along with stacks of 2D and 3D prestack Kirchhoff depth migrations. In the 3D migration, travel times were computed using the true 3D source and receiver locations and a 2.5D extension of the 2D velocity model. The input data to both Kirchhoff migrations were band-limited to the same 1.4 Hz spectrum used to composite the wave equation results. All three sections have the same 60º dip filter applied. Various reflectors interpreted from the 2D migration are shown posted on all three sections.

The only significant difference between the 2D and 3D Kirchhoff migrations is in the first 5 km of the section; below this the two methods produce nearly identical images. The difference in the shallow image is expected as the distance between 2D and 3D positions is a significant fraction of the travel path for the shallowest reflectors. However, neither method produces nearly as clean and continuous an image as the wave equation migration, shallow or deep. By comparing the superimposed interpretation, the strongest reflectors imaged by the Kirchhoff method can be seen to be parts of more continuous and better imaged packages of reflectors imaged by wave equation migration.

The improved signal to noise ratio of the wave equation migration is likely due to the imaging condition employed. Kirchhoff migration uses a kinematic imaging condition; it implicitly assumes that every sample on the input trace is primary reflection. Wave

equation migration employs a wave field correlation imaging condition; as the receiver wavefield is downward continued, only those parts of the wavefield in phase with downward continued source field are included in the image. This phase discrimination turns out to be an effective noise filter, allowing low power reflections to be imaged in the presence of strong noise.

The ability of wave equation migration to handle more complex wave fronts than the Kirchhoff algorithm is probably not a significant factor given the smooth velocity models used here.

The combination of the wavefield correlation and the ability to determine the image bandwidth after this correlation is the primary reason for the improvement in the images presented here.

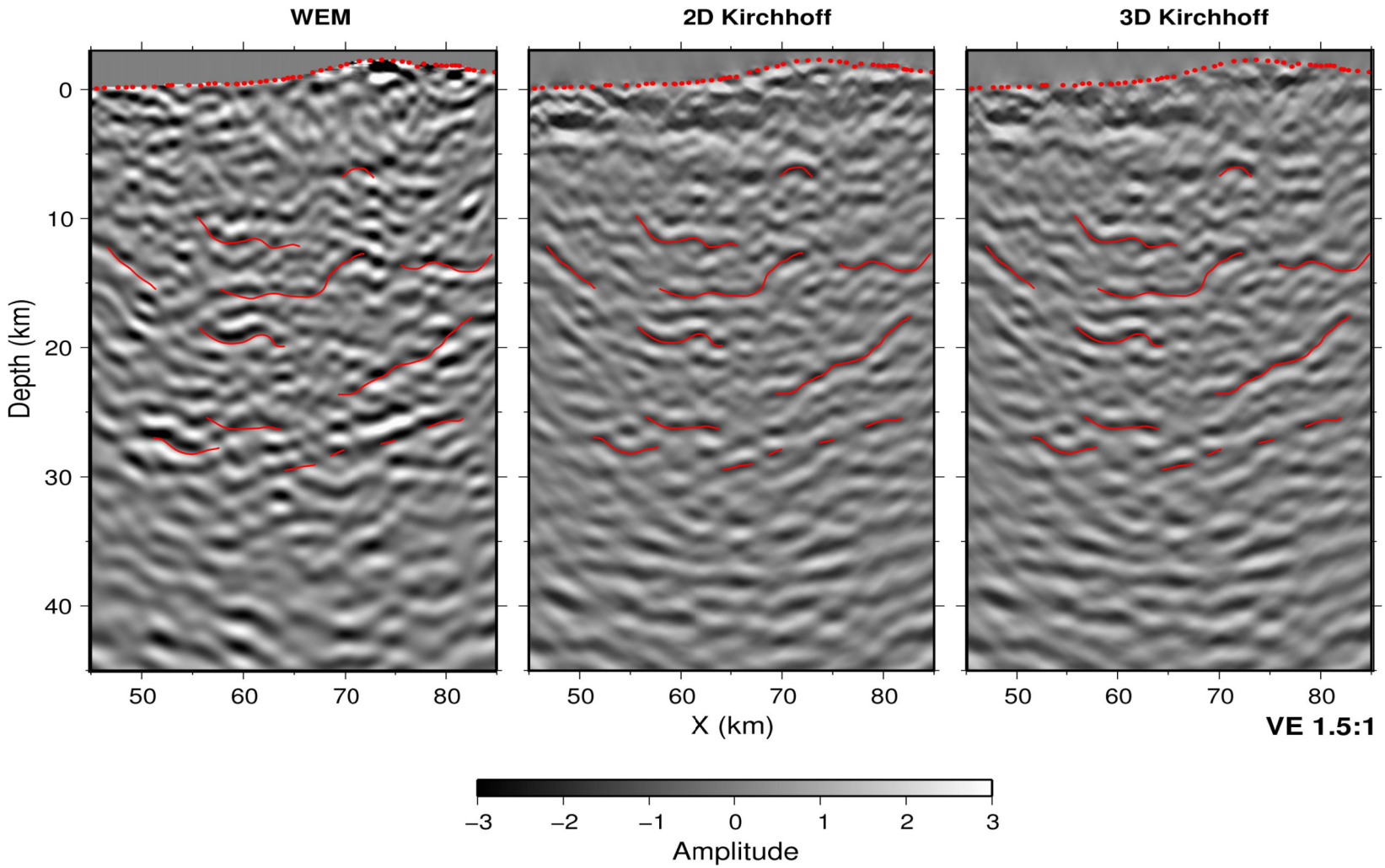


**Figure 28 - Comparison of prestack wave equation migration to 2D and 3D prestack Kirchhoff migration. All sections have 60° dip filter applied. Interpretation from 2D Kirchhoff posted on all sections. Wave equation migration shows improved reflector continuity and signal quality.**

## *Comparison of velocity models*

Four velocity models were constructed for Line 1 to test the effect of the various regional background models on the imaging. Composite stacks for the four migrations are shown in Figure 29. Various horizons interpreted from the Hauksson migration are shown on each section for comparison.

As noted in Chapter 2, the tomographic updates converged to largely the same model in all four cases. This is reflected in the images obtained here; the upper 20 km in each case are nearly identical. Below 20 km, the images from the Hauksson and SCEC models are nearly the same; there are very minor differences in the depth of reflectors, but the same events are present. The MC3 model is slightly slower than the Hauksson or SCEC modles; hence, it images the deeper reflectors 1-2 km shallower. The V(z) function places these same reflectors slightly deeper (~1 km) than the others. The overall image quality is largely unaffected by the differences in these models. The major difference between these models is in the imaged depths of the deeper reflectors.

Figure 30 shows a comparison of migrations using the Hauksson velocity model with and without the tomographic update. There are significant differences in these two images throughout the section, despite the velocity difference being restricted to the first 10 km. The model with the tomographic update does seem to produce better reflector continuity, although it is difficult to argue for one over the other in terms of image quality alone. However, the near surface velocity model has a significant impact on the entire image; as

the updated models are more consistent with the measured travel times through the near surface, I would argue that the tomographically updated models produce a more accurate image.

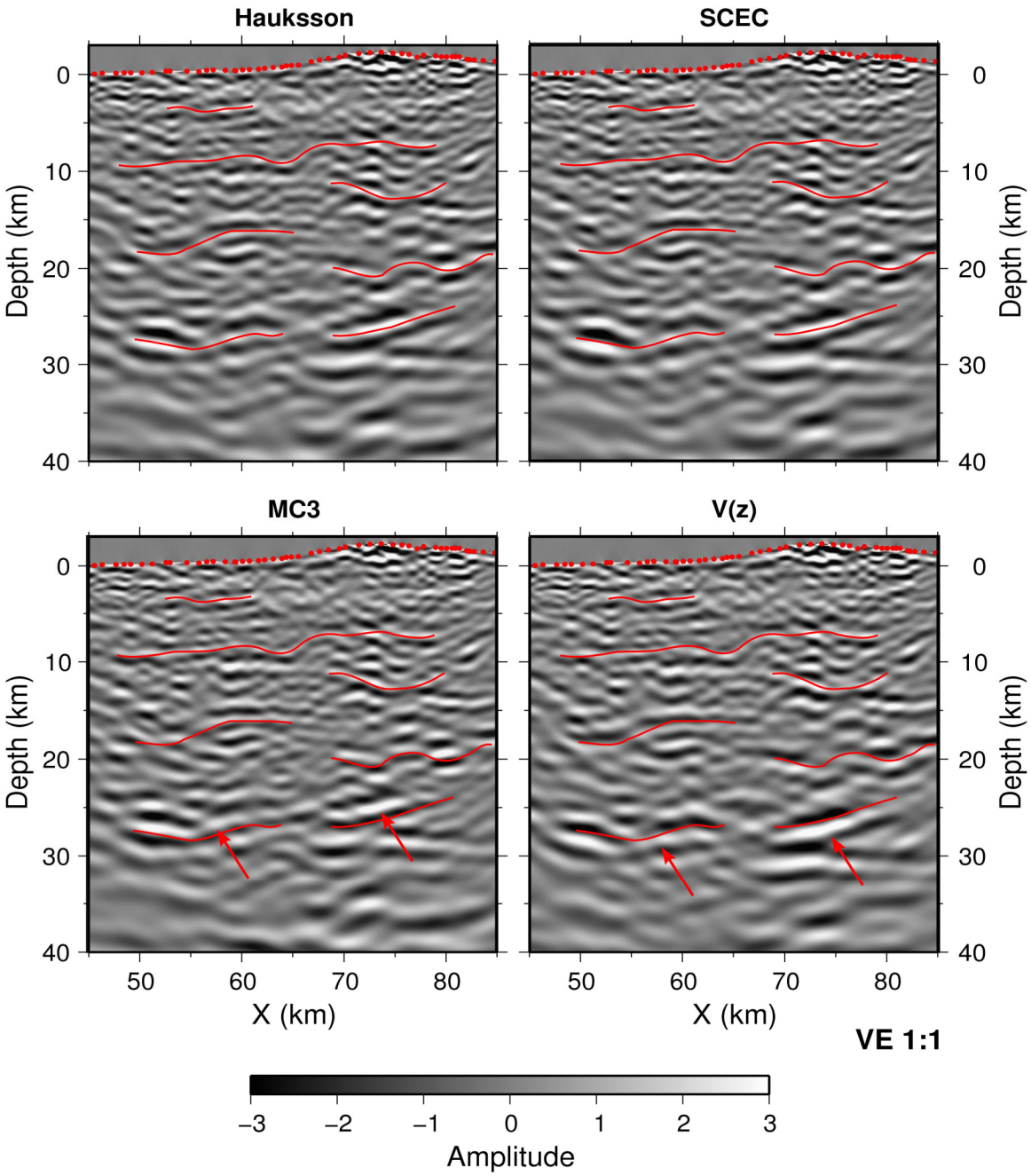


**Figure 29 - Comparison of Line 1 depth migrations using four different velocity models. Interpreted reflectors from Hauksson model posted on all sections in red. Arrows show areas where deep events are imaged a slightly different depths.**

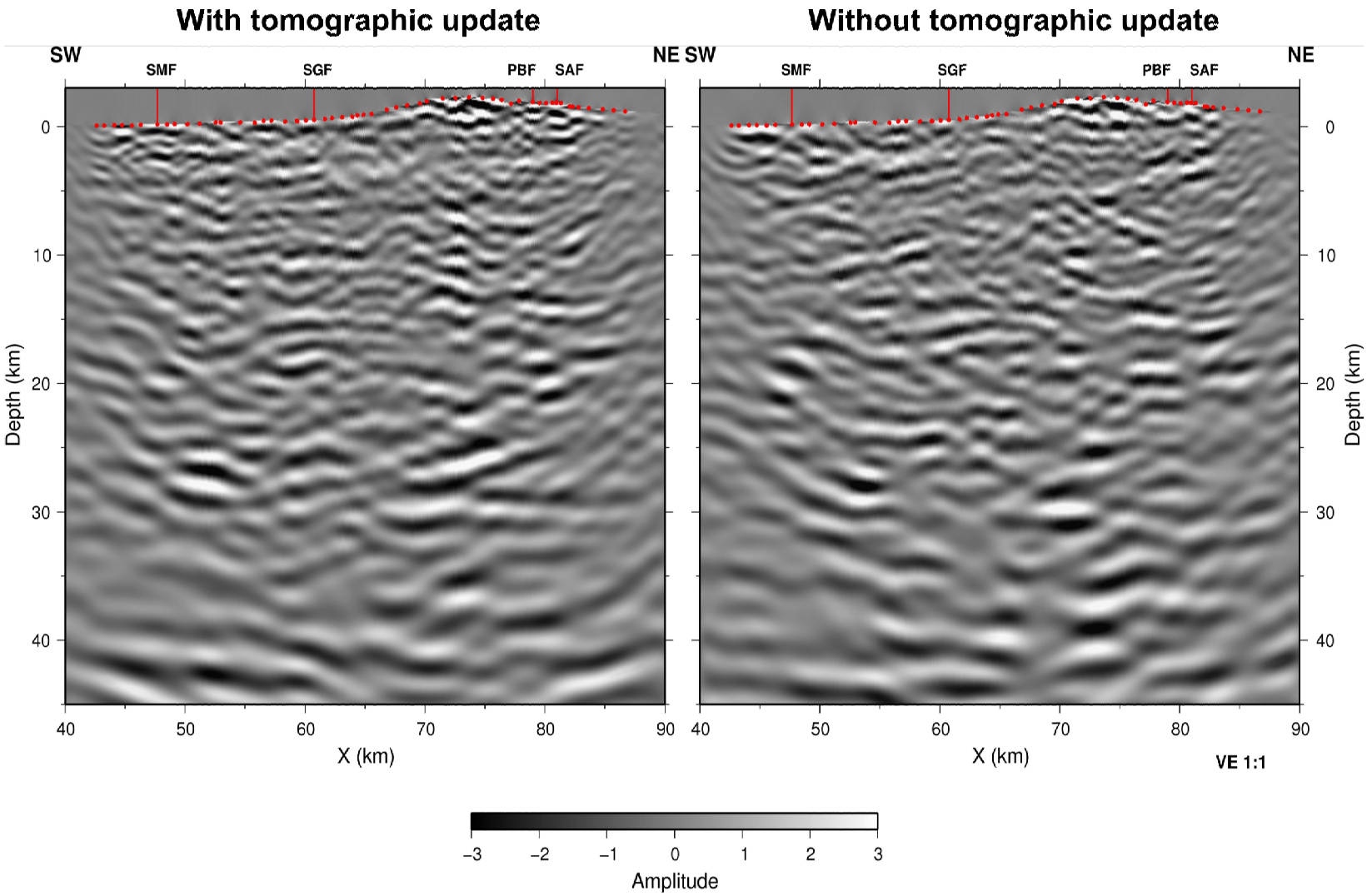


**Figure 30 - Comparison of Line 1 migrations using velocity models with and without tomographic update. Migration with tomographic update shows improved reflector continuity.**

## *Comparison to receiver function imaging*

To assess the validity of the images presented here, these results were compared to the results from two recent studies of crustal structure in southern California. Both used receiver function techniques and teleseismic data to estimate crustal thickness and structure in the LARSE area.

The first, a regional study by Zhu and Kanamori (2000) produced estimates of crustal thickness at 84 broadband stations in southern California. The locations of nearby stations and the two LARSE lines are shown in Figure 31. The crustal thickness estimates for stations within 15 km of each line are posted on the image sections in Figure 32 and Figure 33.

In both lines the crustal thickness estimates correlate well with the zones of low frequency high amplitude reflectivity, interpreted here as the Moho. Both of the Moho zones are rather complex, showing multiple levels of reflectivity. In both lines the Moho zones show a discontinuity near the San Andreas Fault. In Line 2 the Moho reflector appears to drop about 8 km north of the San Andreas, in Line 1 the Moho beneath the North American Plate is not imaged. The discontinuity in the Moho in Line 1 at the San Andreas tends to support the model put forth by Zhu (2002) rather than the sinking Moho model of Godfrey *et al*. (2002). The Moho reflector from Line 1 also shows a discontinuity associated with the San Gabriel Fault, an older extension of the San Andreas system. The two thickness estimates from the southern portion of Line 2

(stations CALB and DJJ) differ by about 3 km and coincide with an apparent discontinuity in the Moho reflector.

The crustal thickness estimate from station BTP is the only one that does not correlate well with the Moho reflection package. This estimate places the Moho some 5-8 km above the strongest portion Moho reflector zone. This location is, however, near a lens shaped package of reflectors, just above the main Moho reflectors. This could be local thickening of the Moho zone associated with the plate boundary, perhaps by duplication of the section in the lower crust by low angle faulting.

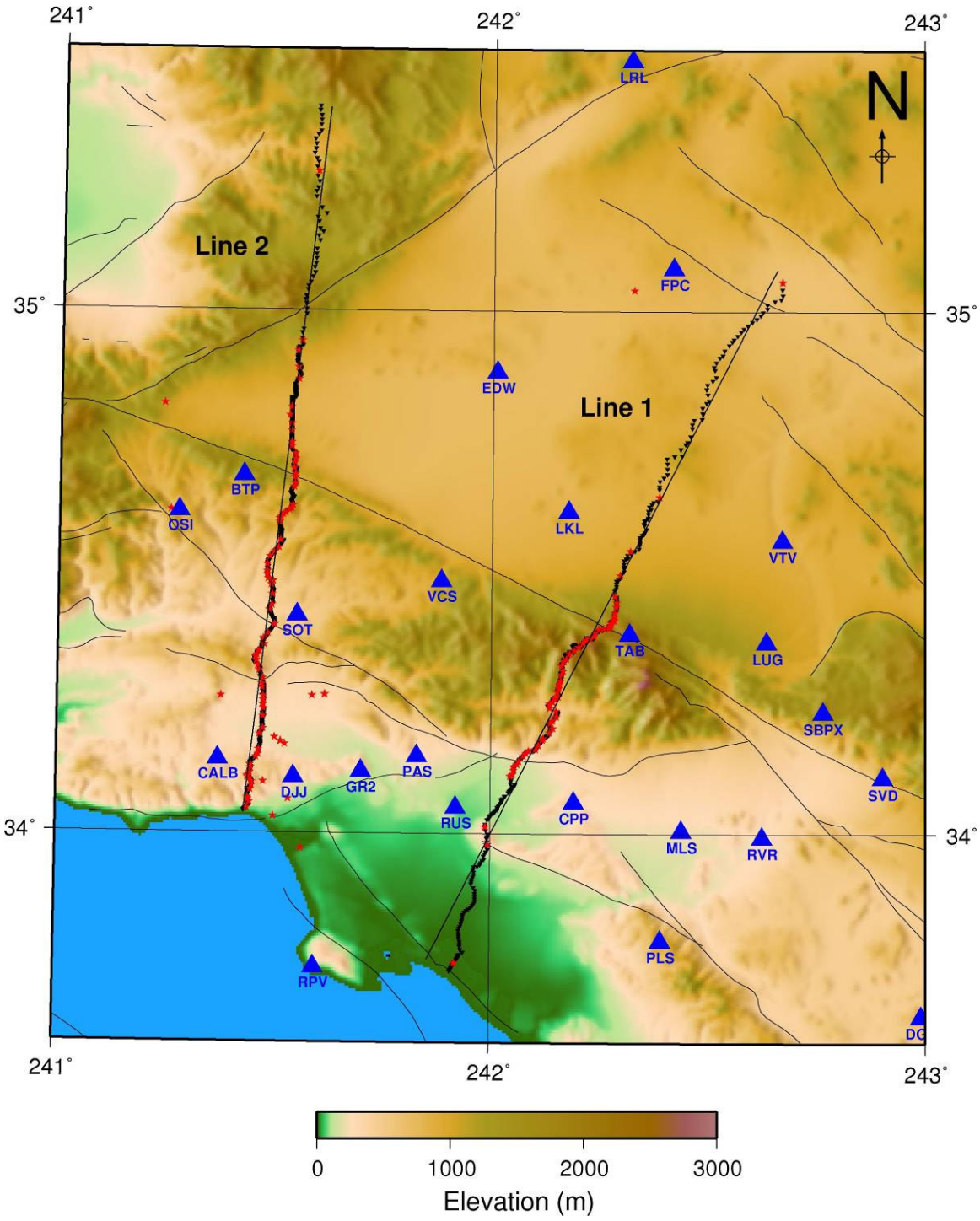


**Figure 31 – Map of southern California showing location of broadband stations (blue) used by Zhu and Kanamori, (2000) and LARSE lines 1 and 2.**

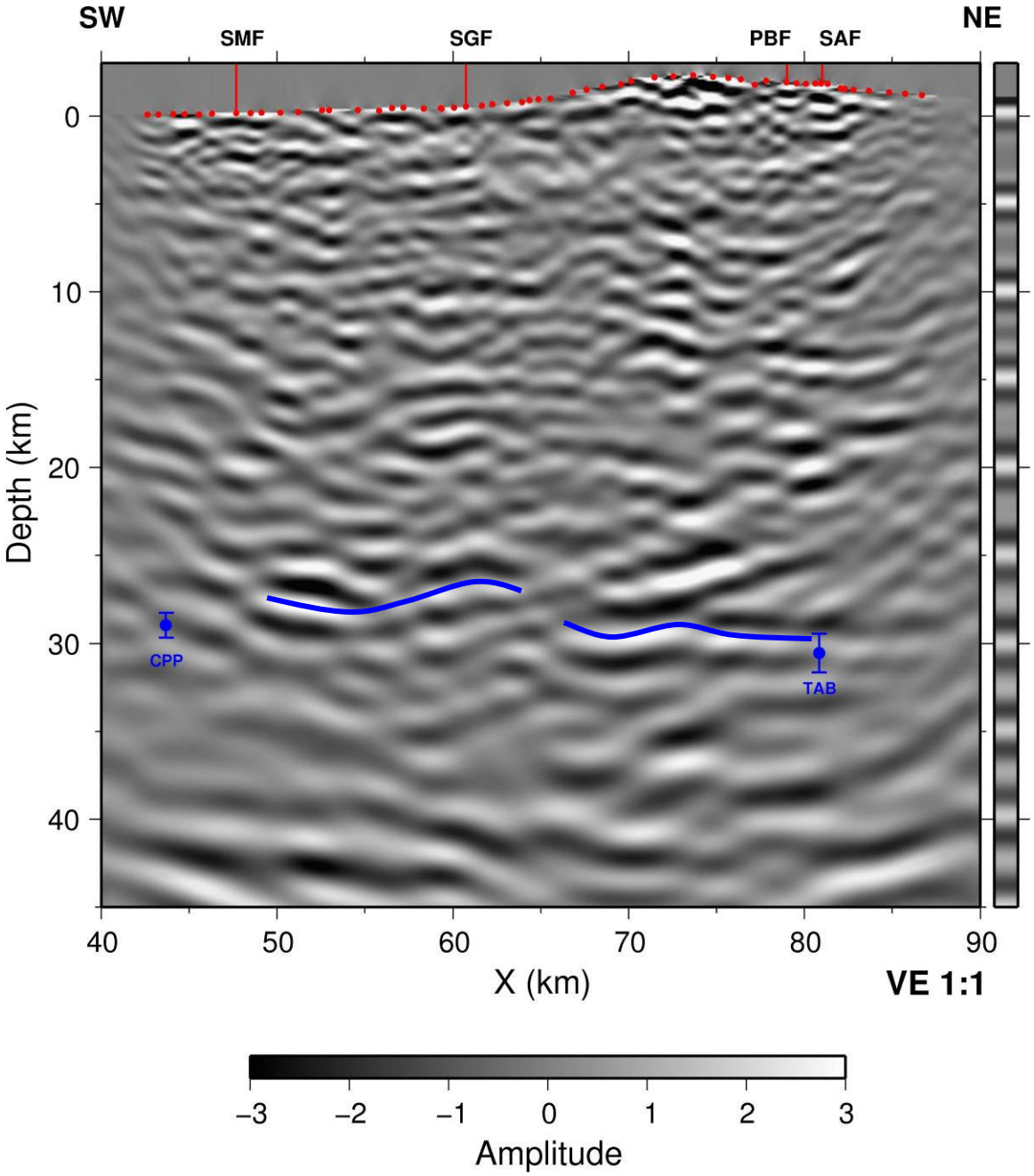


**Figure 32 - Composite stack for Line 1 with crustal thickness estimates from Zhu and Kanamori (2000) for stations TAB and CPP posted as blue circles with error bars. Interpretation of Moho reflectors shown as blue lines.**

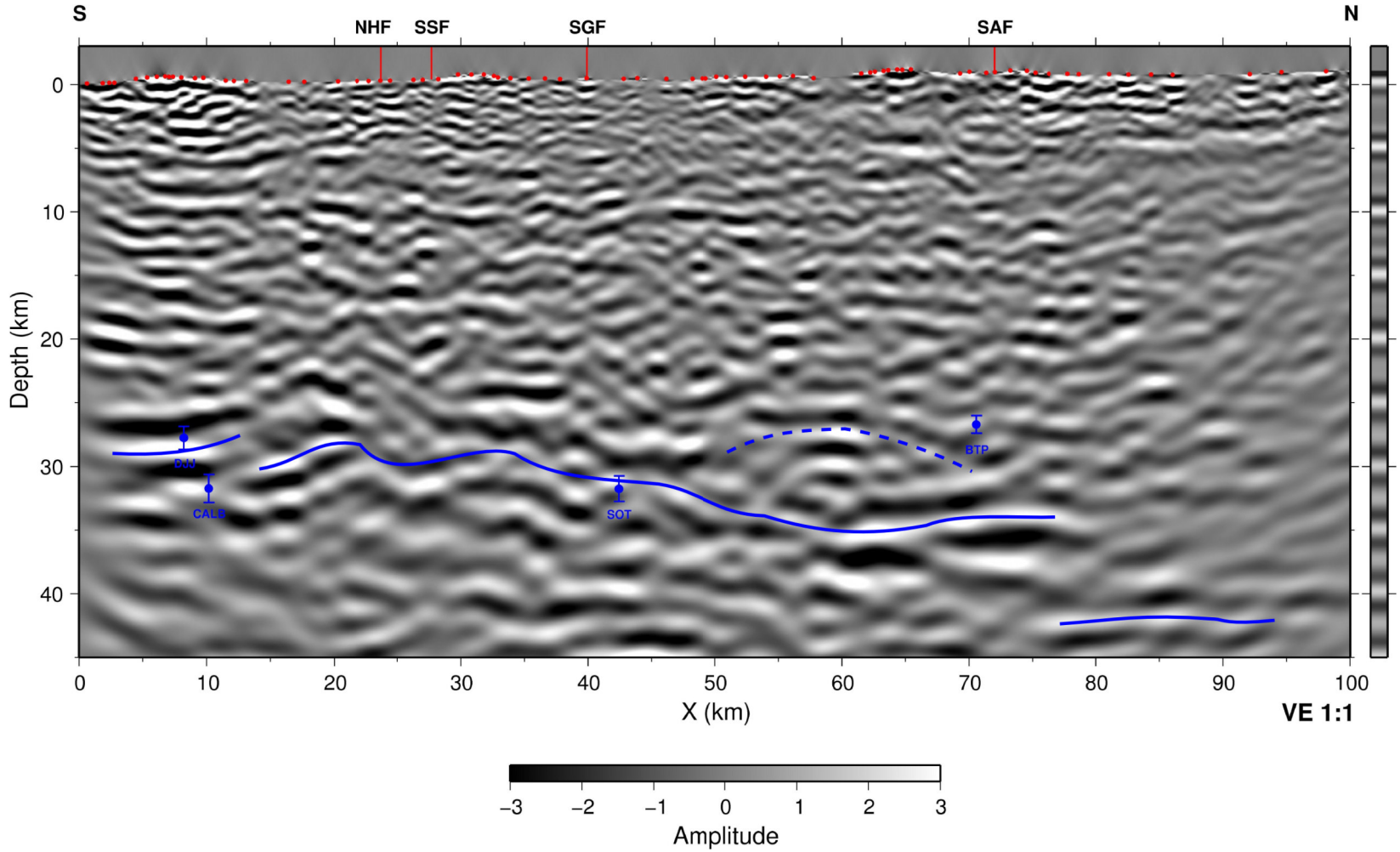


**Figure 33 – Composite stack for Line 2, with crustal thickness estimates from Zhu and Kanamori (2000) for stations CALB, DJJ, SOT and BTP posted as blue circles with error bars. Interpretation of Moho in blue, possible thickening of Moho zone shown as dotted line.**

The second study (Zhu, 2002) used the passive data sets collected by the LARSE program along Lines 1 and 2 to construct common conversion point (CCP) stacks of the teleseismic P to S converted amplitude. The portion of Zhu's CCP section corresponding to the imaging area for Line 1 is shown in Figure 34.

Composite depth sections with center frequencies of 0.4 Hz were constructed to compare to the CCP section. The composite section for Line 1 is shown in Figure 35 along with a schematic interpretation of the CCP section from Figure 34. Figure 36 shows Zhu's CCP section computed for Line 2. Figure 37 shows a 0.4 Hz composite stack for Line 2 with a schematic interpretation of the CCP section from Line 2.

Correlating the converted PS amplitudes and migrated reflection images is complicated by several factors. Depth errors can be induced by errors in the estimated $V_p/V_s$ ratios (Zhu 2002); anisotropy can have similar effects. Differences in image wavelengths and potential polarity differences between PP and PS images make it difficult to correlate events between the two sections. However, even though individual events are difficult to correlate, in both cases the CCP sections and the reflection images do show remarkably similar patterns of events.

Zhu interprets features A and B in Figure 34 and Figure 35 as the Moho; the discontinuity between them associated with the plate boundary at the San Andreas Fault. Feature A is paralleled by a strong band of reflectivity below it in the reflection image. The

northeasterly dipping features C and E are paralleled by a similarly dipping set of events in the reflection image. The negative polarity feature D parallels a set of strong reflection events just above it in the depth section.

Event A in Figure 36 is interpreted by Zhu as the Moho. In the Line 2 depth migration, this feature is paralleled by a series of bright reflection events. The north dipping features B and C correlate to a package of similarly dipping reflectors. Correlations for events D and E are less certain; however, they are located near isolated patches reflectors in a relatively quiet area.

For both lines, the low frequency composite sections agree well in overall structure and character with both the CCP sections and the teleseismic crustal thickness estimates. Both the CCP and the thickness estimates were made without the seismic reflection data set. Verification by two independent estimates provides evidence that these images represent actual primary reflectivity.

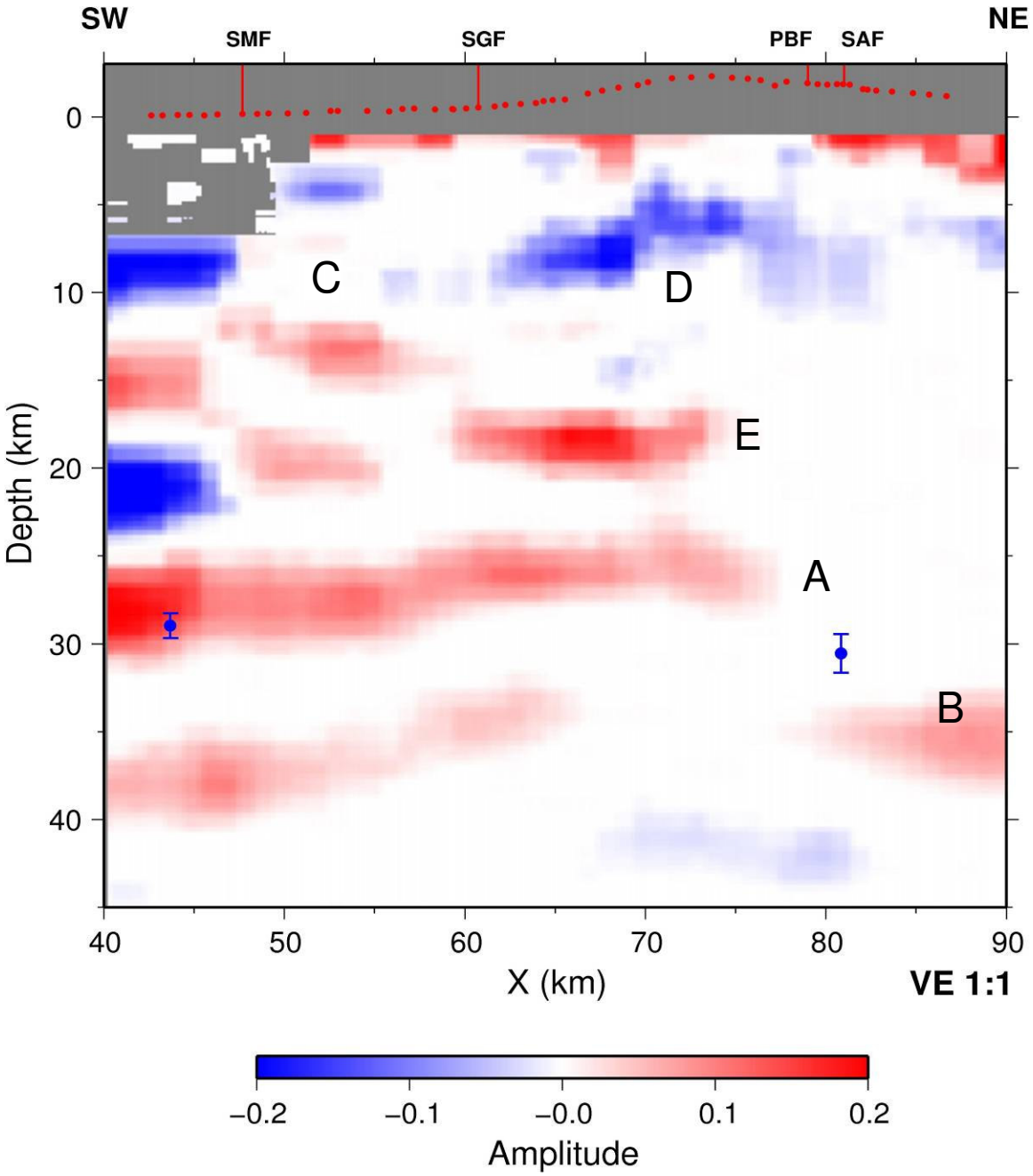


**Figure 34 – Common conversion point stacks of PS converted amplitudes for Line 1 from Figure 2 of Zhu (2002). Major features labeled A-E. Crustal thickness estimates from Zhu and Kanamori (2000) posted in blue.**

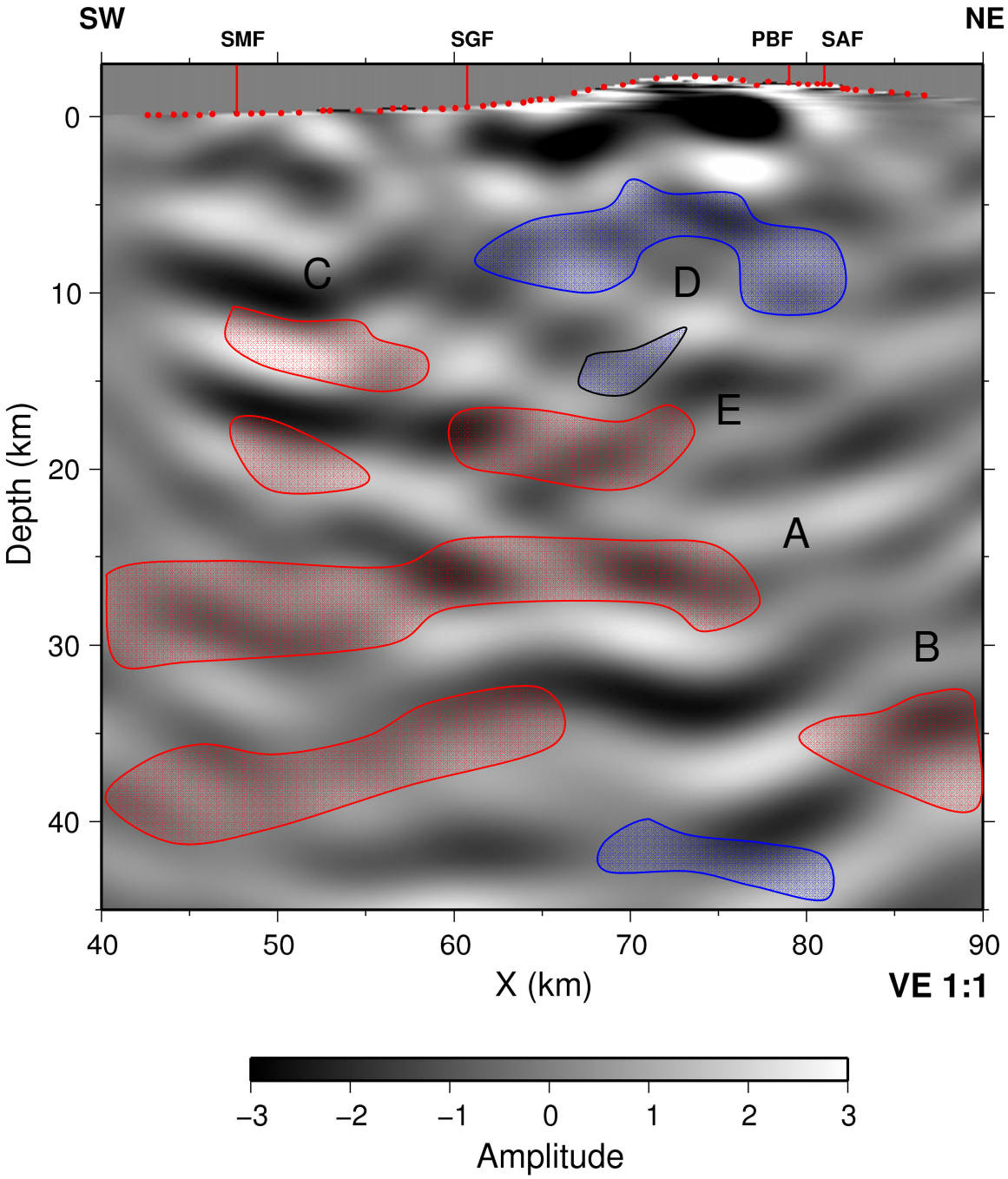


**Figure 35 - 0.4 Hz composite depth migration of Line 1. Interpretation and labels from Figure 34 superimposed. Gross structure of composite section matches that of CCP stack.**

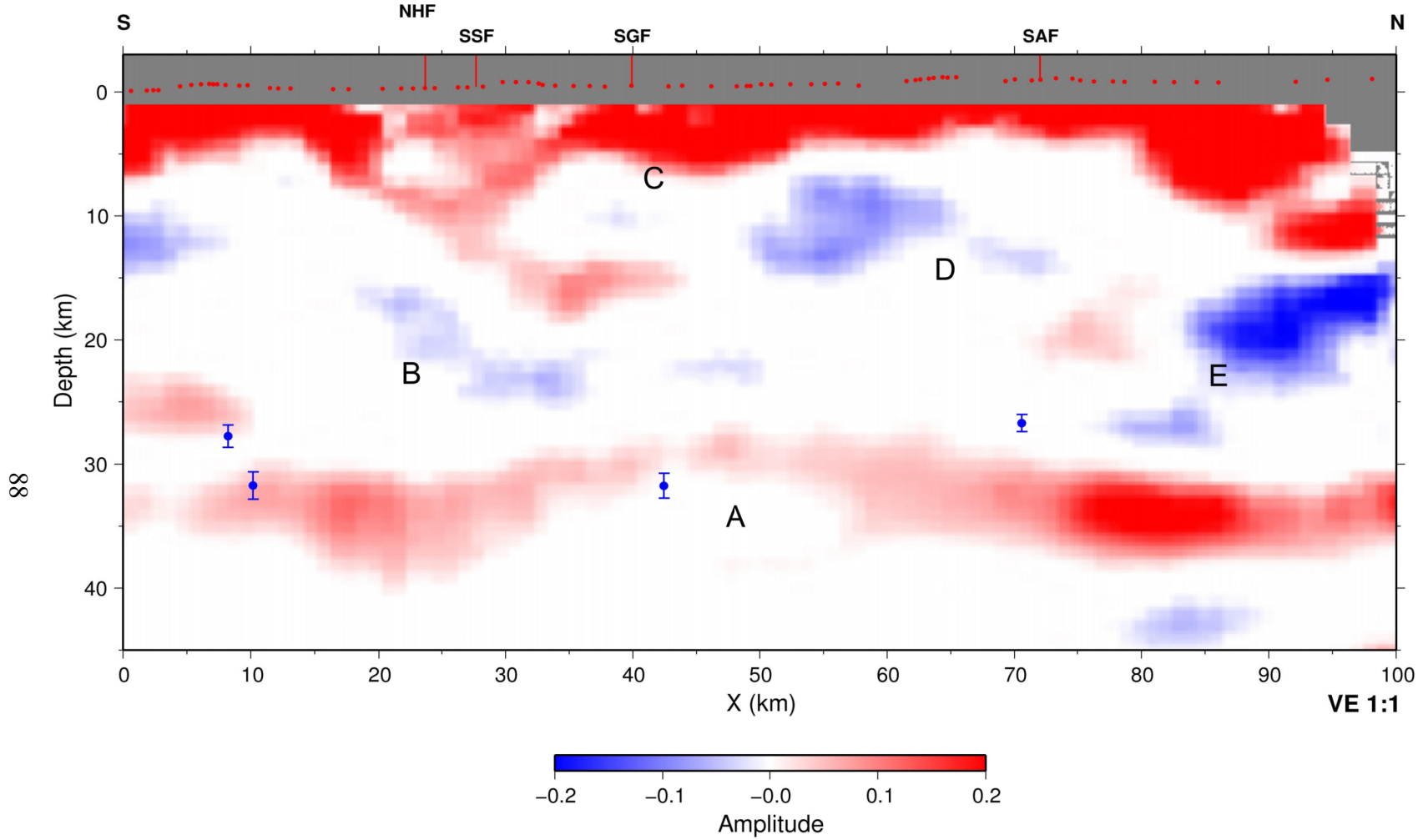




**Figure 36 - Common conversion point stacks of PS converted amplitudes for Line 2 from Figure 2 of Zhu (2002). Major features labeled A-E. Crustal thickness estimates from Zhu and Kanamori (2000) posted in blue.**

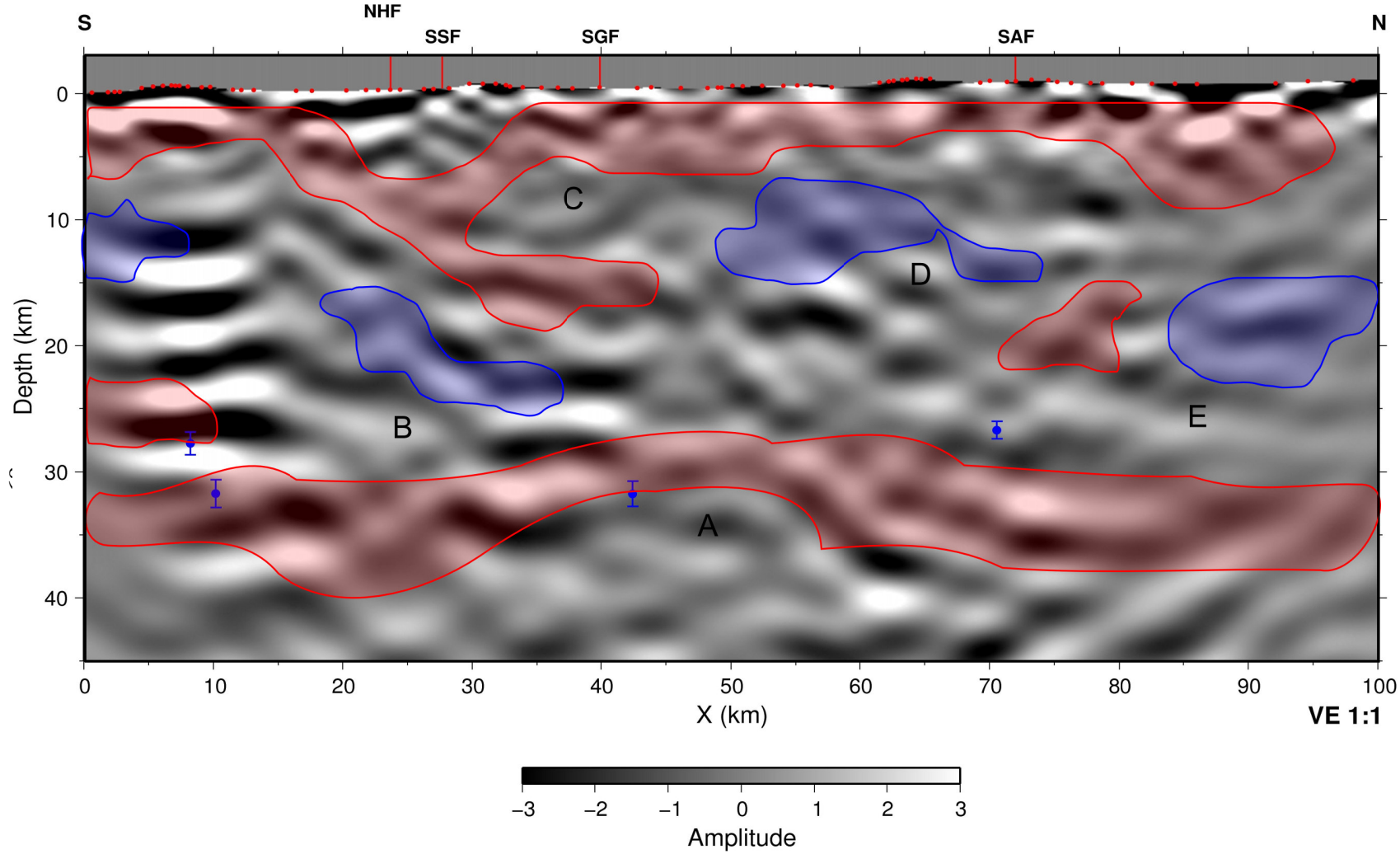


**Figure 37 - 0.4 Hz composite depth migration of Line 2. Interpretation and labels from Figure 36 superimposed. Gross structure of composite section matches that of CCP stack.**

### *Comparison with local seismicity*

A second comparison was made between the depth migrated sections and local seismic events from the Southern California Seismographic Network (SCSN) data catalog. Figure 38 shows a map of local seismic events in the LARSE area covering the period 1932-2006. The local events shown have been limited to the "A" events, those with estimated location errors of 1 km or less.

Hypocenters located within 5 km of Line 1 are shown in Figure 39 superimposed on the composite stack. On the southwestern end of the line there is a cluster of hypocenters between 5 and 15 km deep (labeled A in Figure 39). Unfortunately, most of these events are on the edge of the image area, but some deeper hypocenters on the same trend extend further into the line and correlate well with a set of steeply northeasterly dipping reflections. This is interpreted as the root of the Whittier/Puente Hills fault zone.

On the northeastern end of the line, there is an intense cluster of hypocenters associated with the San Andreas Fault. The cluster is oriented mostly vertically, with a distinct break to the southwest at a depth of 8 km. The break to the southwest is associated with a bright reflection ("B" in Figure 39) in the composite stack with a very similar orientation to the hypocenter swarm.

This bright reflector is part of a series of reflector segments noted earlier. The association of these reflector segments with the traces of known transform faults and local seismic

activity suggests they are in fact images of the fault. They could be caused by juxtaposition of different lithologies across the fault or by localized impedance differences in the fault zone itself.

The center of Line 1 is much less seismically active than either end. The majority of the activity is tightly clustered around a sub-horizontal reflector (labeled "C" in Figure 39). The reflector appears at a depth of about 10 km between the Sierra Madre and San Gabriel Faults, then ramps up to a depth of 7-8 km north of the San Gabriel Fault. The upward ramp of this reflector occurs just north of the trace of San Gabriel Fault. North of the San Gabriel fault, the reflector separates a zone of higher reflectivity below it, from a quieter zone above it.

In order to determine the nature of this reflector, focal mechanism solutions were checked to determine the sense of motion for the hypocenters located near this reflector. Figure 40 shows a set of focal mechanism solutions (Hauksson 2000) for hypocenters located within 5 km of the line. The focal mechanism solutions show that recent motion along this sub-horizontal reflector is largely perpendicular to the line. One particular mechanism located on the ramp, shows nearly the same dip as the ramp. The reflector appears to be a mid-crustal shear zone accommodating the northwest to southeast shear stress imposed by movement between the Pacific and North American plates.

By taking a broader view of seismic activity near Line 1, two interesting observations can be made. Figure 41 shows the composite stack along with the larger set of hypocenters located within 10 km of the line. Within this wider area, seismic activity is limited to the upper 12-15 km of the crust, with distinct breaks in the lower boundary of this zone near the San Gabriel and San Andreas faults. The location of the break and the vertical offset near the San Gabriel Fault are consistent with the offset observed in the shear zone above it.

Secondly, seismic activity appears to be well correlated with areas of higher reflectivity. In the upper portion of Figure 41, five areas of weaker reflectivity are outlined. Note that these areas contain very few hypocenters and that seismic activity is typically concentrated in areas of higher reflectivity, although not all areas of high reflectivity are seismically active. This relationship suggests that the non-reflective zones indicate areas of more ductile, homogeneous rock.

Similar correlations between seismic activity and reflectivity can be made on Line 2. The southern portion of Line 2 passes through an area of intense seismic activity (see Figure 38). This area is the junction of two conjugate reverse faults, the north dipping San Fernando system, and the south dipping Northridge system (Fuis *et al*., 2003). Figure 42 shows the composite stack for Line 2 along with hypocenters located within 15 km of the line and magnitudes greater than 2.5, and the aftershocks associated with the 1971 San Fernando and 1994 Northridge earthquakes. Line 2 passes within 1 km of the epicenter of

the 1994 Northridge earthquake; the 1971 San Fernando earthquake occurred 13 km to the east of the line. Seismic activity in the immediate vicinity of the line is dominated by activity along the Northridge system, forming a distinct south dipping trend. The SCSN catalog contains fewer events associated with the older San Fernando earthquake; these events form a less distinct pattern of activity. Local activity away from these two fault zones is sparse and trends are difficult to determine.

Again, seismic activity seems to be closely associated with areas of high reflectivity; in fact, the largest magnitude events and the densest clusters are associated with the brightest reflectors. Two non-reflective zones immediately adjacent to the Northridge event trend are largely free of hypocenters, consistent with the observations from Line 1.

Figure 43 and Figure 44 show the CCP sections from Zhu (2002) with local seismic activity superimposed. In Line1 there is a weak correlation between local activity and stacked amplitude. The zone of negative amplitudes (A and C) seems to parallel the pattern of local earthquakes. However, the pattern of local activity continues past event A and into the positive event B. In Line 2 a similar weak correlation can be seen. Local events correlate well with the positive south dipping arm of event A, but continue past this event into the negative event B.

The spatial correlation between local seismic activity and reflectivity has two important implications. It provides further evidence that the imaged reflections represent subsurface

structure. The association of seismic activity with high reflectivity and, equally important, zones of low activity with areas of low reflectivity suggests that faults or at least fault prone areas form a significant portion of the observed reflectivity. This relationship can be used to constrain the location of fault zones in the subsurface.

The sets of bright reflector segments noted earlier are a good example of how this relationship can be used. These sets of reflectors appear to form a connecting link from the surface location of a fault through known seismic activity in the shallow crust to structures in the deep crust, which allows one to infer the subsurface location of the fault.

The better correlation of the reflection images to local seismic activity than the PS converted amplitudes sections indicates that the higher resolution reflection sections can provide more precise locations for these faults.

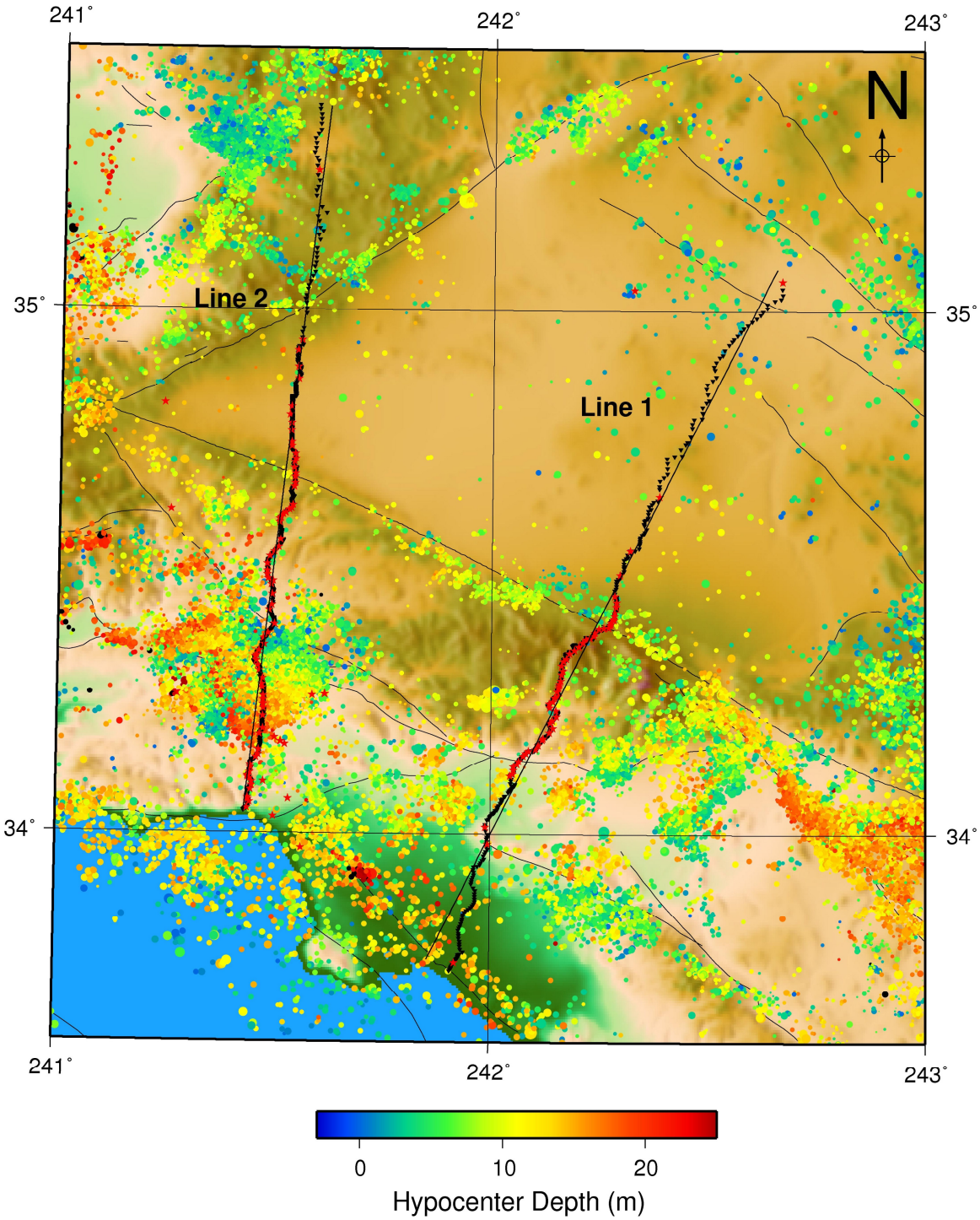


**Figure 38 - Map southern California with seismic events from 1932 to present and location of LARSE lines. Radius of circle indicates relative magnitude of seismic event, color indicates hypocenter depth.**

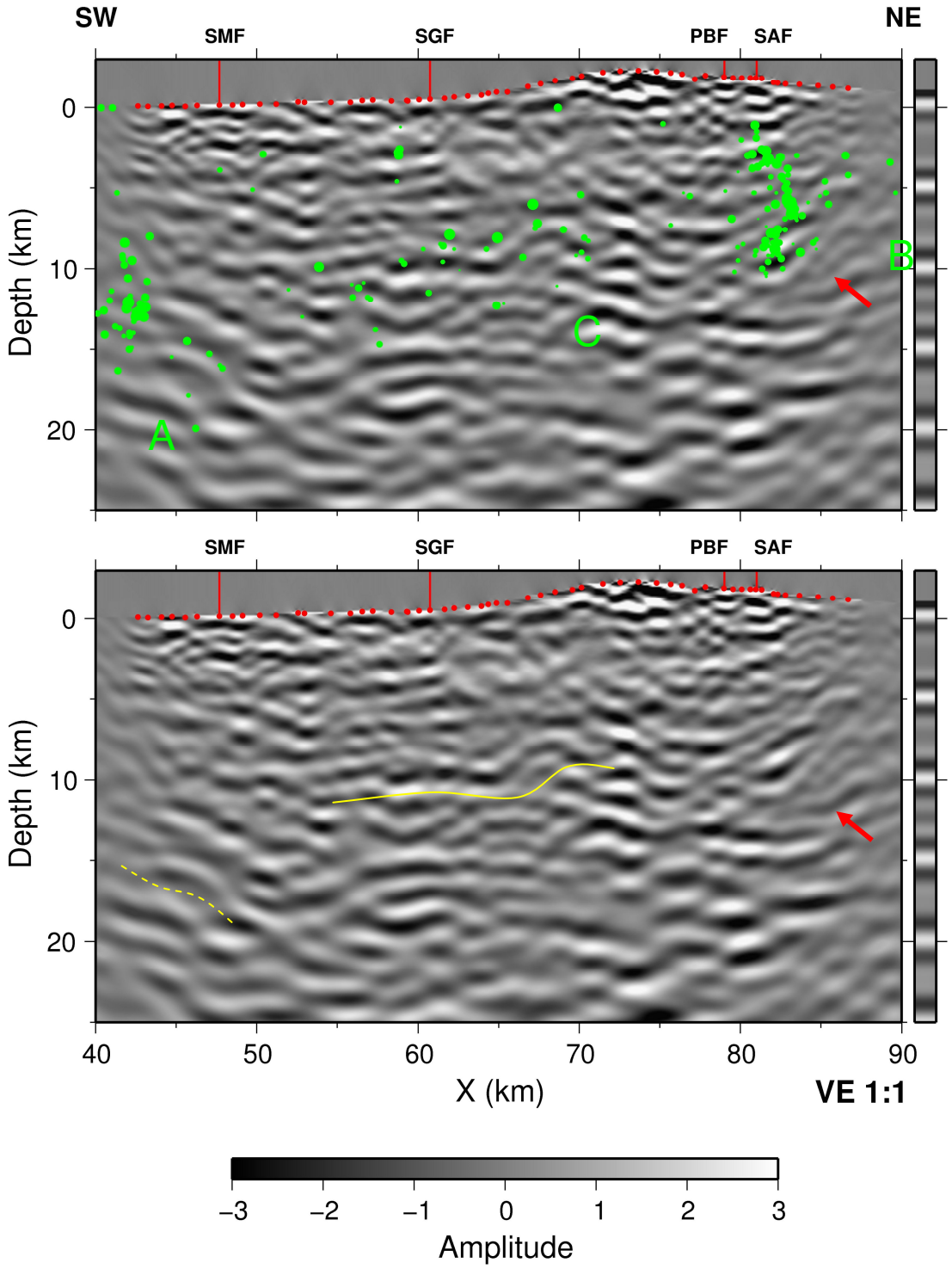


**Figure 39 – Composite stack for Line 1. Above: hypocenters within 5 km of line posted in green. Below: interpretation of two fault zones in yellow. Red arrow highlights bright reflector segment associated with seismicity along San Andreas Fault.**

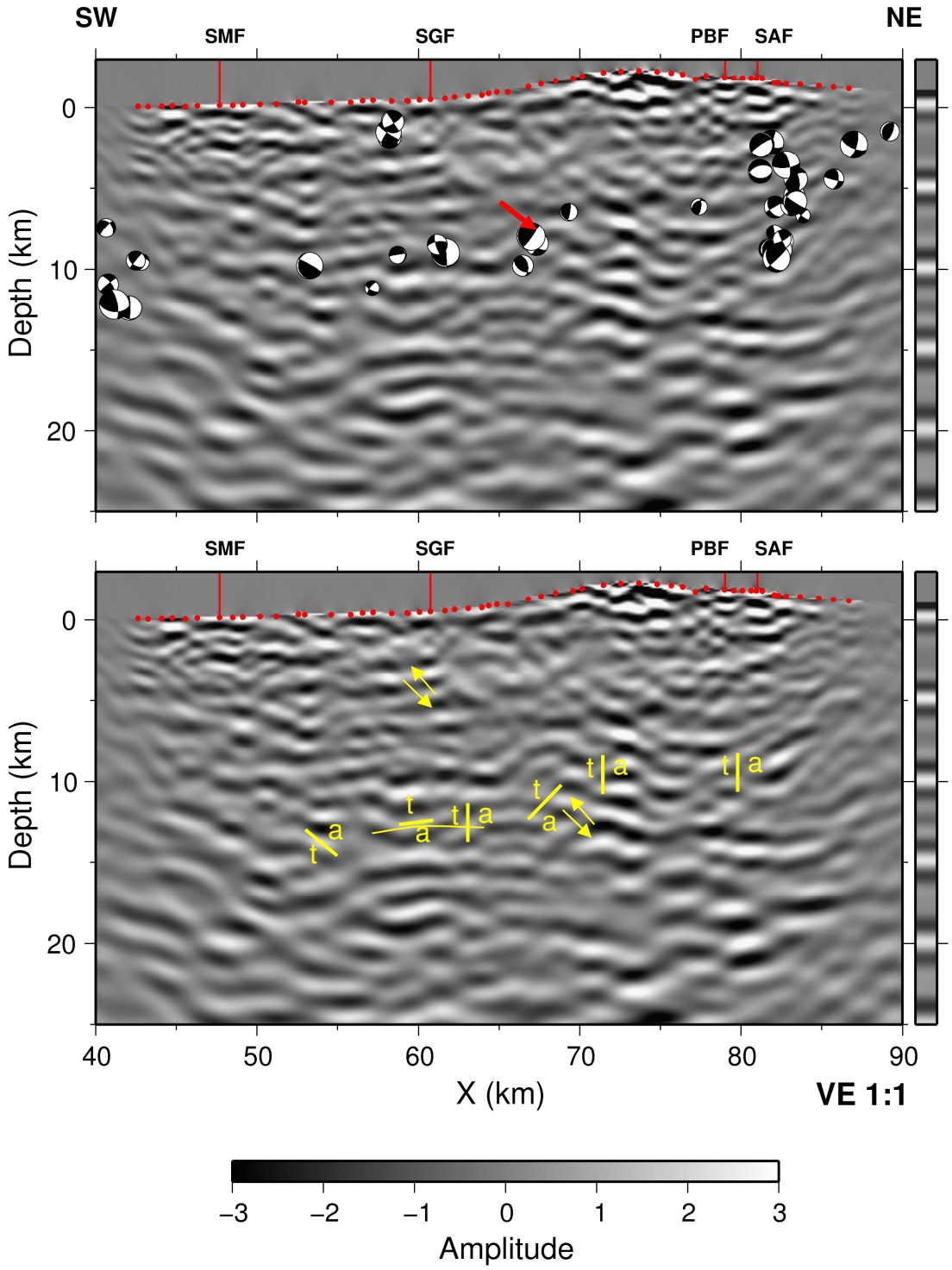


**Figure 40 - Composite stack for Line 1. Above: focal mechanisms (Hauksson, 2000) for hypocenters located within 5 km. Below: interpretation of fault motion, *t* indicates motion towards the reader, *a* indicates motion away from the reader. Red arrow highlights event parallel to imaged reflector.**

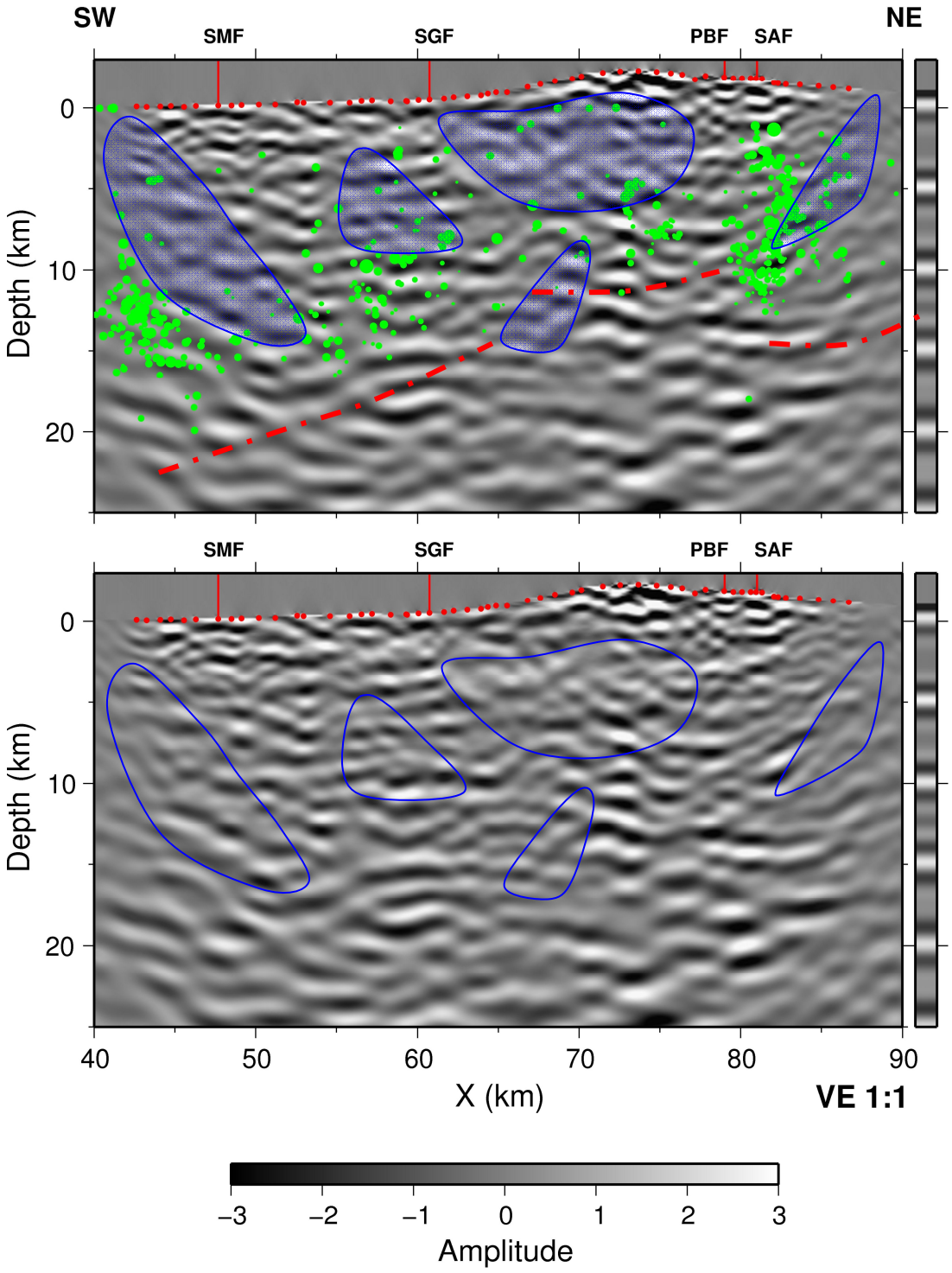


**Figure 41 - Composite depth section for Line 1. Above: hypocenters within 10 km of line posted in green. Low reflectivity zones highlighted in blue, lower limit of local activity in red. Below: Outlines of low reflectivity zones in blue.**

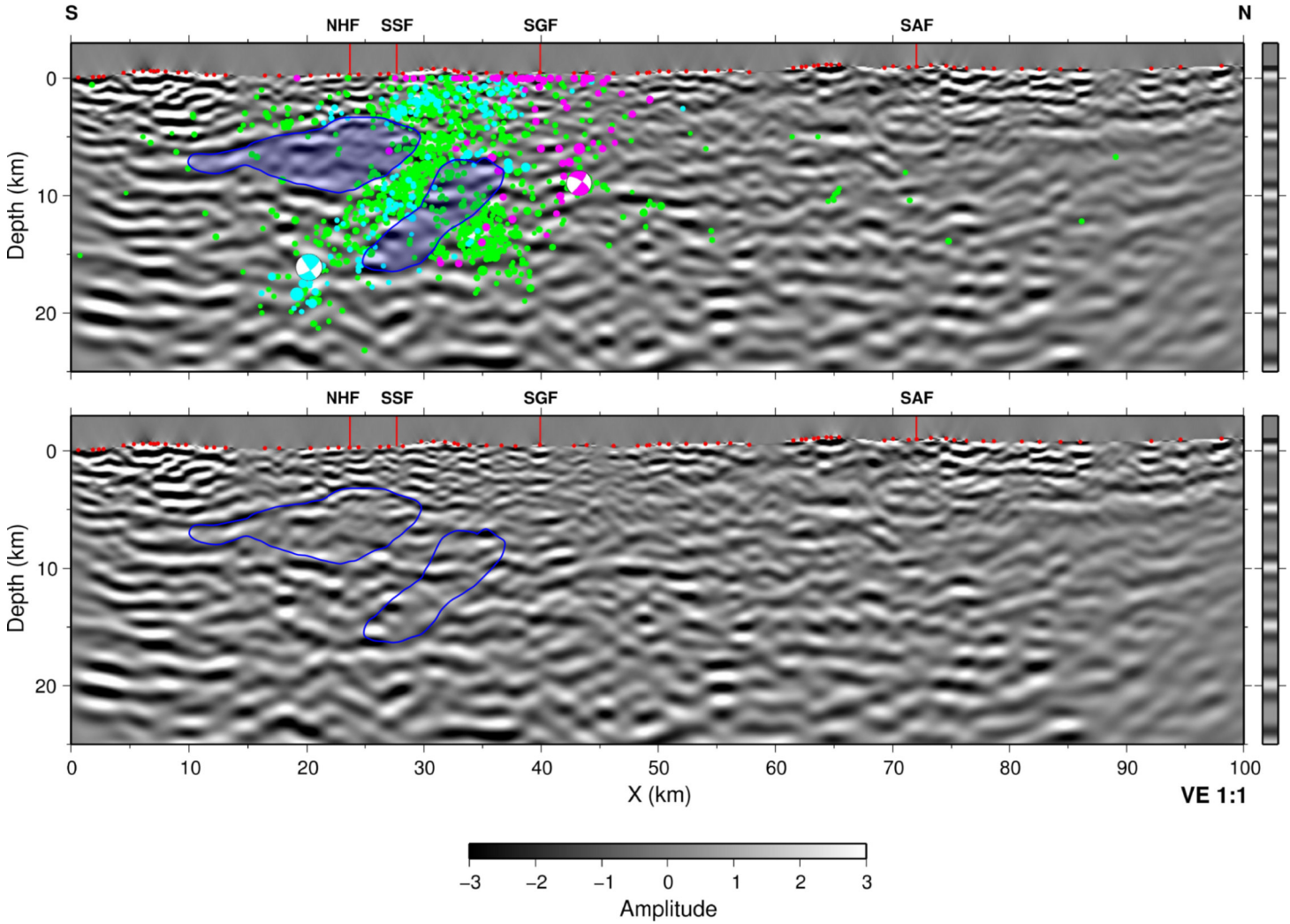


**Figure 42 - Composite stack for Line 2. Above: Events within 15 km and M>2.5 shown in green, 1971 San Fernando earthquake and aftershocks shown in magenta, 1994 Northridge earthquake and aftershocks shown in cyan. Low reflectivity zones highlighted in blue. Below: Low reflectivity zones and hypocenters for Northridge and San Fernando earthquakes**

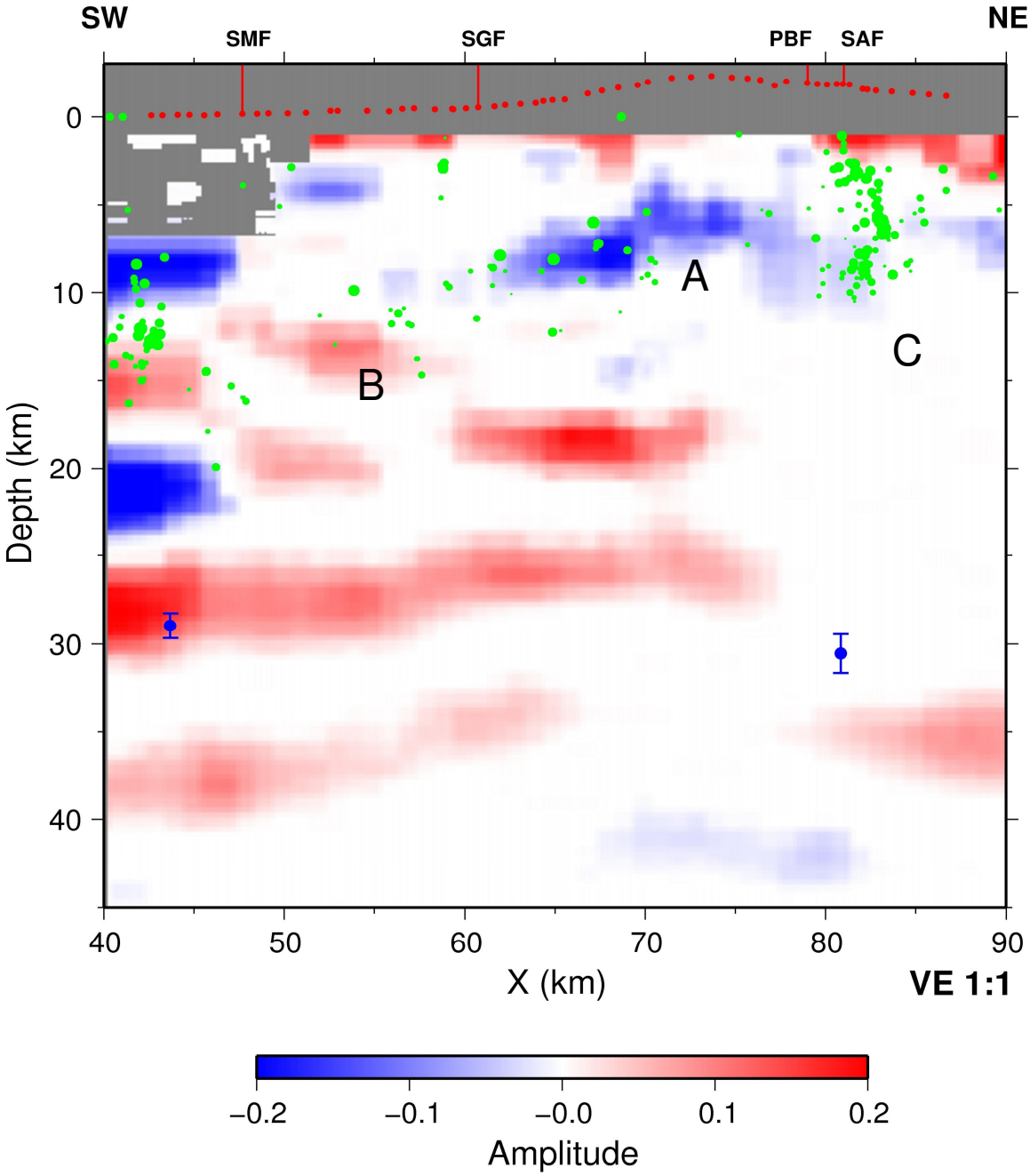


**Figure 43 - Common conversion point stacks of PS converted amplitudes for Line 1 from Figure 2 of Zhu (2002), hypocenters within 5 km in posted in green.**

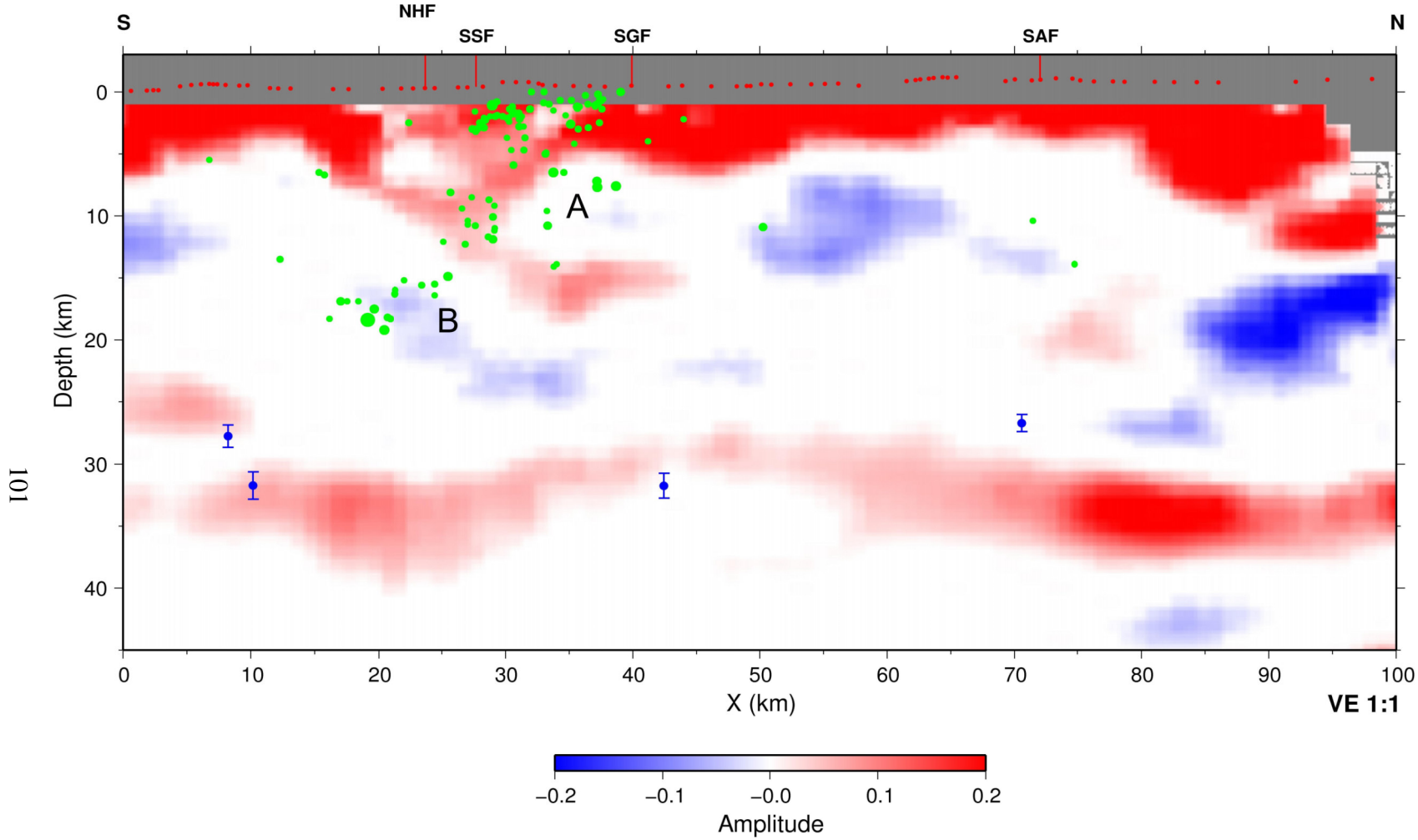


**Figure 44 - Common conversion point stacks of PS converted amplitudes for Line 2 from Figure 2 of Zhu (2002) with local seismicity within 5 km in green.**

## *Interpretation of depth sections*

As a demonstration of the potential improvement in the level of geologic understanding made possible by the improved imaging, simple interpretations of these images were made. The interpretation of the depth image produced for Line 1 is shown in Figure 45.

The San Andreas and Punch Bowl faults follow a series of bright reflector segments which lead down to the northward termination point of the interpreted Moho reflection. The position of the Moho on the North American side of the fault is not well imaged. The break in the lower limit of local seismicity on either side of this series of reflectors also suggests a fault.

The San Gabriel Fault is considered to be an older branch of the San Andreas Fault with a total offset of 40-60 km in this area (Fuis *et al*. 2001). The interpreted position of this fault follows a similar series of reflector segments that trend into a second discontinuity in the Moho reflection. The interpreted fault also runs through the point of the change in depth of both the shear zone and the lower limit of local seismicity. This fault position also separates a more reflective unit to the southwest from a less reflective unit to the northeast, indicating a change in lithology across the fault. The sense of the depth changes in the Moho reflection, the lower bound of seismicity and the shear zone all suggest that the crust between the San Gabriel and San Andreas faults has been uplifted. This uplift could be due to thickening of the Moho zone, suggested by the strong reflector just above the interpreted Moho position.

The Sierra Madre Fault zone is interpreted to follow a weakly imaged set of dipping reflectors which trend towards the shear zone. The shear zone is a likely decollement surface for this fault zone. The root of the Whittier Fault zone parallels a set of north dipping events on the southwestern edge of the section.

An interpretation of Line 2 is shown in Figure 46. The base of the San Fernando and Santa Clarita basins are imaged at a maximum depth of 5 km. The base of the sedimentary basin is marked by an abrupt transition from a zone of high amplitude, high frequency reflections to a zone of lower amplitude, lower frequency reflections. A similar transition can be seen at the base of the sedimentary basin just north of the San Andreas Fault.

Here again the San Andreas Fault follows a set of bright reflector segments which trend into the discontinuity in the Moho. A second trend of segments forms a north dipping splay off the main fault. The position of the main fault separates a more reflective unit to the south from a less reflective unit to the north.

The trend of activity along the Northridge fault zone leads into the discontinuity in the Moho reflection at the southern end of the line. This suggests that this fault zone has penetrated into the upper mantle, or is in fact set up by a thrusting in the lower crust.

Exploration wells and seismic reflection surveys in the San Fernando Valley show that the Northridge Hills and Santa Suzana faults have shallow dips to the north and the San Gabriel fault is nearly vertical (Fuis *et al*., 2003). A series of bright reflector segments lead from the trace of the San Gabriel Fault at a steep angle towards the hypocenter of the San Fernando earthquake. The deep extension of this fault follows from the interpretation of Line 1. It is interpreted here to be a nearly vertical fault penetrating to the Moho. The interpretation here follows a trend that parallels the general sense of dip above 10 km, separates of a zone of higher reflectivity to south from a lower reflectivity zone to the north, and intersects the Moho near the edge of the lens shaped thickening of the Moho. The deeper portion of the San Fernando fault zone is more difficult to decipher. The trajectory of the fault below 10 km was chosen to parallel the orientation of the San Fernando focal mechanism and follow a weak reflector with nearly the same dip.

The improvements in image quality achieved here have led to the identification of six previously unknown crustal features in the southern California. In Line 1 the mid-crustal shear zone, the Moho discontinuity at the San Gabriel Fault and the thickening of the Moho zone at the San Andreas Fault are all previously unknown. In Line 2, the discontinuity of the Moho at the San Andreas, the interaction of the Northridge fault system with the Moho, and the thickening of the Moho at the San Andreas are all newly described features. These newly identified features indicate the potential improvements in the understanding of crustal geology made possible by this technique.

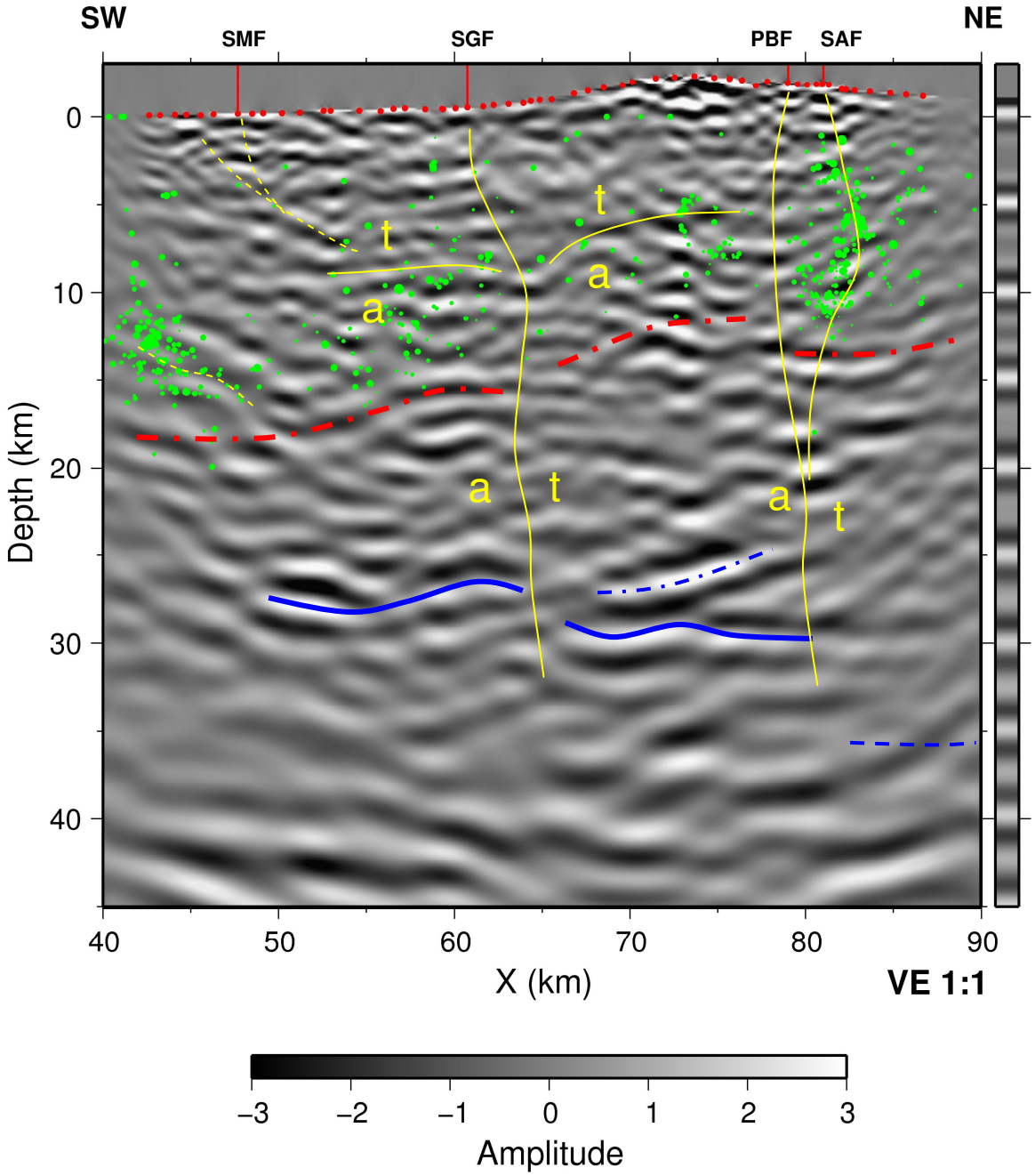


**Figure 45 - Preliminary interpretation of Line 1. Faults in yellow, Moho in blue, local seismicity in green, base of seismicity in red. *t* indicates motion towards reader, *a* indicates motion away from reader.**

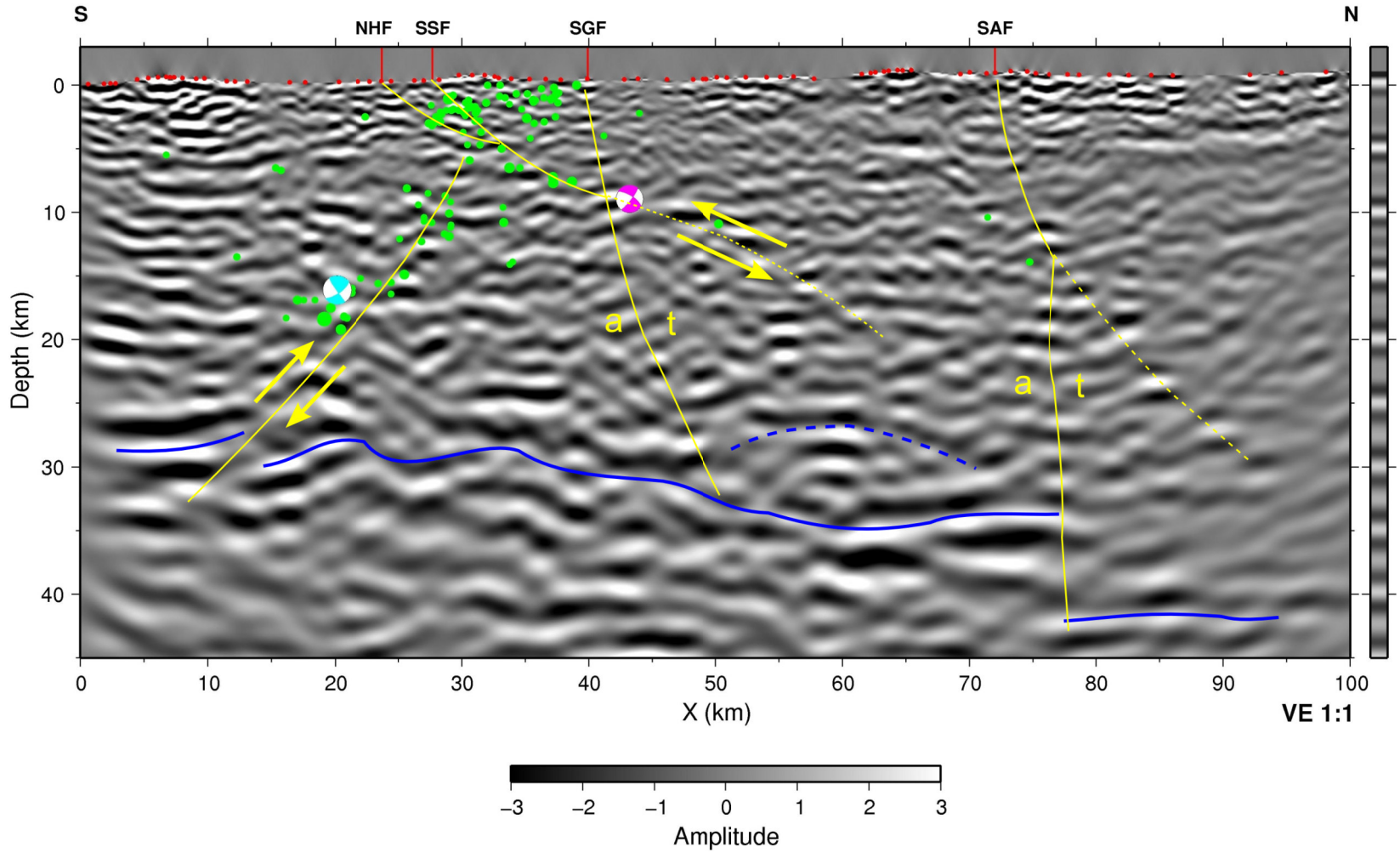


**Figure 46 - Preliminary interpretation of Line 2. Moho in blue, faults in yellow, base of sedimentary basins in orange. Local seismicity in green, focal mechanism for 1971 San Fernando earthquake in magenta, 1994 Northridge earthquake in cyan. *t* indicates motion towards reader, *a* indicates motion away from reader.**

## *Comparison with previous images*

The images for both lines presented here are substantially improved over previous efforts. Figure 47 shows a comparison of the Line 1 image produced here and the previous image obtained by Henyey *et al*. (1999). Events in the previous section are weakly imaged with little continuity or resolution. The primary sense of dip is to the northeast, opposite of that in wave equation migration. The wave equation migration shows no consistent "strongly reflective" zone. Likewise, the Moho event noted in the previous interpretation correlates poorly with the wave equation migration.

Figure 48 shows a comparison for the Line 2 images. Similar levels of improvement in the resolution and continuity of reflectors are evident in the depth migration of this section as well. The sedimentary basins are imaged in both sections. The bright reflectors near the San Andreas Fault reported by Fuis *et al*. (2003) are imaged in the wave equation migration as a relatively low amplitude zone. The strongest reflectors in the depth image, those from the Moho, are not present at all in the previous section.

Figure 49 and Figure 50 show envelope stacks recreated for Lines 1 and 2 following the processing flow reported by Ryberg and Fuis (1998). The input traces had median AGC and a 10 Hz low cut filter applied before the envelope calculation. The envelope traces were then moveout corrected, stacked and elevation statics were applied. Note that the color map has been squeezed significantly to emphasize the subtle amplitude variations.

The envelope stack for Line 1 shows features similar to those in the section from Henyey *et al*. (1999). The events in the envelope stack are more prominent after the low cut filter, indicating a significant high frequency component to these events. The bright event at 8 seconds, previously interpreted as a primary reflection, appears to be a diffraction event. It is difficult to determine the apparent velocity of this event; its moveout is consistent with both a primary reflection (6 km/s) and a reflected direct arrival (5.5 km/s). As noted previously, the direct arrivals are the strongest events in any shot record from either line, and the envelope stacking process is easily biased by high amplitude events. Also these events are most prominent in the northern portion of the line, the central portion of the San Gabriel Mountains. This part of the survey area has the most rugose topography, and offers many potential reflectors in the near surface for direct arrivals and surface waves. The high frequency content of these events, their high amplitude, the moveout of the events, their correlation to topography, and the insensitivity of the envelope stacking process to noise all suggest that the events in the envelope stack are not primary reflections but rather direct arrivals reflected offline somewhere in the San Gabriel mountains.

The envelope stack for Line 2 shows similar problems. The migrated section of Fuis *et al*. (2003) shows a 'V' shaped pattern of events centered at the San Andreas Fault (X=72 km) with the bottom of the 'V' at a depth of 24 km. In the envelope stack an 'X' shaped pattern of events can be seen at a similar position, consistent with the unmigrated position of the 'V' shaped zone. The center of the 'X' is located at the San Andreas Fault and an

arrival time of 8 seconds (from surface); the 8 second arrival time is consistent with a depth of 24 km and an average velocity of 6 km/s. Again, the events in the envelope stack are most prominent in the mountainous areas (the Central Transverse Range spans the range of X from 50 to 80 km), and are most prominent in the low cut filtered stacks. What is more telling about these events is the apparent velocity of these linear events; the approximate velocity is 5 km/s for both legs of the 'X', roughly the near surface P wave velocity. Furthermore, these events can be seen to roughly parallel near surface events which can be traced back to individual shot points.

I believe the significant differences between the images presented here and those from previous work are primarily due to the envelope stacking process. The events that were interpreted as primary reflections by previous researchers are not primary reflections, but actually direct arrivals and back scattered direct arrivals. The envelope stacking process is simply not an effective means to discriminate between signal and noise and leads to erroneous conclusions.

The new images show substantial improvements in resolution and reflector continuity throughout the entire section. This level of improvement will allow more accurate and detailed crustal models to be determined. As described before, these depth migrations have already revealed many crustal features invisible in the previous sections.

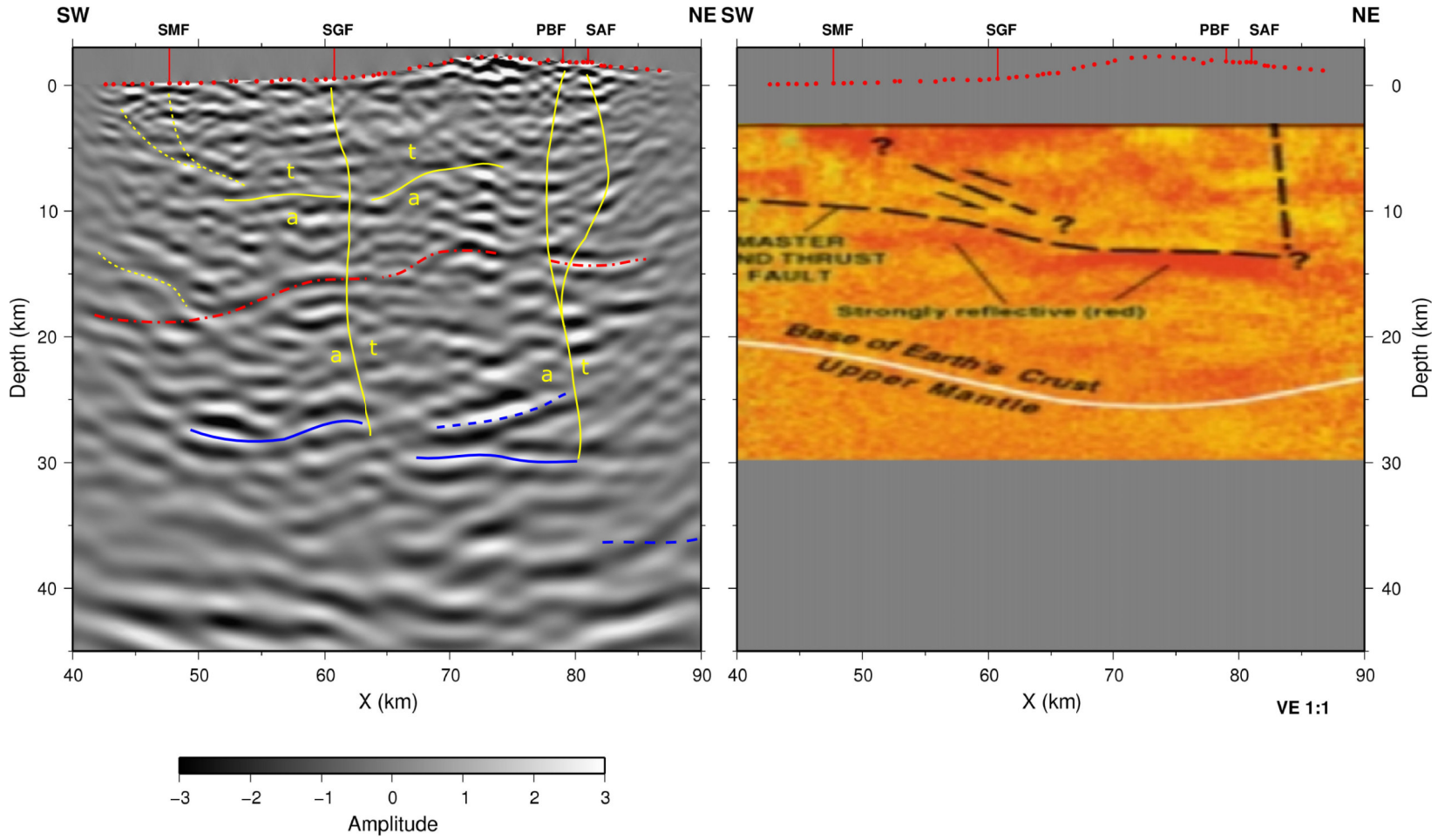


**Figure 47 - Comparison of Line 1 depth migration (left) with depth image (right) from Henyey *et al*. (1999).**

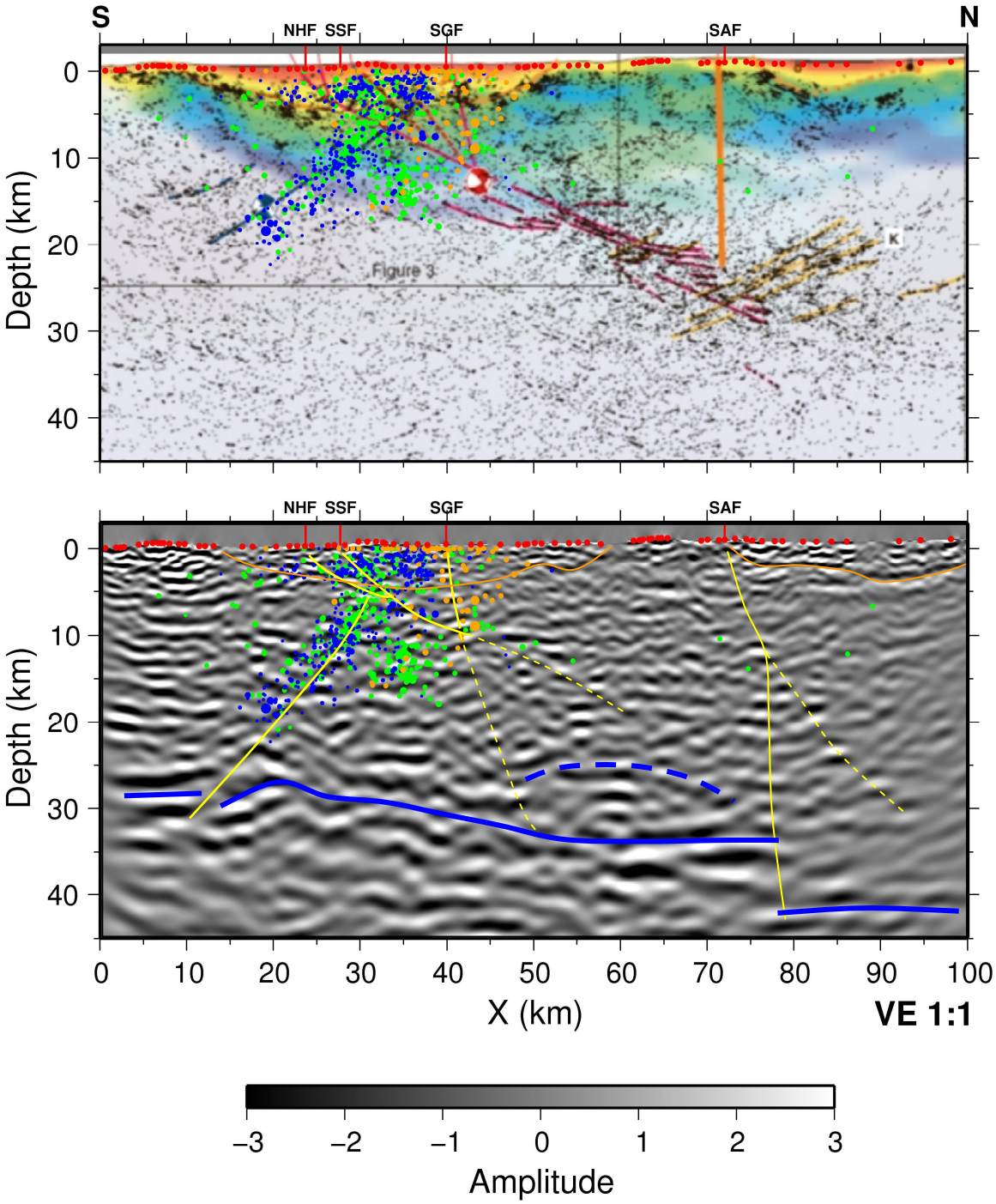


**Figure 48 - Comparison of Line 2 depth migration (below) to depth image (above) from Fuis *et al.* (2003).**

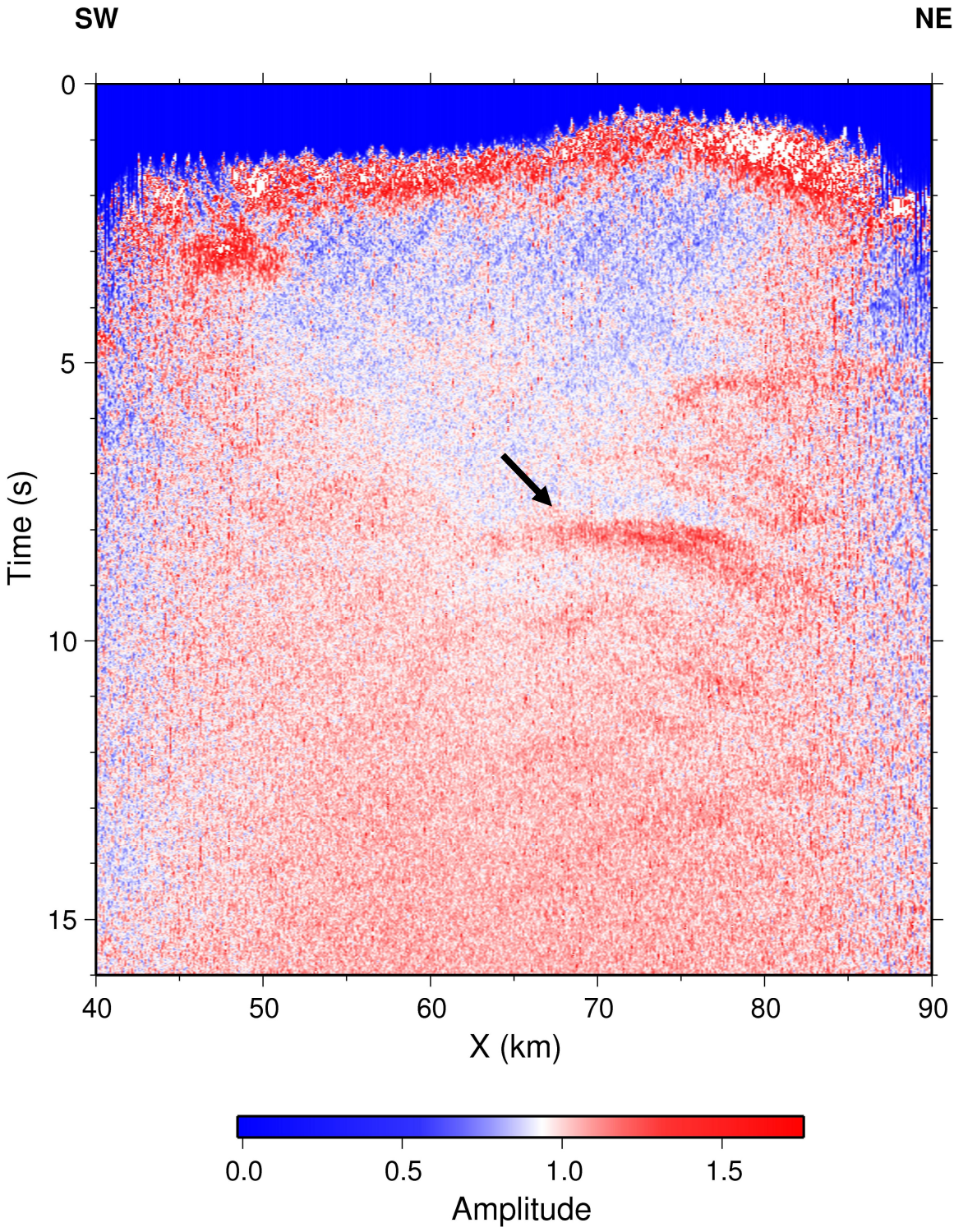


**Figure 49 - Envelope stack of Line 1. Input traces were low cut filtered to 10 Hz before envelope calculation. Arrow indicates location of reflected direct arrivals in stack.**

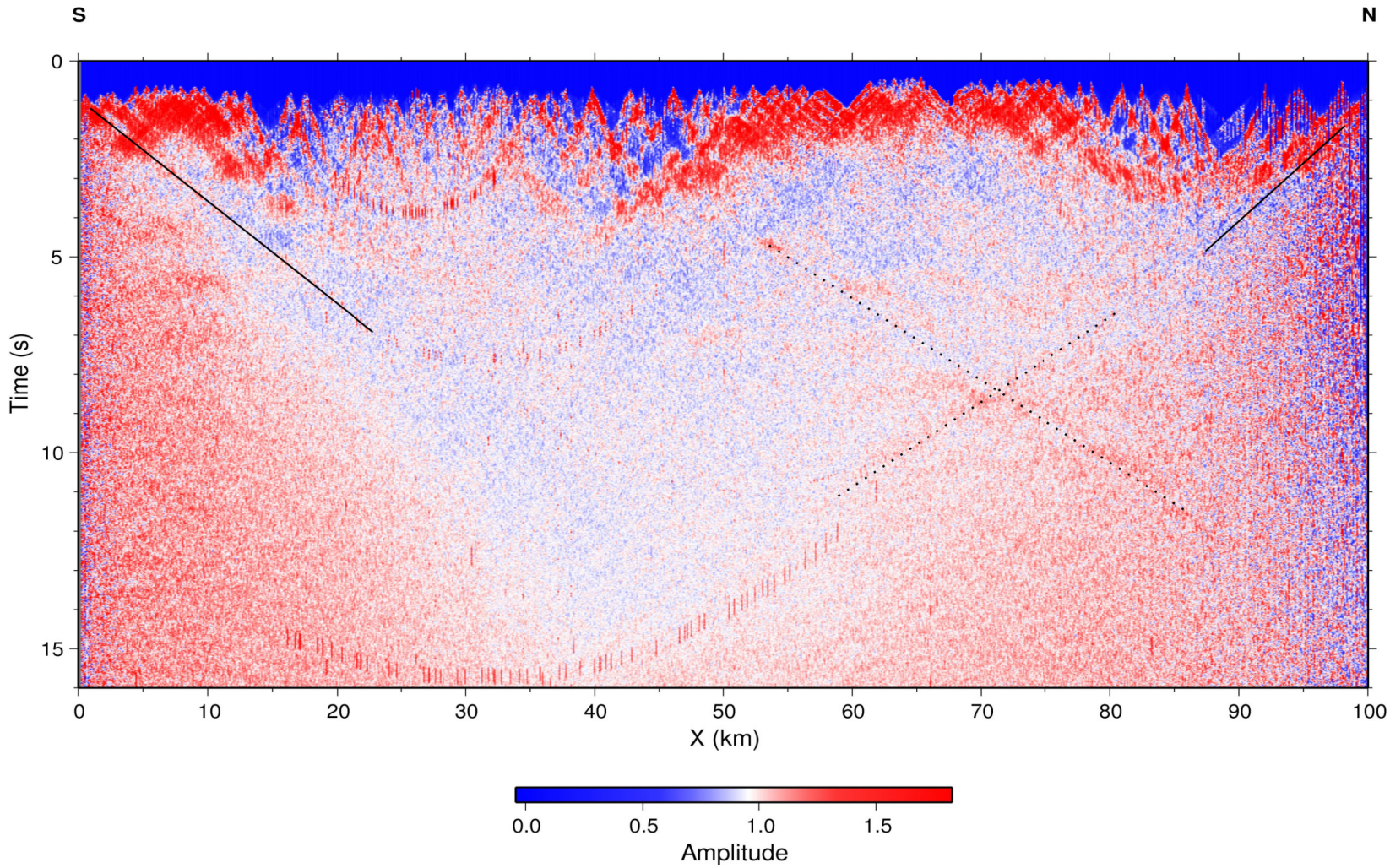


**Figure 50 - Trace envelope stack for Line 2. Direct arrivals show as solid lines, misinterpreted events shown as dotted lines.**

# Conclusions and future research

This dissertation has demonstrated that advanced imaging techniques can be reliably used to substantially improve the images obtained from deep crustal reflection surveys. In particular, wave equation prestack depth imaging is an effective and important tool for imaging weak reflection energy in the presence of noise. This type of imaging quality can dramatically improve the geologic understanding gained from crustal reflection surveys.

The images derived from the LARSE data by previous researchers were flawed by the envelope stacking process. The events that they imaged are not primary reflections, but rather direct arrivals and back scattered direct arrivals. The envelope stacking process is actually a very ineffectual technique for imaging weak signals in the presence of strong noise. The poor signal to noise ratios common to crustal imaging surveys demand more sophisticated imaging techniques, rather than the simplistic approaches commonly used.

The acquisition of a crustal survey takes considerable amounts of resources. To take full advantage of this investment, a reassessment of the typical imaging process is necessary. The techniques used here are feasible for any researcher; they can be (and were) carried out on a modern workstation. To continue to use the simplistic techniques of the past is a waste of time and money. An immediate extension of this research is to apply the techniques developed here to other crustal surveys to determine the robustness of the technique.

The quality of the new images from the two LARSE lines is a significant step towards fulfilling the original goals of the LARSE program: to better understand deep crustal structure and shallow fault geometries. To accomplish this goal, a more comprehensive interpretation of the new images incorporating the regional geology and tectonics should be carried out.

The finding that the optimal imaging bandwidth is in the 1 to 3 Hz range suggests that new acquisition in the LARSE program should be designed for this bandwidth. The reflection portions of the two lines collected to date have used recording systems designed for higher bandwidths. Data quality could potentially be improved by focusing the effort into the lower frequency band, by replacing the 4.5 and 8 Hz recording systems with 2 Hz or lower instruments.

Another area of further research would be the extension of the prestack wave equation technique to passive imaging. The economics of collecting of passive data are such that it will likely continue to be the major source of data for crustal studies. Chen *et al*. (2005a, 2005b) recast the wave equation reflection technique into a wave equation conversion technique to image receiver functions in the poststack domain. A similar application in the prestack domain might be able to produce images with resolution comparable to the reflection imaging from passive data sets. The LARSE program has collected both types of data along the same traverses, and offers an excellent opportunity to test this idea.

## References

Ali, M.Y., and A. B. Watts, 2003, A seismic reflection profile study of lithospheric flexure in the vicinity of the Cape Verde Islands, Journal of Geophysical Research, **108**, 2239.

Beasley, B. and W. Lynn, 1992, The zero-velocity layer: Migration from irregular surfaces, Geophysics, **57**, 1435-1443.

Brocher, T.M., R.W. Clayton, K.D. Klitgord, R.G. Bohannon, R. Sliter, J.K. McRaney, J.V. Garnder, and J.B. Keene, 1995, Multichannel seismic-reflection profiling of the R/V Maurice Ewing during the Los Angeles Region Seismic Experiment (LARSE), California , USGS Open File Report 95-228.

Chen, L., L. Wen, and T. Zheng, 2005a, A wave equation migration method for receiver function imaging: 1. Theory, Journal of Geophysical Research, **110,** B11309.

Chen, L., L. Wen, and T. Zheng, 2005b, A wave equation migration method for receiver function imaging: 2. Application to the Japan subduction zone, Journal of Geophysical Research, **110,** B11310.

Cohen, J. K. and Stockwell, Jr. J. W., 2005, CWP/SU: Seismic Un*x Release No. 38: a free package for seismic research and processing, Center for Wave Phenomena, Colorado School of Mines.

Dessa, J.X., S. Operto, S. Kodaira, A. Nakanishi, G. Pascal, K. Uhira, and Y. Kaneda, 2004, Deep seismic imaging of the eastern Nankai trough, Japan, from multifold ocean bottom seismometer data by combined travel time tomography and prestack depth migration, Journal of Geophysical Research, **109**, B02111.

Fletcher, R., 1980, Practical methods of optimization, John Wiley & sons.

Fuis, G. S., D.A. Okaya *et al*., 1996, Images of crust beneath southern California will aid study of earthquakes and their effects, EOS Transactions, **77**, 173,176.

Fuis, G. S., R. W. Clayton, *et al*., 2003, Fault systems of the 1971 San Fernando and 1994 Northridge earthquakes, southern California: Relocated aftershocks and seismic images from LARSE II, Geology **31,** 171-174.

Fuis, G. S., T. Ryberg, *et al*. 2001a, Seismic mapping of shallow fault zones in the San Gabriel Mountains from the Los Angeles Region Seismic Experiment, southern California, Journal of Geophysical Research, **106**, 6549-6568.

Fuis, G.S., T. Ryberg, *et al*. 2001b, Crustal structure and tectonics from the Los Angeles basin to the Mojave Desert, southern California, Geology **29,** 15-18.

Fuis, G. S., J. M. Murphy., *et al*., 2001c, Report for borehole explosion data acquired in the 1999 Los Angeles Region Seismic Experiment (LARSE II), southern California: Part I, description of the survey, USGS Open-File Report 01–408

Godfrey, N.J., G. S. Fuis, *et al*., 2002, Lower crustal deformation beneath the central Transverse Ranges, southern California, results from the Los Angeles Region Seismic Experiment, Journal of Geophysical Research, **107**, ETG 8-1.

Gray, S.H., J. Etgen, J. Dellinger, and D. Whitmore, 2001, Seismic migration problems and solutions, Geophysics, **66**, 1622-1640.

Hauksson, E., 2000, Crustal structure and seismicity distribution adjacent to the Pacific and North America plate boundary in southern California, Journal of Geophysical Research, **105**, 875-13

Hauksson, E., and J. S. Haase, 1997, Three-dimensional VP and VP /VS velocity models of the Los Angeles Basin and central Transverse Ranges, California, Journal of Geophysical Research, **102**, 5423–5453.

Henning, A.T., D.S. Sawyer and D.C. Templeton, 2004, Exhumed upper mantle within the ocean-continent transition on the northern West Iberia margin: Evidence from prestack depth migration and total tectonic subsidence analyses, Journal of Geophysical Research, **109**, 105.

Henyey, T.L., G.S. Fuis, *et al*., 1999, The "LARSE" Project – Working toward a safer future for Los Angeles, USGS Fact Sheet 110-99.

Hopper, J.R., T.D. Jensen, W. S. Holbrook, H. C. Larsen, D. Lizarralde, J. Korenaga, G. M. Kent, and P. B. Kelemen, 2003, Structure of the SE Greenland margin from seismic reflection and refraction data: Implications for nascent spreading center subsidence and asymmetric crustal accretion during North Atlantic opening, Journal of Geophysical Research, **108**, 2269.

Kopp, H., D. Klaeschen, E.R. Flueh, and J. Bialas, 2002, Crustal structure of the Java margin from seismic wide-angle and multichannel reflection data, Journal of Geophysical Research, **107**, 2034.

Kohler, M., H. Magistrale, and R. Clayton, 2003, Mantle heterogeneities and the SCEC three-dimensional seismic velocity model version 3, Bulletin Seismological Society of America, **93**, 757-774.

Kohler, M. D., P.M. Davis, *et al*., 1996, Data report for the 1993 Los Angeles Region Seismic Experiment (LARSE93), southern California: A passive study from Seal Beach northeastward through the Mojave Desert, USGS Open File Report 96-85.

Louie, J.N, and J.E. Vidale, 1991, Array analysis of reflector heterogeneity, Geophysics, **56**, 565-571,

Lutter, W. J. et. al., 1999, Tomographic images of the upper crust from the Los Angeles basin to the Mojave Desert, California: Results from the Los Angeles Region Seismic Experiment, Journal of Geophysical Research, **104**, 25543-25565.

Moser, T. J., 1991, Shortest path calculation of seismic rays: Geophysics, **56**, 59–67.

Murphy, J. M., G. S. Fuis, *et al*., 1996, Report for explosion data acquired in 19994 Los Angeles Region Seismic Experiment (LARSE 94), Los Angeles, California, US Geological Survey Open-File Report 96-536.

Paige, C. C. and M. A. Saunders, 1982, LSQR: An algorithm for sparse linear equations and sparse least squares, ACM Trans. Math. Soft., **8**, 43-71.

Ryberg, T. and G. Fuis, 1998, The San Gabriel Mountains bright reflective zone: possible evidence of young mid-crustal thrust faulting in southern California: Tectonophysics, **286**, 31-46.

Warner, M., 1987, Migration - Why doesn't it work for deep continental data?, Geophysical Journal of the Royal Astronomical Society, **89**, 21-26.

Zhou, H., 2003, Multi-scale traveltime tomography, Geophysics, **68**, 1639-1649.

Zhou, H., 2004, Multi-scale tomography for crustal P and S velocities in southern California, PAGEOPH, 161, 283-302, doi: 10.1007/s00024-003-2444-7

Zhu, L., 2000, Crustal structure across the San Andreas Fault, southern California from teleseismic converted waves, Earth and Planetary Science Letters, **179,** 183–190.

Zhu, L., 2002, Deformation in the lower crust and downward extent of the San Andreas Fault as revealed by teleseismic waveforms, Earth Planets Space, **54**, 1005–1010.

Zhu, L. and H. Kanamori, 2000, Moho depth variation in southern California from teleseismic receiver functions: Journal of Geophysical Research, **105**, 2969-2980.